ABSTRACT

Title of Dissertation: LIMITS ON NEUTRINO EMISSION
FROM GAMMA-RAY BURSTS WITH THE
40 STRING ICECUBE DETECTOR

Kevin J. Meagher, Doctor of Philosophy, 2012

Dissertation directed by: Professor Kara Hoffman
Department of Physics

Cosmic rays have been observed on Earth with energies in excess of 10^{20} eV. Because cosmic rays are charged particles and are bent by galactic magnetic fields, the origin of these particles has remained a mystery. Gamma-ray bursts are one of a few astronomical sources containing an environment capable of accelerating charged particles to the energies observed. In addition, gamma-ray bursts are the leading candidate due to the fact that the total aggregate power observed in gamma-ray bursts and ultra high energy cosmic rays are the same order of magnitude. Neutrinos can only be created by hadronic interactions, so an observation of neutrinos in coincidence with a gamma-ray burst would provide compelling evidence that hadrons are accelerated in gamma-ray burst fireballs and hence the origin of cosmic rays. Using the IceCube Neutrino Observatory in its 40 string configuration, a stacked search was performed to look for the simultaneous occurrence of muon neutrinos with 117 gamma-ray bursts. This analysis is optimized on the assumption that order TeV neutrinos are produced in $p\gamma$ interactions during the prompt phase of the GRB, when gamma-rays coexist with protons that are assumed to be the source of the observed extragalactic cosmic ray flux. With half the detector complete, this is the first analysis sensitive to the flux predicted by fireball phenomenology and the assumption that GRBs are the sources of the highest energy cosmic rays. No evidence for neutrino emission was found, placing a 90% CL upper fluence of 1.1×10^{-3} erg cm^{-2} in the energy range of 37 TeV - 2.4 PeV or 82% of the predicted fluence.

LIMITS ON NEUTRINO EMISSION FROM GAMMA-RAY BURSTS WITH THE 40 STRING ICECUBE DETECTOR

by

Kevin James Meagher

Dissertation submitted to the Faculty of the Graduate School of the
University of Maryland, College Park in partial fulfillment
of the requirements for the degree of
Doctor of Philosophy
2012

Advisory Committee:
Professor Kara Hoffman, Chair/Advisor
Professor Zackaria Chacko
Professor Julie McEnery
Professor Coleman Miller
Professor Gregory Sullivan

Acknowledgments

IceCube is a large collaboration and there is no way I could possible thank everyone who contributed to the design and construction of this great detector, so I won't even try. The following is a list of people who I would like to thank, this list is incomplete. Kara Hoffman for serving as my advisor. Erik Blaufuss for enumerable help and advice. Greg Sullivan whose great seminar talk got me interested in IceCube and other useful advice. Ignacio Taboda for his help and guidance as GRB working group leader. Alexander Kappas for help on understanding fireball neutrino phenomenology. John Pretz, Alex Olivas, and Dusan Turcan for teaching me how to analyze IceCube data. Phil Roth for countless discussions on how to actually implement this analysis. Troy Straszheim for introducing me to HDF5 files which saved me more time than I can possibly imagine among many other useful ideas. Frances Halzen for repeatedly reminding me that the purpose of this analysis was to make a discovery. Henrike Wissing for general encouragement. Brian Christy and Peter Redl for many discussions both pertaining to this analysis and on unrelated topics. Kevin Hurley for useful discussions on IPN. Nathan Whitehorn for his work on the paper. Christian Gils and Don La Dieu for excellent computer support. Robert Hellauer and Natalie Henley for useful comments on this thesis. Helina Tuminaro, Rozi Sahand, and Naomi Russo for all their help. Brandon Anderson, Pat Harding, Bill Young, Jennifer Elle, Remmington Reid, Mary Fellman for being great roommates and great friends.

Table of Contents

List of Tables

List of Figures

List of Abbreviations

ACS	Anti Coincidence Shield
AGILE	Astro-rivelatore Gamma a Immagini LEggero
AGN	Active Galactic Nuclei
AMANDA	Antarctic Muon And Neutrino Detector Array
ANIS	All Neutrino Interaction Simulation
ATWD	Analog Transient Waveform Digitizer
BAT	Burst Alert Telescope
BATSE	*Burst and Transient Source Experiment*
BGO	Bismuth Germanate Oxide
BH	Black Hole
CC	Charged Current
CCD	Charge-Coupled Device
CGRO	*Compton Gamma-Ray Observatory*
CoG	Center of Gravity
CORSIKA	COsmic Ray SImulations for KAscade
CPU	Central Processing Unit
CsI(Tl)	Thallium doped Cesium Iodide
CTEQ	Coordinated Theoretical-Experimental project on QCD
DOM	Digital Optical Module
DAQ	Data AQuisition
Dec	Declination
EGRET	*Energetic Gamma-Ray Experiment Telescope*
EeV	ExaElectron Volt (10^{18} eV)
eV	Electron Volt
fADC	Fast Analog to Digital Converter
FRED	Fast Rise, Exponential Decay
FPGA	Field Programmable Gate Array
GBM	Gamma-Ray Burst Monitor
GCN	GRB Coordinate Network
GeV	GigaElectronVolt
GGS	Global Geospace Science
GRB	Gamma-Ray Burst
GZK	Greisen, Zatsepin, and Kuz'min
IBIS	Imager on-Board the INTEGRAL Satellite
IERS	International Earth Rotation and Reference Systems Service
INTEGRAL	INTErnational Gamma-Ray Astrophysics Laboratory
IPN3	Third InterPlanatary Network
ISM	InterStellar Medium
KeV	KiloElectronVolt
LAT	Large Area Telescope
ΛCDM	Lambda-Cold Dark Matter
LED	Light Emitting Diode
LSB	Long-Soft Burst
MDP	Model Discovery Potential

MESSENGER	MErcury Surface, Space ENvironment, GEochemistry, and Ranging
MeV	MegaElectronVolt
MHz	MegaHertz
mHz	MilliHertz
MMC	Muon Monte Carlo
Mpc	Mega Parsec
MPE	Multi PhotoElectorn
NaI(Tl)	Thallium doped Sodium Iodide
NASA	National Aeronautics and Space Administration
NC	Neutral Current
NS	Neutron Star
ns	NanoSecond
PDF	Probability Distribution Function
PeV	PetaElectronVolt (10^{15} eV)
PMT	Photomultiplier Tube
RPQM	Recombination Quark Parton Model
PnF	Processing and Filtering
QE	Quantum Efficiency
RA	Right Ascension
RAPCal	Reciprocal Active Pulsing Calibration
SHB	Short-Hard Burst
SN	SuperNova
SPE	Single PhotoElectron
SPI	SPectrometer for INTEGRAL
TDRSS	Tracking and Data Relay Satellite System
TeV	TeraElectronVolt (10^{12} eV)
UHECR	Ultra High Energy Cosmic Ray
UT	Universal Time
UTC	Coordinated Universal Time
UVOT	Ultraviolet/Optical Telescope
WAM	Wide-band All-sky Monitor
XRT	X-Ray Telescope
XRF	X-Ray Flash
XRR	X-Ray Rich burst
ZeV	ZettaElectron Volt (10^{21} eV)

Chapter 1

Introduction

Cosmic rays are charged particles which hit the Earth's atmosphere and cause large showers of secondary particles. The energy spectrum of cosmic ray primaries approximately follows a power-law over 11 orders of magnitude, see Figure 1.1. The cosmic ray spectrum follows $\mathrm{d}N/\mathrm{d}E \propto E^{-2.7}$ from below 10^{10} eV, where they are modulated by the solar wind, up to a feature called the knee at about 10^{15} eV. At these energies, cosmic rays are bent by galactic magnetic fields so they do not point back to their origin. Cosmic rays up to this energy are believed result from Fermi acceleration in supernova remnants in the galaxy. Electrons up to 10^{14} eV have been observed in supernova remnant SN1006[1]. Since Fermi shock acceleration works regardless of particle charge and mass and since electrons have more substantial loss mechanisms than protons this implies that protons are also accelerated to at least the same energy. Fermi acceleration produces a spectrum with an exponent of -2 to -2.2 which is softened to -2.7 as the cosmic rays propagate though the interstellar medium[2]. At energies beyond the knee, the spectrum softens to $E^{-3.0}$. The reasons for this are unclear: one possibility is that it could be due to galactic accelerators reaching their maximum energy or propagation within the galaxy[3, 4].

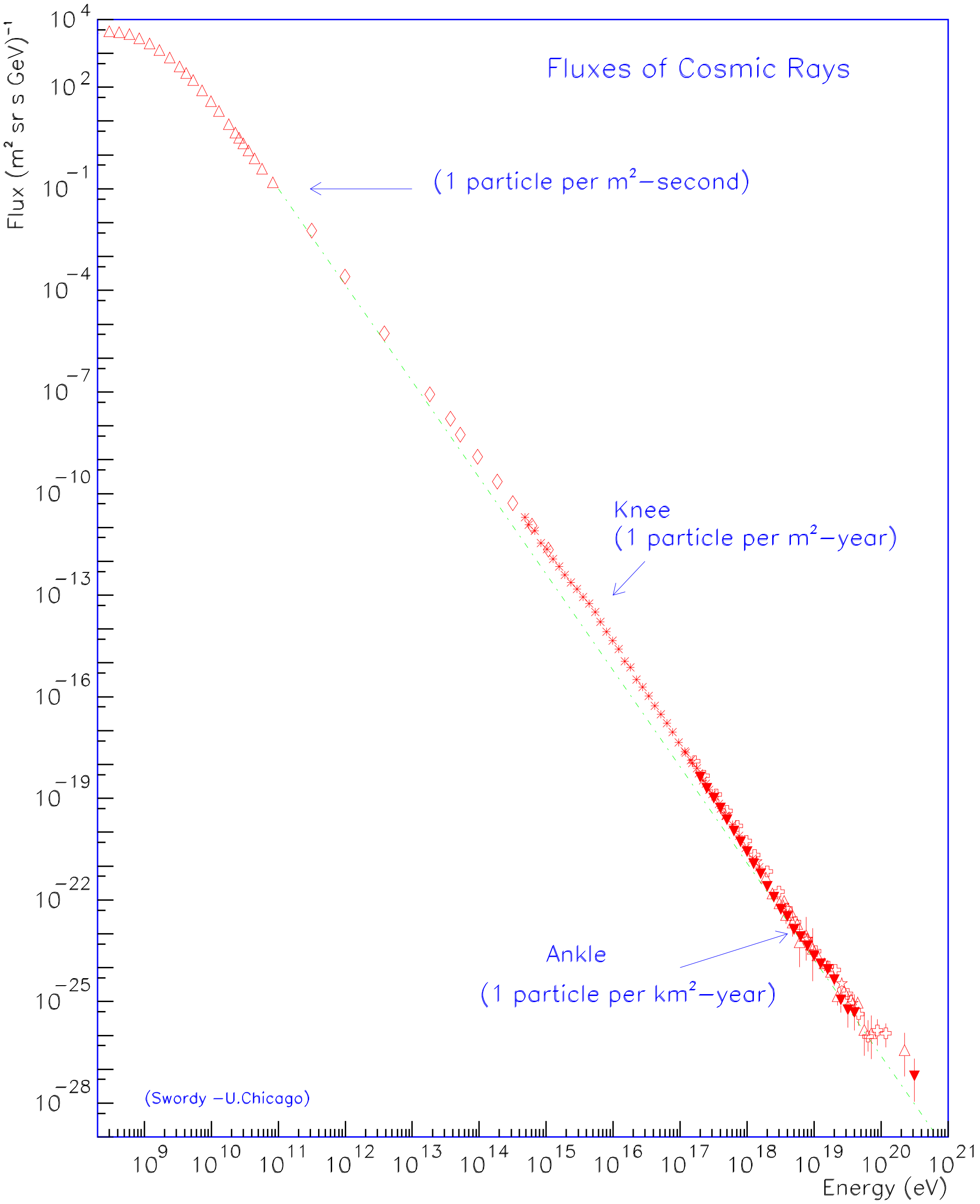

Figure 1.1: Cosmic rays maintain an approximate power-law over 11 orders of magnitude in energy. The red points are measurements and the green line indicates a slope of $E^{-2.7}$. Figure taken from [5].

At $10^{18.6}$ eV there is another feature called the ankle where the spectrum hardens to $E^{-2.6}$, cosmic rays with energies beyond the ankle are called Ultra High Energy Cosmic Rays(UHECR) and are believed to be accelerated by extragalactic sources. Above $10^{19.5}$ eV cosmic rays experience a sharp drop off[6,7], see figure 1.2. This is known as the GZK cutoff[8,9], the energy where protons propagating through intergalactic space become attenuated by Δ-resonance interactions with the cosmic microwave background. UHECR are believed to be of extragalactic origin because their Larmor radius due to interstellar magnetic fields is larger than the size of the galaxy, such that UHECR must point back to their origin. Since their distribution in the sky is near isotropic they cannot be of galactic origin[10, 11].

In order to accelerate particles to these energies, the only plausible mechanism is Fermi acceleration[12–15]. Fermi acceleration requires both a shock wave to accelerate particles and a magnetic field to confine the particles to the acceleration region. According to Fermi, a particle which crosses a shock and is then scattered back across the same shock will on average have gained energy. With each successive cycle of scattering and crossing the shock, the particle will continue to gain energy. If the shock front propagates for an arbitrarily long distance, then particles on its boundary can be accelerated to arbitrarily large energies, provided there is a sufficiently large magnetic field to confine them to the shock region. A plot showing astrophysical objects which contain sufficient magnetic field and shock front length are shown in figure 1.3. The two astrophysical candidate sources which have conditions capable of accelerating protons to 10^{20} eV are Gamma-Ray Bursts (GRBs)[18–20] and Active Galactic Nuclei (AGN)[21]. It has been calculated that

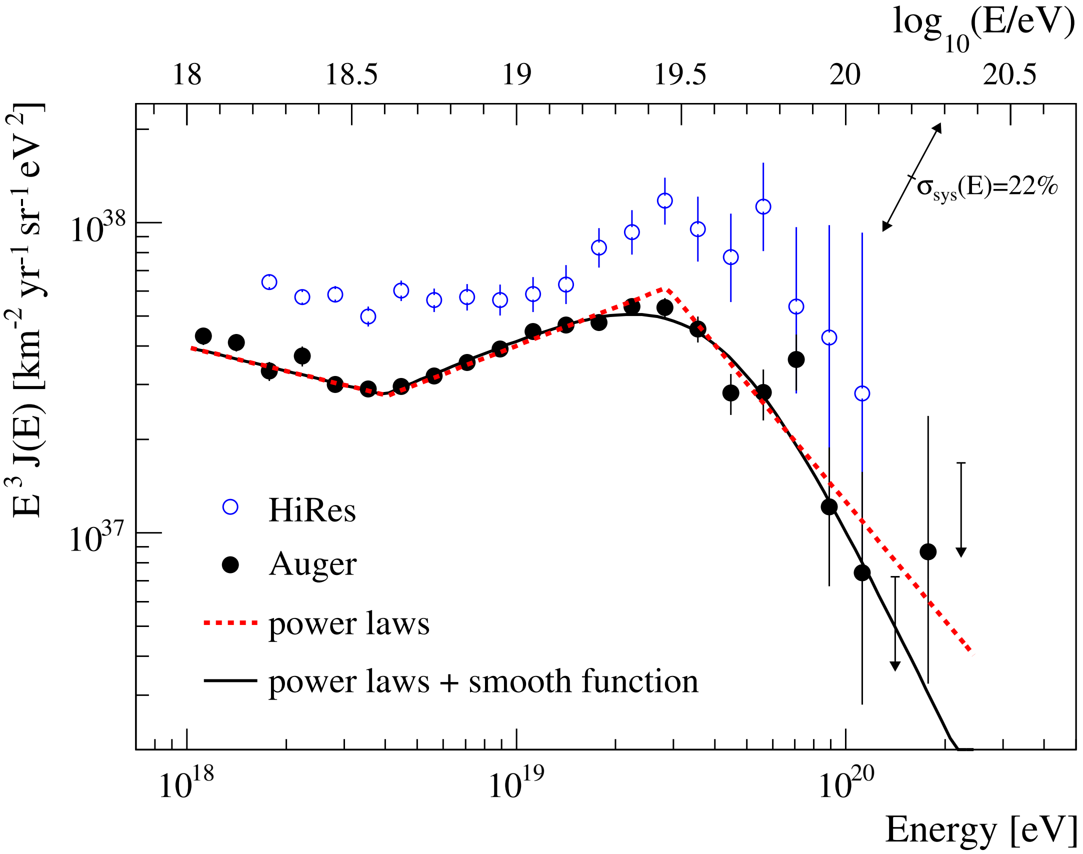

Figure 1.2: Spectrum of the highest energy cosmic rays. Above $10^{18.6}$ eV the cosmic ray spectrum hardens to a slope of $E^{-2.6}$, which is believed to be evidence of a different source of acceleration from the source which dominates below $10^{18.6}$eV. Above $10^{19.5}$ eV the spectrum is cutoff by the GZK cutoff, which is further evidence of an extragalactic origin. Figure taken from [6].

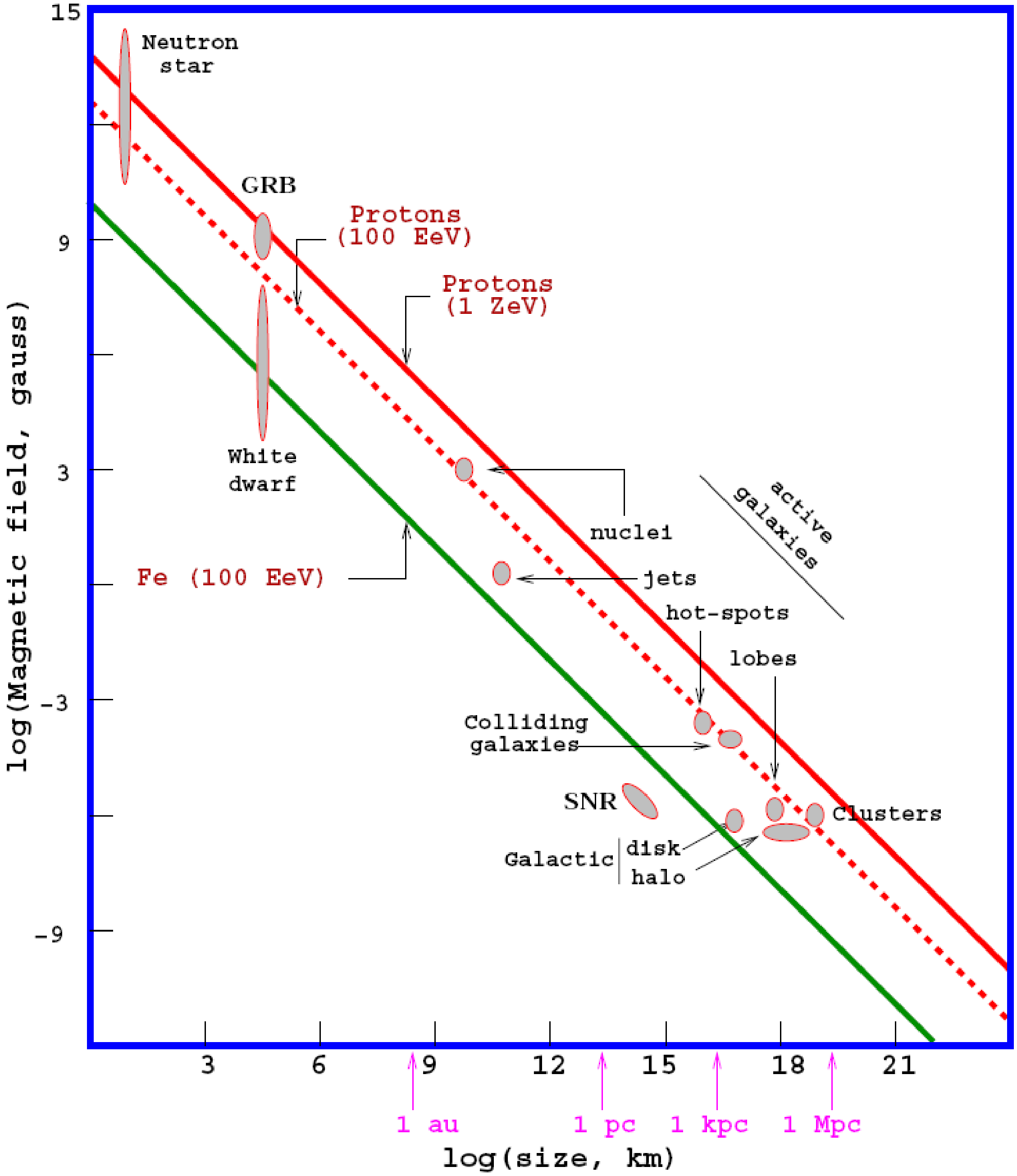

Figure 1.3: The Hillas Plot (figure from [16] a modified version from [17]) shows possible sites of astrophysical acceleration. Candidate sites must possess sufficient magnetic field to confine the particles during acceleration or sufficient size to accelerate. The solid red line represents objects which can accelerate protons to 1 ZeV = 10^{21} eV, the dotted red line represents protons accelerated to 100 EeV = 10^{20} eV, and the green line represents iron accelerated to 100 EeV.

the total power available for GRBs to create UHECR is similar to the observed power[22–24], suggesting GRBs as a plausible source.

If protons are accelerated alongside electrons in GRBs, which would therefore be the source of UHECRs, then those protons should interact with the observed gamma-rays and, through the Δ-resonance, create neutrinos[25] (Δ-resonance is described in detail in section 2.6.) To reverse this logic, if neutrinos are observed to originate from GRBs, then GRBs must be the site of hadronic interaction and thus a source of UHECR. It is also important to note that without Δ-resonances protons cannot escape the acceleration region and become UHECR[26, 27]. For this reason, searching for neutrinos associated with GRBs has been an active subject of study with neutrino telescopes.

The analysis presented in this thesis is built on previous work. Several stacked analyses correlating muon neutrinos with GRBs have been performed with IceCube[28] and its predecessor AMANDA[29–34]. There have also been analyses which search based on a single very bright GRB[35, 36], as well as search for neutrinos with energies high enough to be seen over the background of downward cosmic ray muons in IceCube[37, 38]. A model-independent search was performed which looked for neutrinos with a time offset of up to an hour from the GRB[39]. Although neutrino cascades do not provide directional information, they are sensitive to interaction of neutrinos of all flavors, thus searches correlating them with GRBs have been performed[40, 41]. Follow-ups of IceCube events have been performed to look for GRB afterglows in the optical[42, 43] and x-ray[44] bands. Searches have also been performed with lower energy neutrino telescopes using Super-K[45–47], Baikal Deep Underwater Neutrino Telescope[48] and ANTARES[49]. At energies above IceCube's range, neutrino interactions can be observed by radio emission; searches for neutrinos from GRBs have been performed using the RICE detector buried in the Antarctic glacier[50] and with ANITA, a balloon borne experiment above the ice[51].

This thesis is organized as follows:

- Chapter 2 contains a brief introduction to gamma-ray bursts, a description of the fireball model of gamma-ray emission, and a prediction for neutrino emission within this model.
- Chapter 3 gives an overview of the experimental side of GRB detection and a description of the gamma-ray observatories which provided triggers for this analysis.
- Chapter 4 gives an overview of the IceCube Neutrino Observatory. It contains a description of the hardware, the reconstruction techniques used, and an overview of the simulation used to understand the detector.
- Chapter 5 describes the criteria used to select GRB triggers and the data quality checks to ensure proper detector operation.
- Chapter 6 describes the criteria with which IceCube events were selected as neutrino candidates.

- Chapter 7 describes the unbinned maximum likelihood analysis which was used to correlate neutrino candidate occurrences with GRBs and the statistics used.
- Chapter 8 contains the results of the analysis and systematic errors as well as a discussion of the implications for Ultra High Energy Cosmic Rays.

Chapter 2

Gamma-Ray Bursts

Gamma-ray bursts are one of the brightest and most interesting phenomena in the Universe. GRBs are observed in all bands of the electromagnetic spectrum from high energy gamma-rays to radio. GRBs have been hypothesized to be the source of UHECR.

GRBs occur randomly in the sky without warning. Their locations in the sky are completely isotropic. GRBs are bright flashes of non-thermal gamma radiation. Typical GRBs outshine the rest of the gamma-ray sky during their prompt phase. Their energy spectrum is non-thermal, and can almost always be characterized by a Band function[52], shown in figure 2.1, which consists of two smoothly joined power-laws. Sometimes a thermal component is observed with a smaller intensity than the non-thermal component. Satellites that do not have sufficient spectral response will only see a portion of the energy spectrum and observe a single power-law or a power-law with an exponential cutoff. As shown in figure 2.2, the duration of GRBs has a bimodal distribution with one peak at 30 seconds and another at 0.3 seconds[54]. Most bursts have durations between 0.1 seconds and 1000 seconds. However the temporal light curves of GRBs are incredibly diverse[55], see figure 2.3. Most bursts can be described as the superposition of one or many sharp peaks with a FRED profile. FRED stands for fast rise exponential decay, where the timescale of the rise

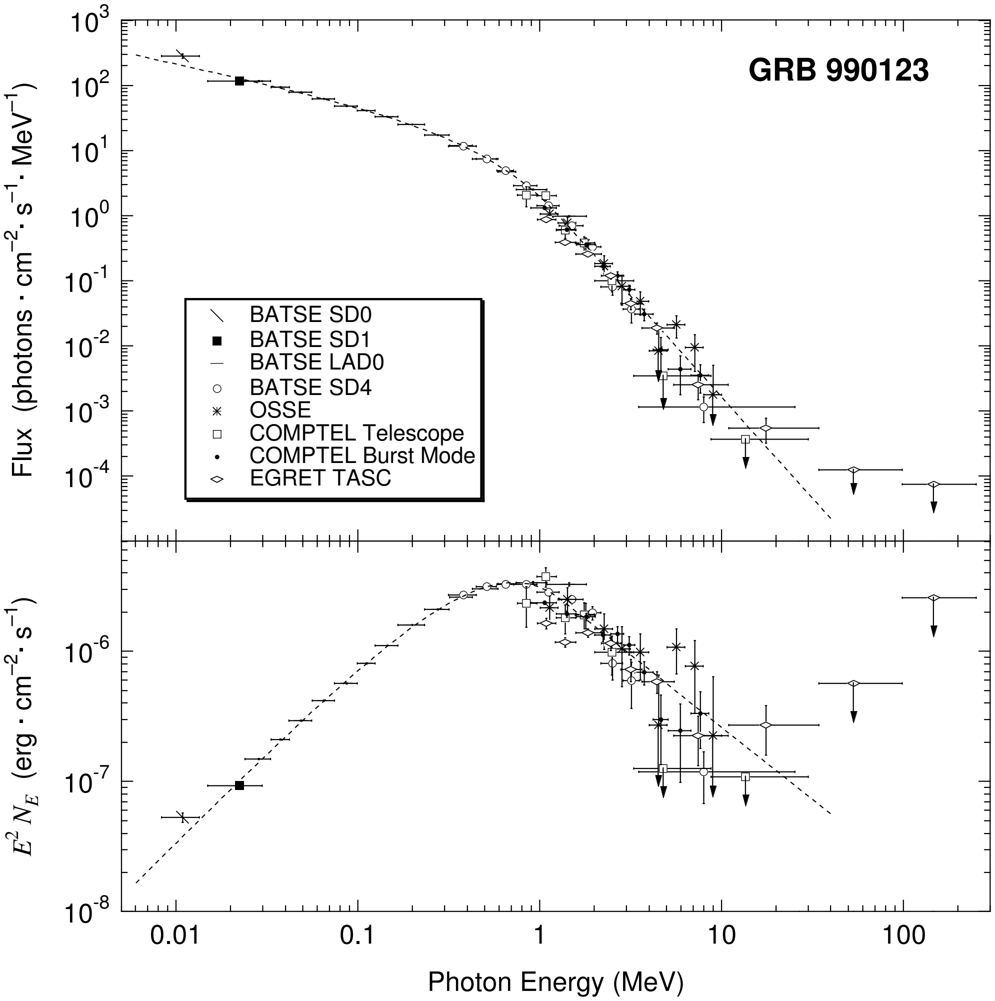

Figure 2.1: Deconvolved Spectra of GRB990123 from the *Compton Gamma-ray Observatory*. The photon flux is plotted on top and the energy flux on bottom. The data is well fit by a Band function[52]. Figure from [53].

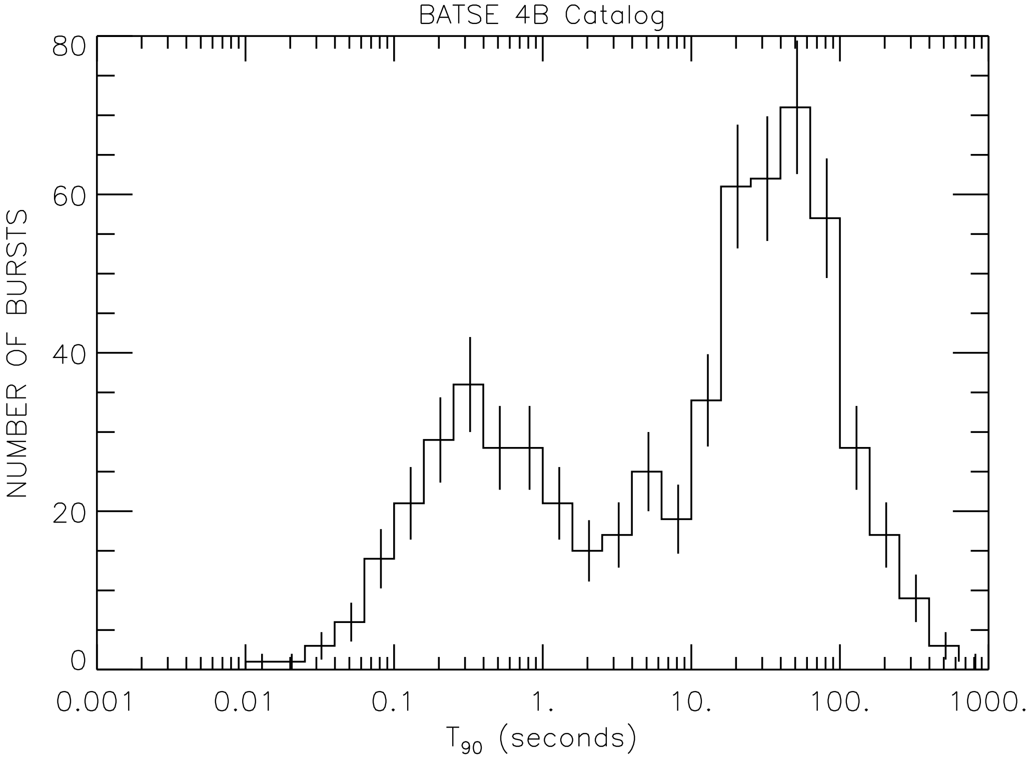

Figure 2.2: The duration (T_{90}) of GRBs from the 4th BATSE catalog[54]. A clear bimodal distribution is seen with short busts peaking at 0.3 seconds and long bursts peaking at 30 seconds.

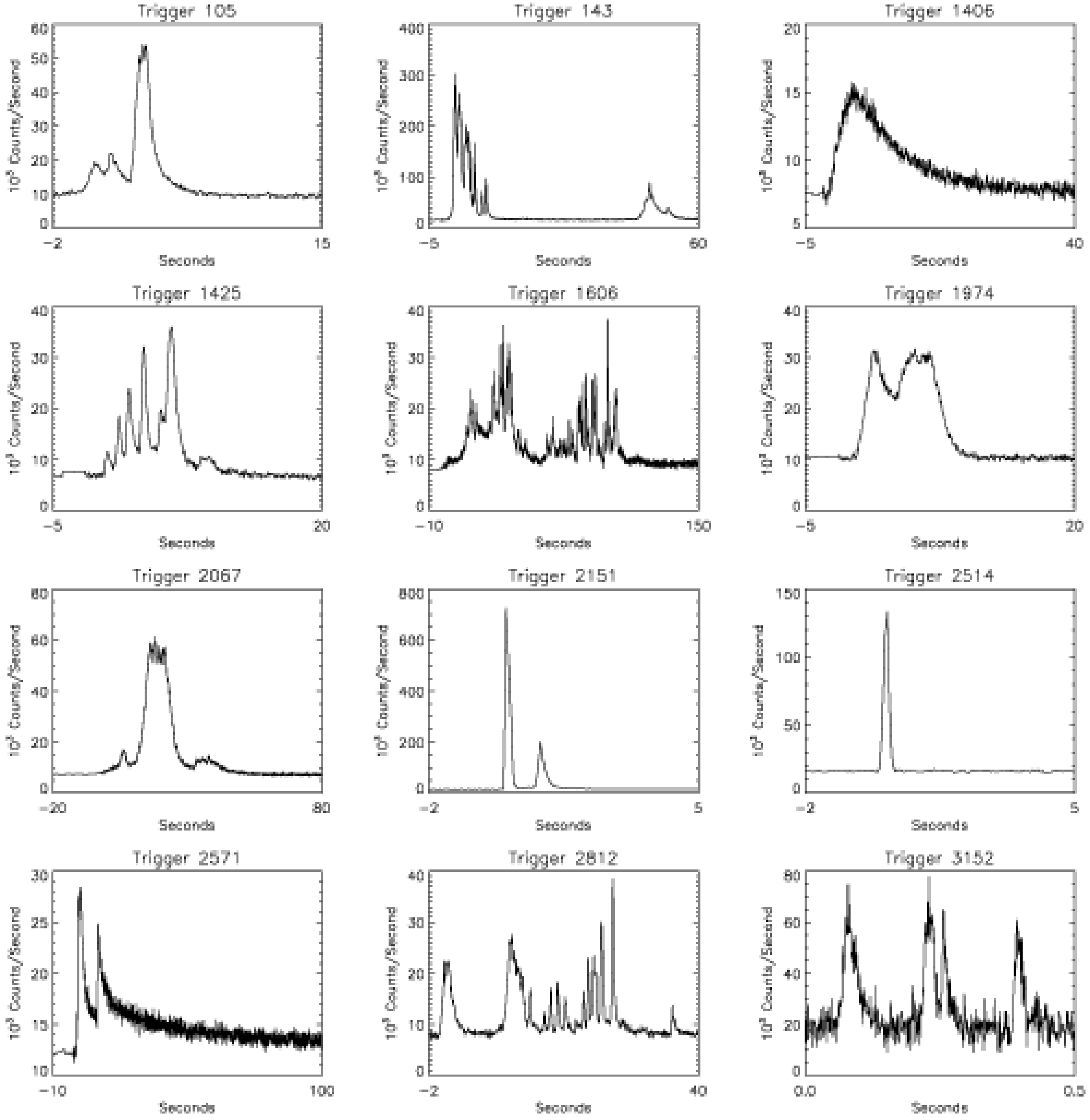

Figure 2.3: The observed light curves of 12 BATSE bursts. Both short and long bursts are shown. GRBs show great diversity in their light curves both in duration and shape. Bursts can exhibit some or all of the following behavior: a single peak with a fast rise exponential decay, multi-peaked, erratic behavior, and long periods of quiescence between events. Figure taken from [56] see also [55].

is much shorter than the timescale of the decay. However, the time between spikes and the relative height of the peaks are extremely diverse and vary from burst to burst.

Following the prompt gamma-ray phase of GRBs there is a prolonged afterglow. Afterglows have been observed in all bands from x-ray to radio. The afterglows are generally observed to have a power-law energy spectrum and also to fade as a power-law function of time. The power-law decay of 30 afterglows is shown in figure 2.4. In the pre-*Swift* era most X-ray afterglow were observed to decay with a power-law with exponent ~ 1.2. With *Swift*'s rapid followup capability more features were observed. Many bursts have a steep decay which is consistent with the low energy tail of the prompt gamma-ray emission. This is sometimes followed by a phase where the decay is shallower than the normal phase with an exponent of ~ 0.5, this is thought to be continuous injection of the fireball energy into the ISM. There are also X-ray flares caused by continued activity of the central engine. This generalized theory of afterglows is shown in figure 2.5.

2.1 History

GRBs were first discovered in 1967 by the Vela satellite program which was looking for violation of the Nuclear Test Ban Treaty[59]. Several bursts of gamma-rays were observed which did not look like nuclear events. Identical observations were recorded by satellites on opposite sides of the Earth, providing convincing evidence that the bursts were not coming from Earth. Since the Vela satellite

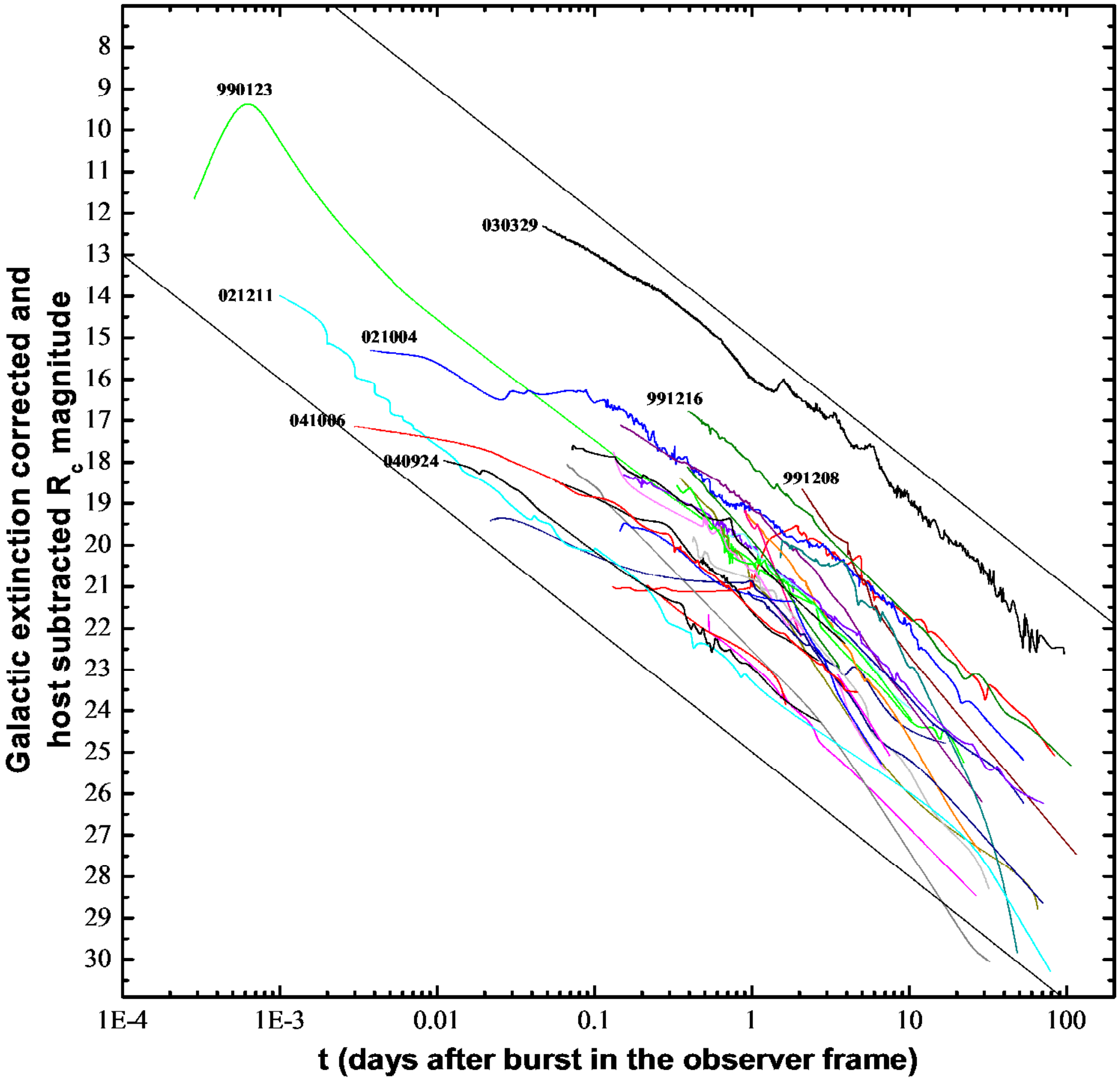

Figure 2.4: Observed near infrared afterglow of 30 pre-*Swift* bursts. The light curves have been corrected for galactic extinction and host galaxy contribution. In the case of GRB030329 the contribution from the associated supernova has been removed. The two lines are meant to guide the eye, they correspond to a decay slope of $\alpha = 0.5$. Note the bump in the light curve of 990123 at early times which is used to measure the bulk Lorentz factor (see section 2.4.) Figure from [57].

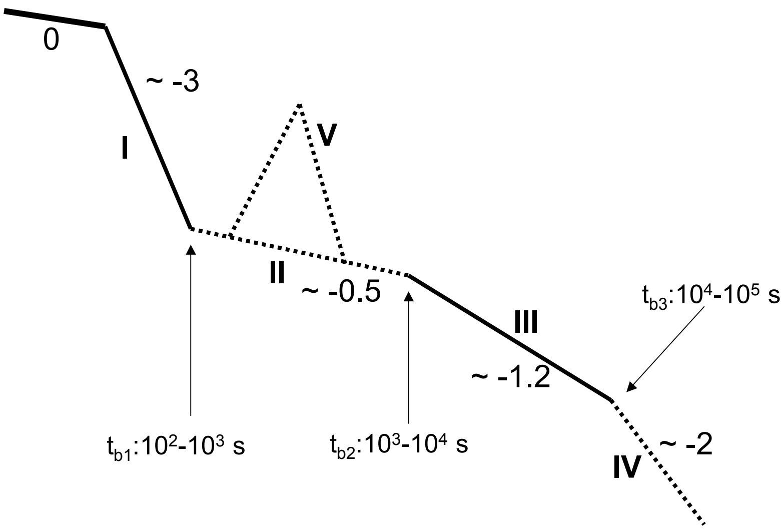

Figure 2.5: Simplified diagram of a generalized GRB afterglow. The horizontal axis indicates time and the vertical axis indicates luminosity. Regions in solid lines are seen in most bursts while dotted lines are seen occasionally. Region 0 represents the x-ray tail of the prompt GRB emission. Region I is the steep decay phase where the x-ray tail of the prompt emission decays rapidly after activity ceases. Region II is the shallow decay phase thought to be caused by continuous injection of energy into system. Region III is the classical decay caused by the forward shock interacting with the interstellar medium. Region IV is the steep decay phase caused by jet breaks after the shock front has decelerated sufficiently for the observer to observe the afterglow as a narrow jet (see section 2.5.) Region V shows x-ray flares which are sometimes observed and thought to be caused by continued injection of energy from the central engine. Figure taken from [58].

program was classified, the existence of GRBs remained classified for seven years after their initial discovery. Using timing triangulation and Earth occultation the Earth, sun, moon and population of visible supernova were all quickly ruled out[60]. These observations were backed up by other gamma-ray detectors on board satellites at the time[61] which were able to observe the non-thermal structure[62].

There was great debate about the nature of GRBs, with theories ranging from extragalactic events to comet collisions in the Oort cloud. Very little was learned until the 1990 launch of the *Compton Gamma-Ray Observatory* (CGRO). The *Burst and Transient Source Experiment* (BATSE) on board CGRO consisted of eight NaI(Tl) detectors on the corners of the CGRO and were sensitive to energies in the range 15 keV - 20 MeV[56]. BATSE used timing triangulation to localize GRBs within an error radius on order few degrees. It showed that GRBs were located nearly isotropically in the sky eliminating all potential galactic candidates as the source of GRBs[63], see figure 2.6. BATSE also found that the durations of GRBs have a bimodal distribution, long GRBs with $T > 2$ sec and short with $T < 2$ sec[64].

Almost all GRBs detected by BATSE had an energy spectrum that could be well-defined by a Band function, which is two power-laws smoothly connected[52], however there were several observations of high energy emission inconsistent with the Band function. *The Energetic Gamma-Ray Experiment Telescope* (EGRET)[65] also on board CGRO imaged seven bursts with energy exceeding 30 MeV[66]. This includes an 18 GeV photon detected 90 minutes after the burst in GRB940217[67] and a rising late GeV spectral component in GRB941017[68]. The Milagrito, the

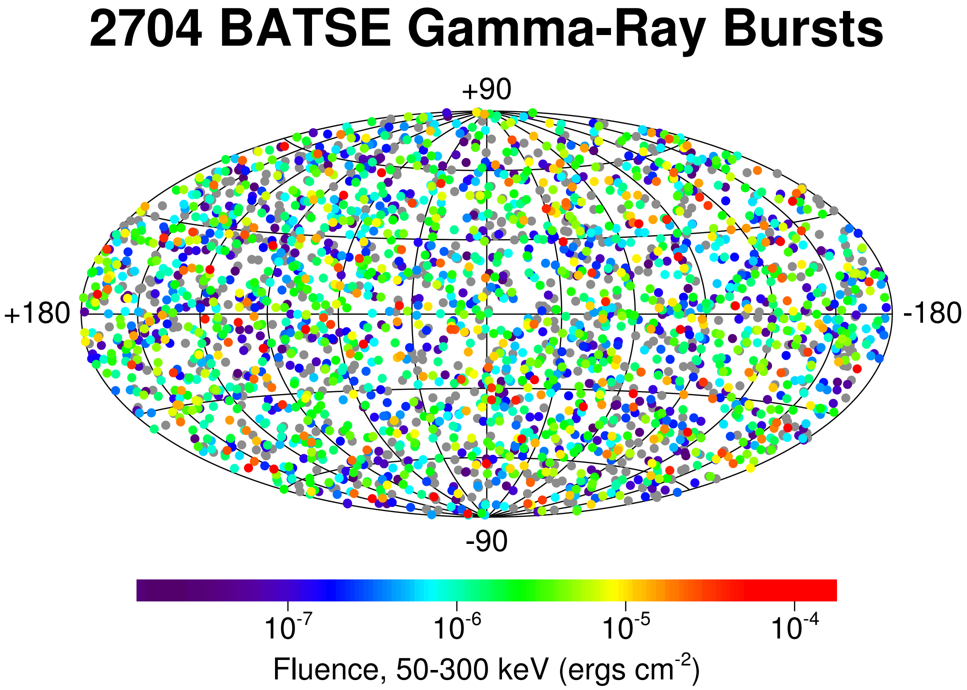

Figure 2.6: This map shows the locations of a total of 2704 Gamma-Ray Bursts recorded with the Burst and Transient Source Experiment on board NASA's Compton Gamma-Ray Observatory during the nine-year mission. The projection is in galactic coordinates; the plane of the Milky Way Galaxy is along the horizontal line at the middle of the figure. The burst locations are color-coded based on fluence, which is the energy flux of the burst integrated over the total duration of the event. Bright bursts appear in red, and dim bursts appear in purple, grey indicates bursts for which the fluence cannot be calculated due to incomplete data. Figure taken from [54, 56].

prototype for Milagro[69], observed the an excess of photons with energy greater than 650 GeV from GRB970417A with a statistical significance at the 3σ level[70,71]. However, subsequent searches with Milagro for high-energy gamma-ray emission from GRBs did not find similar signals[72–74], indicating such events are rare.

The next satellite to make a significant GRB discovery was *Beppo*-SAX[75], a hard x-ray telescope which was the first instrument able to localize GRBs to arcminutes quickly which allowed follow up in the optical and radio band. GRB970228 was the first GRB localized by *Beppo*-SAX [76]. Within a year of launch *Beppo*-SAX localized GRB970508[77] and GRB971214[78] which allowed redshift measurements, giving proof of a cosmological origin of GRBs. The afterglow of GRB971214 was the first observation to reveal the true energy scale of GRBs: 10^{51} ergs, as well as the beamed nature of the emission[79].

More recently the *Swift* and *Fermi* missions have significantly increased our knowledge of GRBs. *Swift* has detected a large sample of GRBs with associated afterglows; several of these afterglows have revealed extremely high redshifts: GRB050904 with $z \approx 6.3$[80], GRB080913 with $z \approx 6.7$[81] and GRB090423 $z \approx 8.2$[82,83]. Redshifts this high indicate that these bursts were created at the time of the earliest stars. *Swift* has also observed the first afterglows from short GRBs[84]. While *Fermi* has increased our knowledge of the highest energy gamma-rays in GRBs, it has also detected several GRBs with a high energy power-law component in addition to the typically observed band function[85–88]. For a more detailed description of *Swift* and *Fermi* see chapter 3.

2.2 Fireball Model

This section gives a brief description of the Fireball theory of GRBs, for a more complete review see[89–94]. In the Fireball model there are two distinct engines which convert energy: 1) the progenitor or central engine which converts gravitational energy into kinetic energy and 2) internal shocks which convert kinetic energy to gamma-rays.

In the central engine, a cataclysmic event results in the rapid accretion of matter onto a black hole. Two types of central engines fulfill this criteria: the core collapse of a massive star (collapsar)[95, 96] or the merger of two compact objects, either a neutron star–neutron star merger or a neutron star–black hole merger[97]. Accretion induced collapse of a magnetized white dwarf has also been suggested as a possible central engine[98]. Both kinds of central engines lead to an accretion disk around a black hole which creates jets of plasma along the spin axis. These jets contain a plasma of leptons, photons and baryons are optically thick. The energy injected into this plasma causes the plasma to expand adiabatically, accelerating the plasma until it reaches a Lorentz factor Γ[99] see figure 2.7. Once this Lorentz factor is reached the fireball continues to coast at a constant Lorentz factor[100, 101]. At the photosphere radius $r_{ph} \simeq 10^{11}$ cm the temperature of the fireball drops below the pair production threshold and the fireball becomes transparent to gamma-rays and capable of emitting non-thermal gamma-ray spectra[99, 102]. Accretion onto the compact object is expected to last longer than the light travel time across the injection region. This will create a series of sub-shells which cannot communicate

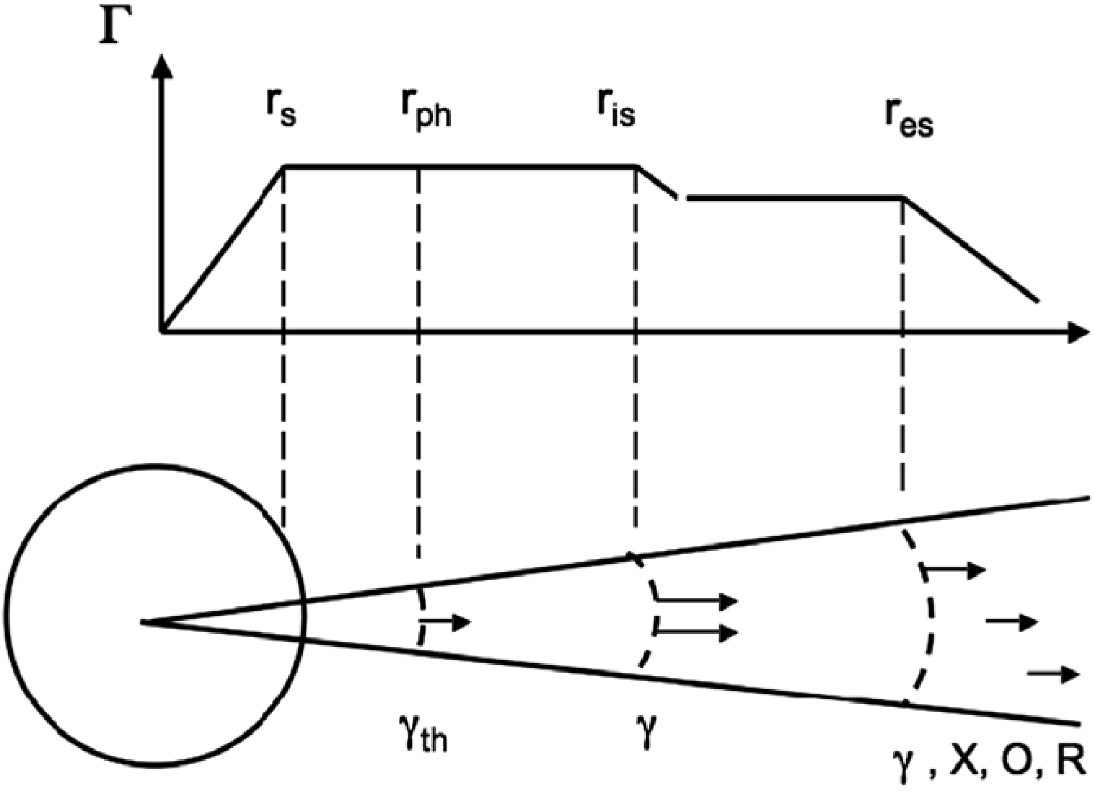

Figure 2.7: Simple diagram of the Fireball model. The outflow is constrained to a narrow jet. The fireball's Lorentz factor (Γ) increases until the saturation radius $r_s \simeq 10^8$ cm. Then the fireball coasts past the photosphere $r_{ph} \simeq 10^{11}$ cm until the internal shock radius $r_{is} \simeq 10^{14}$ cm where Γ decreases due to energy losses in internal shocks. The outflow then continues to coast until the ambient medium decelerates the fireball and creates external shocks at $r_{es} \simeq 10^{16}$ cm. Thermal gamma-rays may be observed at the photosphere, non-thermal gamma-rays at the internal shocks and the x-ray, optical and radio afterglow from the external shocks. Figure from [92].

with each other, and with different injected energies, hence different bulk Lorentz factors. These different sub-shells are expected to collide at a radius of $r_{is} \simeq 10^{14}$ cm and produce internal shocks. The different bulk Lorentz factor of two shells is a form of kinetic energy that can be converted to gamma-rays[103, 104]. These collisions will result in shock fronts. A significant portion of the fireball energy ξ_B is expected to build up in comoving magnetic fields due to turbulent dynamo effects in the shock[105], which will confine charged particles to the acceleration region. The shocks will also convert a fraction of the fireball's energy ξ_e to accelerated electrons with a power-law spectrum by first order Fermi acceleration. There are no theoretical models which can predict the equipartition fractions ξ_B and ξ_e, however if either were to be much smaller than one they would be inconsistent with observed gamma-ray emission[106, 107]. The Band function gamma-ray emission is often attributed to synchrotron emission by the accelerated electrons[108], however the exact mechanism for efficiently converting electron energy into the non-thermal radiation remains unclear[109]. The variability of injection by the central engine is thought to be the cause of the extreme variability observed in the light curves of GRBs[110, 111].

After the internal shocks, the fireball continues to expand. At a much larger radius $r_{es} \simeq 10^{16}$ cm, the mass of the Interstellar Medium (ISM) swept up by the fireball will be on the order of the total fireball energy[102]. Once this occurs the fireball will decelerate, causing further synchrotron energy loss which is observed as the afterglow. This deceleration can take weeks to years creating the long timescale observed in GRB afterglows. As the deceleration occurs, the average energy of the fireball decreases which causes the energy of the afterglow photons to decrease over time.

2.3 Compactness

The most important problem that the Fireball model solves is the compactness problem. GRB emission has been observed to vary on the order of milliseconds[54, 112] which imply that the sources are compact with a size of approximately $r_0 \simeq 10^7$ cm. It was originally observed by Ruderman[113] that GRBs are variable on a very short time scale which must be longer than the light crossing time of the object, however, the observed gamma-ray density would result in an optically thick pair plasma which would have a thermal black body spectrum. The Fireball model solves this by separating the central engine from the emission region. The bulk relativistic motion relaxes the constraint on the size of the emission region by a factor of Γ^2 allowing the emission to come from a much larger radius, and sparse enough to be optically thin[114].

However the time scale variability still leaves constraint on the central engine of $r < 10^8$ cm. The only object which can satisfy the energy requirements (10^{52} ergs) and size constraints is the rapid accretion of matter onto a solar mass size black hole after a cataclysmic event. There are two possibilities for the event: 1) a core collapse of a super massive star at the end of its life or 2) the merger of two compact objects, either neutron star-neutron star merger or a black hole-neutron star merger. The dynamics of these two possibilities lead to the conclusion that long

GRBs are the result of core collapses[95, 96], while short GRBs come from compact mergers[97]. The association of long GRBs with supernova[115, 116] as well as the observation that long GRBs always come from metal poor, star forming regions of galaxies[117] leads to the conclusion that long GRBs are a result of core-collapses of massive stars. Modeling of the dynamics of accretion disks leads to short emission time scales from compact mergers[118].

2.4 Relativistic Motion

Bulk relativistic motion is necessary to solve the compactness problem. Relativistic motion was first observed in GRB970508, its radio afterglow varied wildly until 4 weeks after the burst when it became stable[119]. This was caused by interstellar scattering where irregularities in the local interstellar medium scatter the incoming radio signal which results in a twinkling of the source. This effect disappears when the angular size of the emission region becomes large enough to prevent diffraction[120]. Knowing the angular size of the afterglow along with a redshift distance measurement allowed for an estimate on the size of the afterglow $\sim 10^{17}$cm, indicating that the fireball had expanded at relativistic speeds[121]. This effect has also been observed with GRB030329[122].

There are three methods for measuring the bulk Lorentz factor. In the first, the Fireball model predicts that there will be a smooth bump in the light curve of the afterglow when half of the fireball energy has been dissipated by the medium[123, 124]. This method has been used for many GRBs: $\Gamma \simeq 1000$ for GRB990123[125](see figure 2.4), $\Gamma \simeq 400$ for GRB060418 and GRB060607A[126], a constraint of $300 \lesssim \Gamma \lesssim 1400$ for GRB080319B[127], $\Gamma \simeq 300$ for a sample of four *Swift* bursts[128], a range from 79 to 610 for a sample of 19 bursts[129] and $\Gamma \simeq 195$ for GRB091024[130]. In the second method, observation of thermal photospheric emission can determine size of photosphere and Γ, this method obtains $\Gamma \simeq 305$ for GRB970828[131], $\Gamma \simeq 384$ for GRB990510[131], and $\Gamma \simeq 750$ for GRB090902B[132].

Bursts must have a Lorentz factor high enough so that pair production does not occur[133, 134]. Lower limits based on opacity to pair production were obtained for bursts observed with EGRET[135–138]. This method gives $\Gamma \simeq 200 - 700$ for GRB090926A assuming the peak in extended emission is caused by pair production[88](the range is caused by uncertainty in the model.) Lower limits were also reported for other *Fermi* LAT bursts: 900 for GRB080916C [85], 1200 for GRB090510[86], and 1000 for 090902B[87], these values should be a factor 3 lower using the model of [139] to compare with the lower bound of 090926A[88]. It is important to note that this method actually places a limit on $r_{is} = \Gamma^2 c t_{var}$, where t_{var} is the time scale of the variation in the central engine.

An upper limit on Γ can be obtained by requiring that internal shocks occur before external shocks[140], by studying the gamma-ray pulse width as a function of the pulse intensity[141], or by requiring that radiation not decouple from the fireball plasma[89]. All three requirements give an upper bound on the bulk Lorentz factor of $\Gamma \lesssim 1000$.

2.5 Beamed Emission

Beamed jets are necessary to explain GRBs, since the observed isotropic energy of many GRBs is $\sim 10^{54}$ ergs, which is difficult to explain from core collapses or from compact object mergers. If a burst is expanding with a Lorentz factor of Γ, then the light cone of outflow which is off of the line of sight by an angle $\theta > 1/\Gamma$ will not include the observer, hence the outflow will be indistinguishable from isotropic expansion[142]. Once the outflow has decelerated such that the edges of the jet become visible, then the jet can expand sideways and the luminosity will decrease with one power-law steeper than the isotropic expansion resulting in an achromatic jet break[143, 144]. Recent simulation confirms this simple analytical model[145]. Evidence for afterglows following the break was observed first in GRB980519[146], the first achromatic break was observed with GRB990510[147], see figure 2.8. Typical values of the beam opening angle are $2^\circ - 14^\circ$, which relax the energy requirement to the more reasonable value of $\sim 10^{51}$ ergs[144, 148]. This value of energy output is similar to the total output in a standard supernova, albeit in gamma-rays and within a much shorter time scale. This quantity of energy is also below the maximum theoretical output available for a collapsar[95, 149] or compact merger[150].

2.6 Neutrino Emission

Waxman and Bahcall first derived a neutrino flux from GRBs assuming $p\gamma$ interactions in the fireball after protons have been accelerated to UHECR energies with the same energy density as the electrons necessary to explain the gamma-

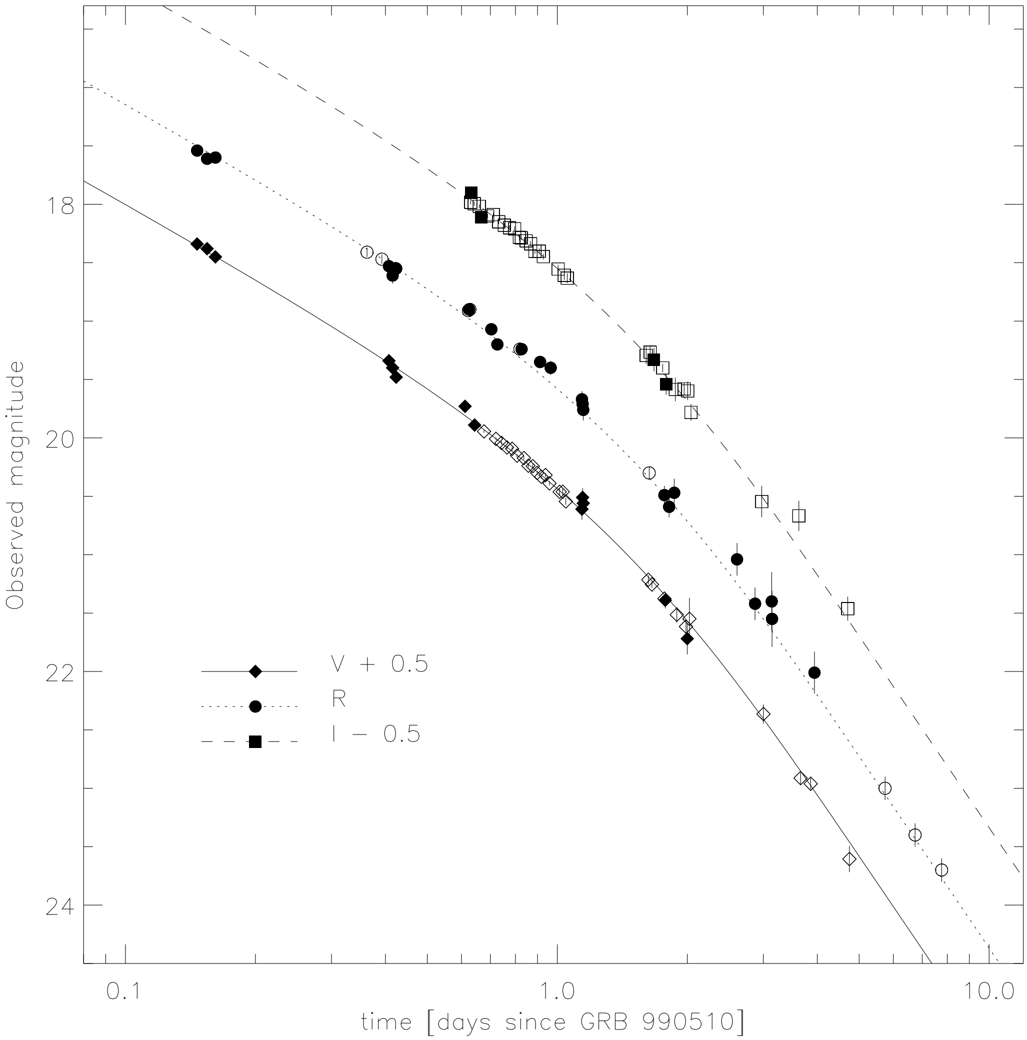

Figure 2.8: Light-curves of the optical afterglow of GRB990510. All three bands shown display a steepening at about 1 day after the trigger. This achromatic break is evidence for beamed emission in the GRB. Figure taken from [147].

ray emission[25]. This model was then refined by adding evolution and redshift losses[151] and synchrotron losses in muons and pions[26]. This analytical model is consistent with detailed simulations[152–155]. The model used in this analysis is a further refinement of the Waxman and Bahcall model derived by Guetta *et al.* which uses the observed gamma-ray flux and spectrum of each GRB to predict the neutrino flux and spectrum for each GRB[156]. This model is slightly below an upper bound on the neutrino flux which is calculated by assuming that all UHECR production results in neutrinos caused by photo-meson interaction which allow the protons to escape from the acceleration region known as the Waxman and Bahcall upper bound[151, 157]

Although most GRBs are reported with a power-law, power-law with an exponential cutoff, or Band function, for simplicity a broken power-law will be used here, so that the gamma-ray emission of a GRB is given by:

$$F_\gamma(E_\gamma) = \frac{\mathrm{d}N_\gamma(E_\gamma)}{\mathrm{d}E_\gamma \mathrm{d}A} = f_\gamma \times \begin{cases} \epsilon_\gamma^{(\alpha_\gamma - \beta_\gamma)} E_\gamma^{-\alpha_\gamma} & \text{for } E_\gamma < \epsilon_\gamma \\ E_\gamma^{-\beta_\gamma} & \text{for } E_\gamma \geq \epsilon_\gamma \end{cases} \tag{2.1}$$

Assuming protons are accelerated along with the electrons in the fireball to an E^{-2} spectrum, then protons will interact with the gamma-rays to produce pions via the delta resonance.

$$p + \gamma \rightarrow \Delta^+ \rightarrow n + \pi^+ \tag{2.2}$$

$$\rightarrow p + \pi^0 \tag{2.3}$$

Charged pions will then decay to neutrinos and associated leptons while neutral pions will decay into high energy photons.

$$\pi^+ \rightarrow \mu^+ + \nu_\mu \tag{2.4}$$

$$\mu^+ \rightarrow \bar{\nu}_\mu + e^+ + \nu_e \tag{2.5}$$

$$\pi^0 \rightarrow \gamma + \gamma \tag{2.6}$$

This produces a neutrino flavor ratio at the source of $(\nu_e : \nu_\mu : \nu_\tau) = (1 : 2 : 0)$. The decay of the neutron will also result in a $\bar{\nu}_e$, but since this neutrino only receives order 10^{-4} of its parent's energy it is not considered further. The energy threshold for Δ-resonance is

$$E'_p \geq \frac{m_\Delta^2 - m_p^2}{4E'_\gamma} \tag{2.7}$$

where prime indicates energy in the comoving fireball frame. Assuming that most interactions will occur at or close to the threshold energy, the inequality in equation 2.7 can be replaced by an equality. This derivation relies solely on the Δ resonance to produce neutrinos, including other $p\gamma$ interactions[158, 159] or reacceleration of particles[160] will increase the flux and result in a harder spectrum. When the pion decays into four leptons, the energy is distributed approximately equally. We assume the fraction of the energy from the proton to pion is approximately $\langle x_{p\rightarrow\pi}\rangle \simeq 0.2$. Switching back to the observer frame the energy of the neutrino is:

$$E_\nu = \frac{1}{4}\langle x_{p\rightarrow\pi}\rangle \frac{m_\Delta^2 - m_p^2}{4E_\gamma}\frac{\Gamma^2}{(1+z)^2} \tag{2.8}$$

Plugging equation 2.8 into equation 2.1 gives:

$$F_\nu(E_\nu) = \frac{\mathrm{d}N_\nu(E_\nu)}{\mathrm{d}E_\nu \mathrm{d}A} = f_\nu \times \begin{cases} {\epsilon_\nu^b}^{(\alpha_\nu - \beta_\nu)} {E_\nu}^{-\alpha_\nu} & \text{for } E_\nu < \epsilon_\nu^b \\ \\ {E_\nu}^{-\beta_\nu} & \text{for } E_\nu \geq \epsilon_\nu^b \end{cases} \tag{2.9}$$

with $\alpha_\nu = 3 - \beta_\gamma$ and $\beta_\nu = 3 - \alpha_\gamma$ and

$$\epsilon_\nu^b = \frac{1}{4} \langle x_{p \to \pi} \rangle \frac{m_\Delta^2 - m_p^2}{4\epsilon_\gamma} \frac{\Gamma^2}{(1+z)^2} \tag{2.10}$$

$$= 7 \times 10^5 \text{ GeV} \frac{1}{(1+z)^2} \left(\frac{\Gamma_{jet}}{10^{2.5}} \right)^2 \left(\frac{\text{MeV}}{\epsilon_\gamma} \right) \tag{2.11}$$

Synchrotron cooling in pions and muons must also be considered[26], the synchrotron cooling time, t_s, for pions and muons is:

$$t'_s = \frac{3 m_\pi^4 c^3}{4 \sigma_T m_e^2 E'_\pi U'_B} \tag{2.12}$$

where $\sigma_T = 6.65 \times 10^{-25} \text{cm}^2$ is the Thompson cross section. The magnetic energy density is $U'_B = B'^2/8\pi$. The fraction of the internal energy that goes into magnetic fields is denoted ξ_B, so that

$$\xi_B L_{int} = 4\pi R^2 c \Gamma^2 U'_B \tag{2.13}$$

The radius of the collisions can be estimated from the variability. If two shells collide with a difference in velocities of $\Delta v \simeq c/2\Gamma^2$ and a variability of t_{var}, the shells collide at a time $t_c \simeq c t_{var}/\Delta v$ at a radius of $R \simeq 2\Gamma^2 c t_{var}$[161]. Relating the internal luminosity to the observed gamma-ray luminosity, $\xi_e L_{int} = L_{iso}$, where ξ_e is the fraction of total energy that goes into accelerating electrons, the pion lifetime is:

$$\tau'_\pi = \tau^0_\pi \frac{E'_\pi}{m_\pi c^2} \tag{2.14}$$

$$\epsilon^s_\nu = \sqrt{\frac{12\pi m^5_\pi c^8 \Gamma^8 \xi_e t^2_{var}}{\sigma_T m^2_e \tau^0_\pi (1+z)^2 L^2_{iso} \xi_B}} \tag{2.15}$$

$$\epsilon^s_\nu = 10^7 \text{ GeV } \frac{1}{1+z} \sqrt{\frac{\epsilon_e}{\epsilon_B}} \left(\frac{\Gamma_{jet}}{10^{2.5}}\right)^4 \left(\frac{t_{var}}{0.01\text{s}}\right) \sqrt{\frac{10^{52} \text{ erg s}^{-1}}{L^{iso}_\gamma}} \tag{2.16}$$

The decay probability is approximated by the ratio of cooling time to decay time $t'_s/\tau' \propto E^{-2}_\nu$ so that the expected neutrino spectrum will steepen by two powers above ϵ^s_ν so that $\gamma_\nu = \beta_\nu + 2$. Adding synchrotron loss gives the final form of the neutrino spectrum:

$$F_\nu(E_\nu) = \frac{\mathrm{d}N_\nu(E_\nu)}{\mathrm{d}E_\nu \mathrm{d}A} = f_\nu \times \begin{cases} \epsilon^{b\,(\alpha_\nu - \beta_\nu)}_\nu {E_\nu}^{-\alpha_\nu} & \text{for } E_\nu < \epsilon^b_\nu \\ {E_\nu}^{-\beta_\nu} & \text{for } \epsilon^b_\nu \le E_\nu < \epsilon^s_\nu \\ \epsilon^{s\,(\gamma_\nu - \beta_\nu)}_\nu {E_\nu}^{-\gamma_\nu} & \text{for } E_\nu \ge \epsilon^s_\nu \end{cases} \tag{2.17}$$

where

$$\alpha_\nu = 3 - \beta_\gamma, \quad \beta_\nu = 3 - \alpha_\gamma, \quad \gamma_\nu = \beta_\nu + 2 \tag{2.18}$$

Since Fermi shock acceleration is independent of particle charge and mass, the normalization of the spectrum is obtained by assuming that the same amount of energy that went into accelerating electrons also went into accelerating protons. The gamma-ray fluence is defined as:

$$\mathcal{F}_\gamma = \int_{1\ \text{keV}}^{10\ \text{MeV}} \mathrm{d}E_\gamma\ E_\gamma F_\gamma(E_\gamma) \tag{2.19}$$

where the finite limits are necessary because some GRBs are reported with gamma-ray spectra that are divergent if integrated from zero to infinity. The fluence of neutrinos is then given by:

$$\mathcal{F}_\nu = \int_0^\infty \mathrm{d}E_\nu\ E_\nu F_\nu(E_\nu) = \frac{1}{8}\frac{1}{f_e} f_\pi \mathcal{F}_\gamma \tag{2.20}$$

The factor of 1/8 represents the fact that half of the photo-hadronic interactions result in leptons (the others produce π^0) and of those reactions that produce neutrinos the energy is distributed evenly between four leptons. There is also a factor of 1/2 and a factor of 2 which cancel: the reaction creates 2 muon neutrinos (ν_μ and $\bar{\nu}_\mu$) but then neutrinos oscillate from a ratio of $(\nu_e : \nu_\mu : \nu_\tau) = (1 : 2 : 0)$ to $(1 : 1 : 1)$[162, 163]. However, neutrinos at energies dominated by muon and pion losses will oscillate to $(1.8 : 1.8 : 1)$[164]. The $1/f_e$ accounts for the fraction of total energy in electrons compared to protons. f_π accounts for the fraction of proton energy lost to pion production, which can be estimated from the fraction of energy transferred from protons to pions $\langle x_{p\to\pi}\rangle$ and the estimated number of photo-meson interactions N_{int}:

$$f_\pi = (1 - (1 - \langle x_{p\to\pi}\rangle)^{N_{int}}) \tag{2.21}$$

N_{int} can be estimated from the size of the shock and the mean free path of a proton to photo-meson interactions

$$N_{int} = \frac{\Delta R'}{\lambda_{p\gamma}} = \Delta R' n_\gamma \sigma_\Delta \tag{2.22}$$

where n_γ is the number density of photons which is the ratio of the energy density to the photon energy in the comoving frame: for $R \simeq 2\Gamma^2 c t_{var}$

$$n_\gamma = \frac{U'_\gamma}{\epsilon'_\gamma} \simeq \left(\frac{L_\gamma t_{var}/\Gamma}{4\pi R^2 \Delta R'}\right) \Big/ \left(\frac{\epsilon_\gamma}{\Gamma}\right) \tag{2.23}$$

$$= \frac{L_\gamma}{16\pi c^2 t_{var} \Gamma^4 \Delta R' \epsilon_\gamma} \tag{2.24}$$

So that the number of interactions is given by:

$$N_{int} = \left(\frac{L_{iso}}{10^{52}\mathrm{ergs}^{-1}}\right)\left(\frac{0.01\mathrm{s}}{t_{var}}\right)\left(\frac{10^{2.5}}{\Gamma}\right)^4\left(\frac{\mathrm{MeV}}{\epsilon_\gamma}\right) \tag{2.25}$$

This model will be used as the expected signal flux for this analysis. There are a few things to note about this model. The model depends significantly on the fluence of the individual GRBs such that most of the flux will come from a handful of bright bursts[165, 166]. The model mainly depends on the measured gamma-ray flux, the measured cosmic ray flux and the unmeasured number of interactions between these components (N_{int}), thus, most of the uncertainty in this model comes from N_{int} which depends on Γ and t_{var}. Muon and pion synchrotron losses were added here for completeness, however, this does not become a concern until above 10^7 GeV where the event rate in IceCube is very low.

This model assumes that the observed gamma-rays are from a baryon dominated jet. An alternative theory is the Poynting flux dominated jet[150, 167–169] which does not accelerate baryons. If this model is true, then GRBs will not be the source of either UHECR or TeV scale neutrinos.

This model predicts that neutrinos will be emitted at the same time as the gamma-rays, and is therefore often called the prompt model. There are other models which predict neutrino emission from GRBs: low-energy precursor neutrinos[170, 171], TeV scale precursor neutrinos[172], low-energy neutrinos in the fireball[173], high-energy neutrinos in the afterglow[174–176], and low-energy neutrinos in afterglow[177]. All of these theories predict fluxes which result in much lower observable signal in IceCube than the prompt model and are not considered for this analysis. Additionally there are theories which use different emission to produce neutrinos in the fireball which predict prompt fluxes as well: photospheric emissions[178, 179] and synchrotron self-Compton emission[178]. There are also models in which GRB jets interact with the ejecta of a precursor supernova[180–183]. These theories are not significantly different from the prompt model to warrant a separate analysis.

Chapter 3

Gamma-Ray Detectors

This chapter provides a brief description of the gamma-ray detectors used in this analysis to observe GRBs. All of these detectors report their findings via the Gamma-Ray Coordinate Network (GCN)[184]. GCN distributes three kinds of messages: alerts, circulars, and reports. Alerts are written by the satellite's fight software which are machine readable and designed to alert telescopes to immediately repoint in response to GRBs. Circulars are follow up observations written by scientists after analyzing data and contain the most accurate position information, and also may contain fluence measurements and spectral fits. Reports summarize the results of all of the circulars for a GRB. This analysis relies solely on GCN circulars and reports for all information on GRBs. Using circulars and reports allows analysis of IceCube data to proceed before GRB catalogs become available.

3.1 *Swift*

Swift is a satellite designed primarily to study GRBs[185]. It consists of three instruments: the Burst Alert Telescope(BAT), the X-ray Telescope(XRT), and the Ultraviolet/Optical Telescope (UVOT). The BAT uses a coded aperture mask to scan the sky with a field of view of 1.4 sr and an energy response in 15-150 keV[186]. The coded aperture mask works by placing a pattern of lead tiles arranged into an array on a plate in front of a detector array. The detector array consists of a gamma sensitive array of CCD devices. The on-board computer reads out the charge pattern on the detector array and knowing the pattern of the coded aperture mask it can reconstruct an image of the gamma-rays incident on the detector.

Swift continuously scans the sky with the BAT. When the on-board computer detects a gamma-ray transient, it compares it with a catalog of known gamma-ray sources. If the detected transient is not in the catalog, it slews to point the XRT and UVOT to the transient. *Swift* uses momentum wheels to autonomously slew in the direction of GRBs. Slewing takes 20 to 75 seconds depending on the distance to the target. BAT localizations are on the order of 15 arc-minute. When the transient is in the x-ray telescope field of view, *Swift* searches for an x-ray point source. The XRT's energy range is 0.2-10 keV and can localize point sources to ~ 3.5 arc-sec[187]. If an x-ray source is found, the UVOT will search for an optical point source in the 170-650 nm band[188]. It can localize an afterglow to a 0.5 arc-sec accuracy. *Swift* detects an x-ray afterglow in 90% of GRBs and an optical afterglow in 33% of GRBs[93].

3.2 *Fermi*

Fermi Gamma-Ray Space Telescope is a wide field of view high-energy gamma-ray telescope. It consists of two instruments: the Large Area Telescope (LAT) and the Gamma-Ray Burst Monitor(GBM). The LAT is a pair converter detector with an energy sensitivity range of 20 MeV to 300 GeV [189]. Gamma-rays enter the telescope and produce e^+e^- pairs and these pairs are tracked with silicon strip detectors. It also contains a thallium activated cesium iodide [CsI(Tl)] calorimeter. Although the LAT has a large field of view, its energy threshold is too high to detect most GRBs. However, the high energy GRBs that it has detected have greatly improved our knowledge of GRBs. Only three GRBs detected by the LAT are included in this analysis. The LAT's spatial resolution allows for better localization than the GBM alone.

The secondary instrument on *Fermi* is the Gamma-Ray Burst Monitor (GBM)[190]. It consists of 12 thallium activated sodium iodide [NaI(Tl)] detectors optically coupled with PMTs. These detectors have an energy response of 8 keV - 1 MeV. In addition, there are 2 bismuth germinate (BGO) detectors with an energy range of 200 keV - 40 MeV overlapping in energy both the NaI(Tl) detectors and the LAT. The GBM can localize GRBs by utilizing the timing difference between the arrival times of gamma-rays in different NaI(Tl) detectors and the orientation of the detectors. The angular resolution is on the order of $1^\circ - 15^\circ$, which although too poor for x-ray or optical follow-up is well suited for correlating with neutrinos reconstructed with IceCube. *Fermi* was launched on June 15, 2008 and began issuing GCN circulars on August 10, so there are only bursts observed by *Fermi* for $\sim 60\%$ of the realtime of this analysis. Nevertheless, because of the GBM's all sky coverage, almost half of the bursts in this analysis were localized solely by GBM.

3.3 INTEGRAL

INTEGRAL is a satellite in a highly eccentric orbit with an apogee of 0.5 light-seconds[191]. It is designed to study gamma-rays. It contains three different coded aperture mask gamma-ray instruments. The Imager on board INTEGRAL (IBIS) uses a coded aperture mask to image the gamma-ray sky with an energy sensitivity of 15 keV to 10 MeV[192]. IBIS's field of view is much smaller than *Swift's* so it was only able to localized five bursts for this analysis. The Anti Coincidence Shield (ACS) on the SPI instrument consists of 91 BGO crystals[193]. The ACS is designed to serve as a veto for charged particles and gamma-rays outside the field of view of the SPI. The ACS consists of 91 BGO crystals with a collective mass of 512 kg. The ACS was not designed for imaging or spectral analysis of gamma-rays, however with its significant mass it is a very efficient all-sky GRB monitor. The time series of hits in the ACS can be used for GRB localizations by IPN (see section 3.7). The ACS is also used to verify weak GRB detections as seen in the IBIS. In this analysis, time series from the ACS were used to verify the beginning and end of gamma-ray emission in bursts where other detectors did not release such time series.

3.4 AGILE

The SuperAGILE instrument on the Agile Spacecraft consists of four square silicon detectors placed 14 cm from a tungsten coded aperture mask[194]. The detector can image an area of 0.8 sr in the range 10-40 keV. During IceCube-40 operation SuperAGILE localized 6 bursts in the northern hemisphere

3.5 Konus-Wind

Konus is a gamma-ray detector on board the GGS-Wind spacecraft[195]. GGS-Wind is in a halo orbit around the Earth-Sun Lagrange point L1 about 7 light-seconds from Earth. Its spin is stabilized perpendicular to the ecliptic. Konus-Wind consists of two hemispherical detectors placed such that the hemispheres remain pointed perpendicular to the ecliptic. Both detectors consist of a NaI crystal coupled to PMTs with an energy range 10 keV to 10 MeV. Konus-Wind reveals very little about the direction of a GRB but can provide very good spectral information for a burst localized by other means.

3.6 Suzaku WAM

The Suzaku satellite consists of two instruments: the X-ray Imaging Spectrometers and the Hard X-ray Detector. The anti-coincidence shield for the Hard X-ray Detector consists of 20 BGO detectors which are well suited to detecting gamma-ray bursts[196]. Referred to as the Suzaku Wide-band All-sky Monitor (WAM) it covers an energy range from 50-5000 keV[197]. Data is only transmitted to the ground when the satellite is over Japan so it cannot send GCN alerts immediately after detecting a burst. Like Konus, WAM data contains no directional information, but it can be used for timing and spectral information.

Detector	Energy Range	Field of View	Spatial Resolution
Swift BAT	15 – 150 keV	0.5π sr	$1' – 4'$
Fermi LAT	20 MeV – 300 GeV	0.8π sr	$0.1^\circ – 1^\circ$
Fermi GBM	8 keV – 40 MeV	2π sr	$1^\circ – 15^\circ$
INTEGRAL IBIS	15 keV – 10 MeV	0.5π sr	$1' – 2'$
INTEGRAL SPI-ACS	> 75 keV	4π sr	—
SuperAGILE	15 – 45 Kev	0.3π sr	$1' – 2'$
Konus Wind	10 keV – 10MeV	4π sr	—
Suzaku WAM	50 keV – 5 MeV	2π sr	—
IPN	—	4π sr	$0.1^\circ – 10^\circ$

Table 3.1: Summary of Gamma-Ray Detectors used in this analysis. Fields of view are approximate. Spatial resolution are typical values for GRB localization.

3.7 IPN3

The Third Interplanetary Network (IPN3) is a network of satellites that have gamma-ray detectors[198]. Timing data from multiple detectors can be combined to localize bursts. At the time of this analysis, IPN's configuration consisted of 9 spacecraft: AGILE, *Fermi*, Suzaku, and *Swift* in low Earth orbit; INTEGRAL in eccentric Earth orbit with an apogee of 0.5 light-seconds; Wind in halo orbit 7 light-seconds from Earth; MESSENGER traveling to Mercury; and Mars Odyssey orbiting Mars. The timing information from two satellites will restrict the burst to an annulus in the sky. Two such annuli will restrict the location to two points in the sky. Earth occultation can be used to resolve the degeneracy. If one of the observing satellites is Konus, the ratio of hits in the two hemispheres can also resolve the degeneracy. Often two of the satellites will be in low Earth orbit, which results in similar annuli causing the location to be a long skinny banana shaped box.

Table 3.1 shows a summary of the gamma-ray observatories used in this analysis.

Chapter 4

IceCube

Neutrinos have cross sections much smaller than all other particles, so in order to observe neutrinos, it is important to build very large detectors. Although astrophysical neutrino sources may be emitting neutrinos at lower energies, the search for astrophysical neutrinos should focus on the TeV scale. There are two reasons to focus on this scale. First, this is the lowest energy scale in which astrophysical neutrinos could be seen amongst the ever present background of atmospheric neutrinos[199]. Second, this is the energy scale where muon neutrino interactions acquire a pointing angular resolution and neutrinos can be traced back to their source; the median angular difference at this scale between the muon secondary and neutrino primary is $\sim 0.7^\circ \times (E_\nu \mathrm{TeV})^{-0.7}$[200]. In addition, at this scale the secondary muons will have long tracks on the order of 10 km[201]. However, at the flux level predicted for astrophysical neutrinos, even accounting for the long tracks of muons, the size of the detector required is on the order of a cubic kilometer to observe astrophysical neutrinos. The only possible way to build such a detector would be to take advantage of a naturally occurring transparent medium such as deep ocean water or glacial ice.

The IceCube Neutrino Observatory was built with these design goals in mind[202, 203]. It instruments a cubic kilometer of deep Antarctic glacial ice located near the

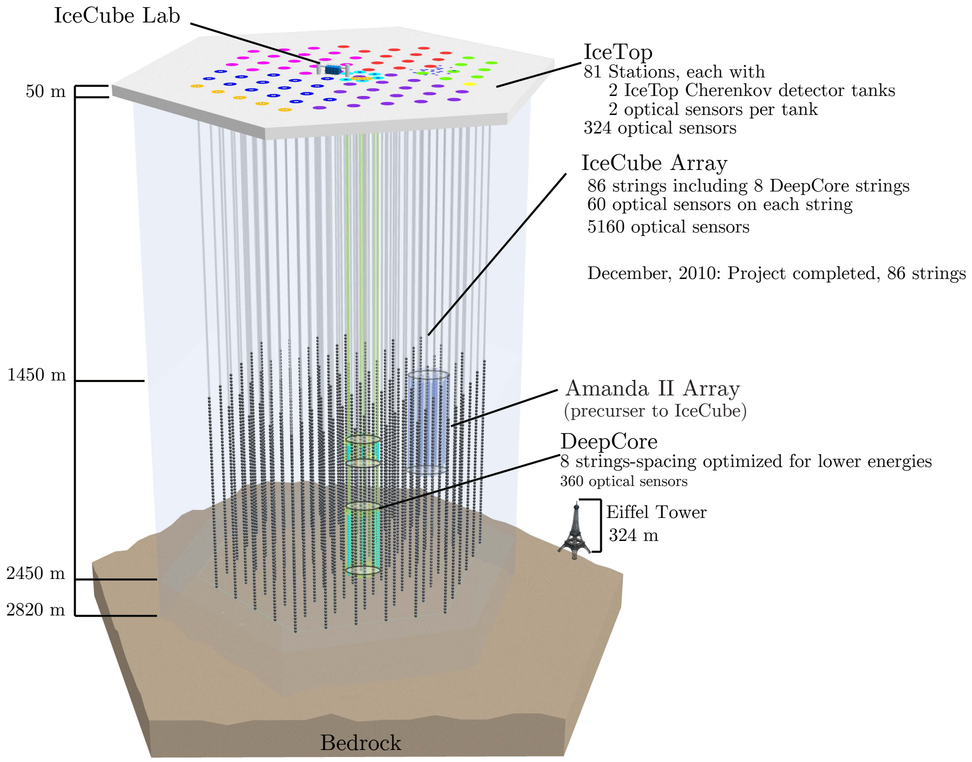

Figure 4.1: Schematic diagram of IceCube. IceCube consists of 86 vertical strings each containing 60 DOMs. On their surface there are 81 IceTop stations each consisting of two tanks each with two DOMs. At the center the vertical and horizontal DOM spacing was decreased in order to create the low-energy sub-detector Deep Core[205]. IceCube's now decommissioned predecessor AMANDA-II[206, 207] is also shown. The Eiffel Tower is shown for size comparison. Figure from [208].

geographic South Pole, as shown in figure 4.1. The ice sheet at this location is approximately 2.8 km deep. However, above a depth of 1400 m the optical properties of the ice are dominated by scattering off of hydrate bubbles[204], so IceCube is instrumented between a depth of 1450 m and 2450 m. Power and other infrastructure is provided by the Amundsen-Scott South Pole Station.

4.1 Hardware

The IceCube detector is constructed by hot water drilling into deep glacial ice. As the drill is lowered into the ice, it releases hot water to melt the ice and creates a column of water. Once the drill reaches the bottom of the glacier it is reeled back up. An IceCube string is then lowered into the column of water. Each string contains 60 Digital Optical Modules (DOMs) spaced 17m apart. The strings use a steel cable as a strength element. There is also a communications cable that connects to each DOM carrying power and communications via twisted pair wires to each DOM. The bottom of each string is lowered to roughly 2450 m below the surface.. The string is then anchored in place while the ice refreezes, which typically takes two to three weeks. Once the water refreezes, the DOM becomes optically coupled with the ice.

In total, IceCube has 86 strings. 78 of the strings are placed 125 meters apart in a hexagonal grid pattern, 8 additional strings were placed inside the hexagonal grid near the center of the array to form a high density region known as Deep Core[205]. Due to weather constraints at the South Pole, the construction could only occur during the Austral summer which lasts a few months out of the year. In between construction seasons, the detector operated with the installed strings collecting physics quality data. This analysis uses data collected from April 2008 to May 2009, while IceCube was collecting data with 40 strings, see figure 4.2.

Each DOM (shown in figure 4.3) is housed in a pressure sphere that can withstand the 300 atmospheres pressure at the bottom of the detector[210]. For

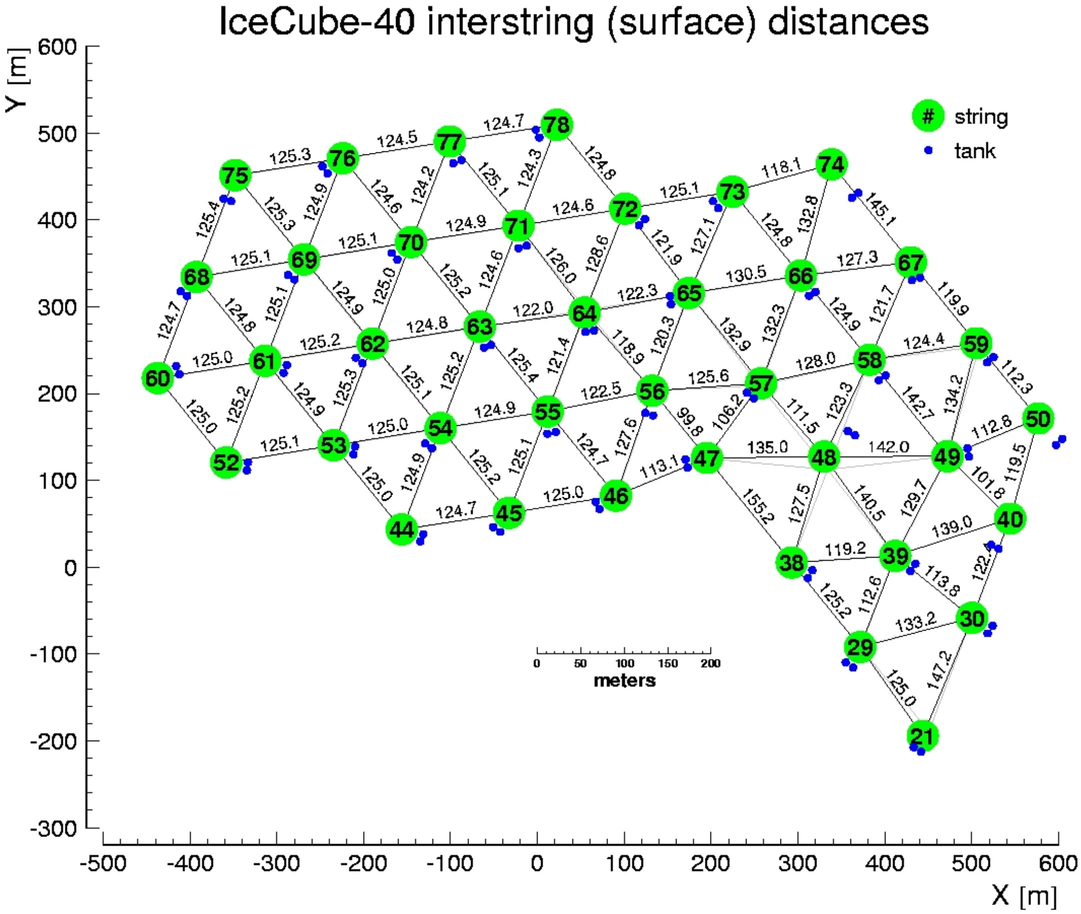

Figure 4.2: The Geometry of IceCube in its 40 string configuration with distances between adjacent strings shown. Green circles indicate the location of in ice strings, while blue circles represent IceTop surface array tanks. Figure from [209].

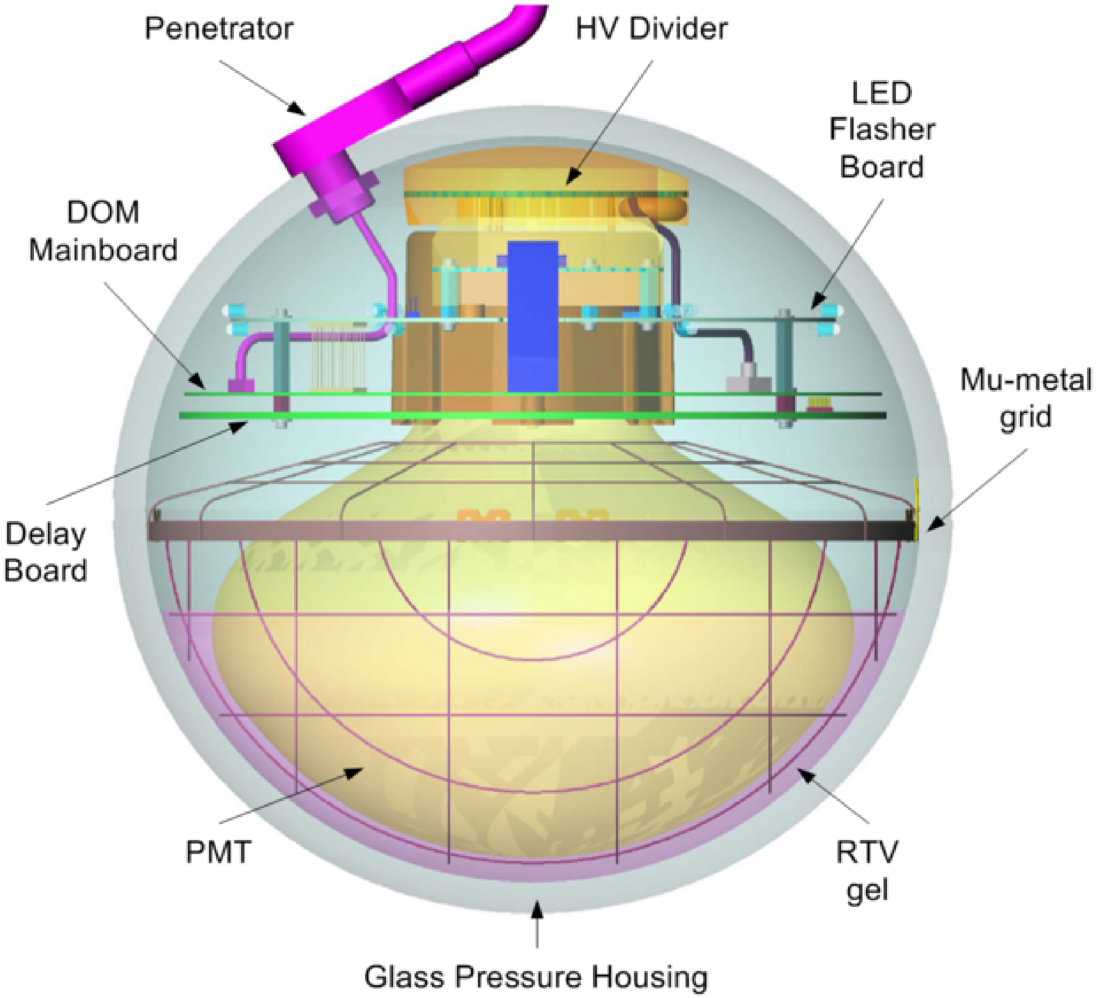

Figure 4.3: Schematic view of an IceCube DOM. Each DOM is a self contained unit for detecting light. The DOM is housed in a glass pressure vessel to withstand the pressure of a 2.5 km column of water. The DOM receives communication and power through a penetrator cable. The PMT is encased in a mu-metal grid and coupled to the glass with optical gel. High voltage is supplied by a step up transformer. A flasher board holds LEDs to transmit light to other DOMs for calibration purposes. Digitization of the PMT signal, control of the flasher board and high voltage board, as well as communications with the surface are all handled by the mainboard. Figure from [211].

the detecting light, IceCube uses the R7081-02, a 10" hemispherical photomultiplier tube manufactured by Hamamatsu Photonics, Japan. The PMTs are coupled with optical gel to the pressure vessel and encased by a mu-metal grid to decrease the effect of the Earth's magnetic field on electrons inside the PMT. It has a Bi-alkali photo-cathode (peak QE 25% at 420 nm) and 10 dynode stages which produce on the order of 10^7 gain at a bias of approximately 1400 V. The PMT has a noise rate of approximately 500 Hz in the low temperature of the glacial ice.

The DOMs each contain four circuit boards[212]. The mainboard contains all the required circuitry to measure the signal from the PMT, digitize it and communicate with the surface. It has both a micro-controller and FPGA to quickly process data. It contains two digitization systems, the fADC and the ATWD. The Fast Analog to Digital Converter (fADC) digitizes the signal from the PMT every clock cycle (25 ns). The flasher board contains twelve 405 nm LEDs which are aimed in various directions. These LEDs can be flashed during special calibration runs. By analyzing the arrival time and amplitude of light from one flashing DOM to another receiving DOM, the distance between the two DOMs can be measured as well as the properties of the ice between the DOMs. The delay board contains one long trace to delay the signal so data from before the time of the trigger can be digitized. The high voltage board contains the necessary circuits in order to step up the voltage supplied from the surface to the voltage required to power the PMT. This variable voltage supply is controlled by the mainboard. During calibration the voltage is varied to find a voltage vs gain curve. During normal operation each DOM sets its high voltage independently so that all the DOMs have the same gain of 10^7.

When a signal greater than approximately 0.25 photoelectrons is detected by the fADC, then the DOM triggers and the DOM triggers the ATWD (analog transient waveform digitizer) starts capturing data. The ATWD consists of an array of 256 very low capacitance capacitors. The ATWD continuously connects each capacitor to the signal for a brief time (3.3 ns) in sequence, so that the capacitors now hold a time series of the signal in their charge that can be read out later. If the digitization conditions are met, then the ATWD connects each capacitor to an analog-to-digital converter in sequence to get a time series of the voltage on the anode as a function of time, binned in 3.3 ns bins. Digitizing the ATWD takes time and since most triggers are noise, the data is not necessarily digitized every time there is a trigger. A launch occurs when the digitization conditions are met. The DOMs use a system of local coincidence signals between neighboring DOMs on a string to determine when to launch. If a DOM triggers and one of its two nearest neighbor DOMs or one of the two next-to-nearest neighbor DOMs triggers within 1000 ns, then the local coincidence condition is met and both DOMs launch. To increase the dynamic range of the digitizer, each ATWD has three channels with different gain on the input amplifier. The gains are 16, 2 and 0.25, there is also a fourth channel that is used only for calibration signals. The channels are read out in order of high-gain to low-gain and the low-gain channels are only read out if the higher-gain channel saturated. The digitization process takes 29 μs if all three channels are read out. Each DOM is equipped with two ATWDs so that if a trigger occurs while the DOM is digitizing one ATWD then it can use the second ATWD to capture the second trigger. Once a DOM is finished digitizing the ATWD, it creates a packet of data. The packet contains the timestamp of the trigger and digitization of both the ATWD and the fADC (the fADC was continuously taking data while the ATWD was digitizing). This packet is then sent to the surface to be analyzed by the Data Acquisition (DAQ) software.

On the surface, the communication cable of each string is connected to a computer called a DOMHub. The DOMHub controls the DOMs, provides power, and holds data sent by the DOMs. Each DOMHub has a buffer in which it stores the packets of data sent to it by the DOMs.

In order to reconstruct events in IceCube, accurate timing is very important. The relative time when a photon hits a DOM must be known to order nanosecond accuracy. Overall timing accuracy has been determined to be at least as good as 3 ns[211] (the same timescale as the width of an ATWD bin). The DOM's internal clock signal is generated by a crystal oscillator with a nominal rate of 40 MHz. Due to clock drift in the oscillator, the DOM's clock has to be continuously recalibrated. In order to accomplish this, the DAQ will periodically send a calibration pulse, called a RAPCal pulse, to each DOM separately. When a DOM receives a RAPCal pulse, it sends an identical pulse back to the DOMHub. Since the DOM and DOMHub use identical hardware to send and receive RAPCal pulses (reciprocal hardware) then it can be assumed that the time it takes to reach the DOMHub from the DOM is half the round trip time. Using data from RAPCal, both the time offset from travel and the clock drift of the DOM's crystal oscillator can be measured and corrected. The DAQ continuously sends RAPCal pulses and dynamically updates its calculation for clock drift so that launch times are as accurate as possible.

When a DOMHub receives a launch from a DOM, it sends the timestamp of the launch to the trigger system. The trigger system continuously scans the data trying to form a detector trigger. A detector trigger occurs when more than 8 launches occur within a 5000 ns window. When a detector trigger occurs all launches within the window are bundled into a unit called an event. Then if the trigger condition is met for longer than the trigger window, the event is extended as long as there are 8 events in a window of 5000ns. The trigger system also adds all other hits within a 10μs window before and after the limits of the trigger condition. These events are written to the Online Processing and Filtering (PnF) system discussed in the next section. Launches which do not form part of an event are lost when the buffer is overwritten.

4.2 Online Filter

The PnF system receives events from the DAQ. Every event that the DAQ event builder assembles gets written to tape at the South Pole. In addition, data is sent from the South Pole to the University of Wisconsin using NASA's Tracking and Data Relay Satellite System (TDRSS). However, the bandwidth available on TDRSS is significantly less than IceCube's total output. IceCube is swamped by a background of downgoing cosmic ray air-shower muons which are the background for neutrino searches. Downgoing events trigger the 40 string IceCube configuration at about 1000 Hz while atmospheric neutrinos occur at a rate of about 1 mHz. In order to meet the bandwidth requirement of TDRSS, the data must be reduced in order to send the neutrino stream over the satellite.

The PnF system performs a series of reconstructions discussed in section 4.4 on each event. Neutrino candidates which reconstruct as upgoing pass the filter and are sent north for immediate analysis, see chapter 6 for more details.

4.3 Simulation

In order to understand how IceCube responds to neutrinos, it is necessary to produce simulations. The IceCube Collaboration has developed a software package that simulates both the high energy particle physics processes which IceCube detects and IceCube's hardware. The IceCube simulation chain starts by generating a primary particle, for example a neutrino from a GRB. Monte Carlo simulation techniques are used to properly sample the direction, location and energy space of the primary particle. In this analysis two types of primary particle event generators are used for simulation: neutrino-generator for simulating GRB neutrinos and CORSIKA[213] for cosmic rays. Simulated cosmic rays are not used in the unbinned analysis discussed in chapter 7, however since the majority of events seen in IceCube are from cosmic rays, the cosmic ray simulation is useful for verifying the validity of both the simulation and any processing which is performed on data. The CORSIKA package generates cosmic ray primaries with the composition and energy spectrum from the Polygonato model[214] based on the parameterization of [215], it then calculates all daughter particles from the primary interacting with the atmosphere. Since muons are the only resultant particles which can penetrate the

1.5 km of ice between the surface and IceCube, these are the only particles which are tracked.

Neutrino-generator is used to calculate neutrino interactions in the Earth and in and around the detector, it is based on code from ANIS[216]. It starts with neutrinos sampled uniformly on the surface of the Earth with a power-law spectrum. The neutrinos are then propagated through the Earth taking into account absorption, scattering, and neutral current regeneration of neutrinos. This code uses the cross section from CTEQ5[217] to simulate neutrino-nucleon interactions, see figure 4.4. The daughter muon and nuclear recoil are calculated based on deep inelastic scattering. The structure of the Earth is taken from the Preliminary Reference Earth Model[220]. Neutrino-generator then randomly places a neutrino interaction vertex in or near the detector volume and calculates the probability of this interaction occurring. A Monte Carlo weight is then calculated from this probability and the expected neutrino spectrum. For atmospheric neutrinos, the Honda 2006 model[221] is used for pion and kaon decay induced neutrinos and the Naumov RPQM model[222] used for charmed lepton decay. The Honda 2006 model is based on simulations performed for lower energy neutrino experiments, it is extended to higher energy using the analytic model[223, 224]

$$\phi_\nu(E_\nu) \propto E_\nu^{-2.7} \left\{ \frac{A_{\pi\nu}}{1 + B_{\pi\nu}\cos(\theta)E_\nu/\epsilon_\pi} + \frac{A_{K\nu}}{1 + B_{K\nu}\cos(\theta)E_\nu/\epsilon_K} \right\} \tag{4.1}$$

Where $\epsilon_\pi = 115$ GeV and $\epsilon_K = 850$ GeV are the decay constants, the energy where a particle in an atmospheric air shower is more likely to interact rather than to

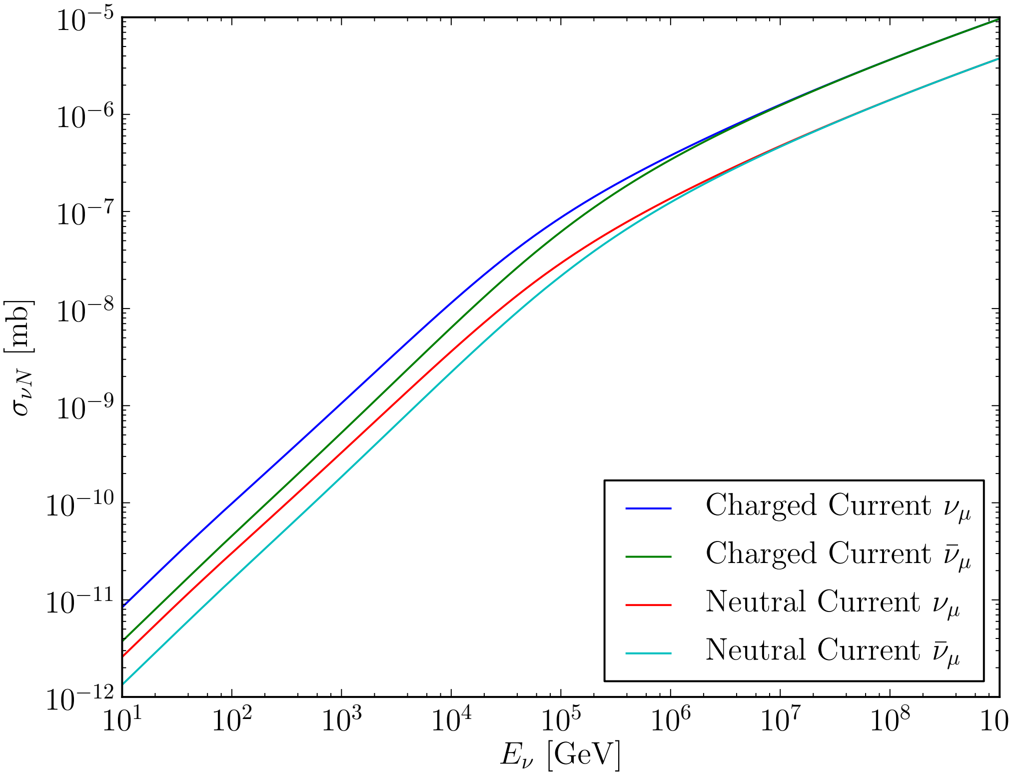

Figure 4.4: Neutrino-nucleon cross section for muon neutrinos as a function of neutrino energy (E_ν). All interactions are calculated using deep inelastic scattering with CTEQ5[217]. Only charged current (CC) interactions produce muons which can be detected, however neutral current (NC) interactions must be accounted for in losses while propagating neutrinos through the Earth. At low energies ($E_\nu \ll M_w^2/2M_N$) the cross section is proportional to E_ν, while at higher energies ($E_\nu \gg M_w^2/2M_N$) the interaction is damped by the W-boson propagator and the cross section becomes proportional to $E^{0.363}$. Above $\sim 10^6$ GeV the contribution from valence quarks becomes negligible compared to sea quarks so that the neutrino and anti-neutrino cross sections become equal[218, 219].

decay. The values $A_{\pi\nu}$,$B_{\pi\nu}$,$A_{K\nu}$ and $B_{K\nu}$ are considered free parameters set to get a smooth transition to the Honda model. This model has been shown to accurately produce the atmospheric neutrino flux observed in IceCube[208].

In addition to neutrinos generated with random directions, this analysis uses simulation where each individual GRB is simulated. For each GRB, 10^5 events are simulated where the direction of the primary neutrino is in the direction of the GRB with a random 2-dimensional Gaussian offset, where the width of the Gaussian is the GRB's localization uncertainty. The time of the neutrino is generated randomly from the on-source time of the GRB in question. The losses in the Earth and detector is calculated identically to the random direction neutrino simulation. Finally, the GRB simulation is weighted based on the primary spectrum of neutrinos from GRBs that is derived in section 2.6.

Once the primary has been generated and the daughter muons calculated, the rest of the simulation chain proceeds identically for both neutrinos and cosmic rays. Muon propagation above 1 TeV is extremely stochastic and is dominated by bright events where a significant fraction of the energy is lost[201]. The MMC[225] package is used to propagate muons. It assumes a baseline continuous energy loss and randomly adds stochastic energy to the track based on the probability of such events occurring. The values of energy loss it uses to simulate muons is plotted in figure 4.5.

Since the muon is moving faster than the speed of light in the medium, the energy lost by the muon will radiate as Cherenkov radiation[226, 227]. Since the ice in which IceCube was built does not have uniform optical properties, there is no an-

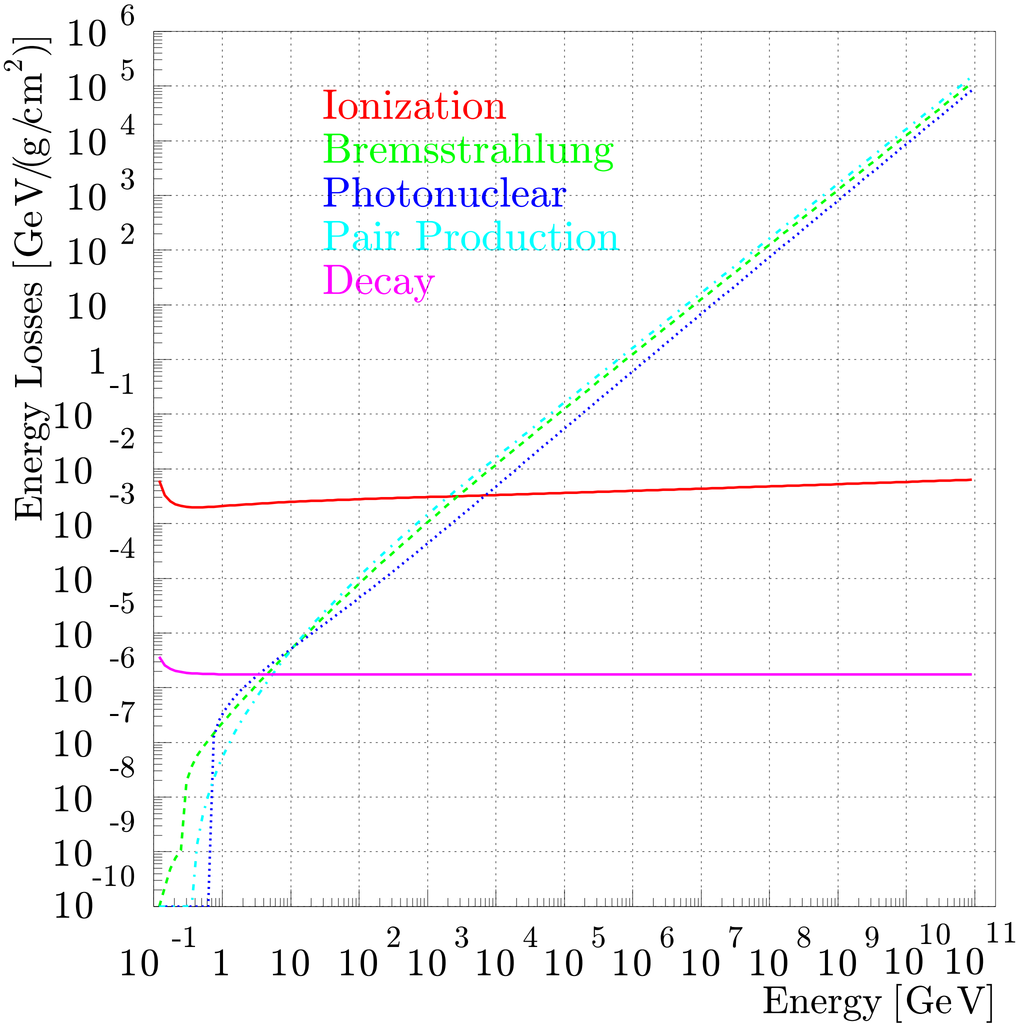

Figure 4.5: Average energy losses for a muon traveling through ice. The four types of losses are ionization, bremsstrahlung, photo-nuclear interaction and pair production, decay is also shown. Ionization losses are weakly dependent on energy, while bremsstrahlung, photo-nuclear and pair production, which dominate at energies above a TeV, are proportional to the muon's energy. Figure taken from [225].

alytic solution to approximate photon propagation through the ice. It is impractical to individually propagate all photons emitted from a muon track. The only way to obtain a reasonable description of light yield in the DOMs is to propagate a large number of photons beforehand and histogram their location into tables that describe the probability of a photon propagating from the track to the DOMs. This is done by a program called photonics[228]. Photonics breaks all space and time around the origin into bins. Then it uses Monte Carlo simulation to propagate photons through the space considering both scattering and absorption which are both functions of depth in the ice. As the photon propagates, equidistant recording points are generated along its path. The probability of observing a photon emitted from the origin is calculated as the number of counting points in each bin normalized by the total number of counting points generated. Since the ice model is not uniform, this procedure must be repeated for each location where light is to be emitted. However, since the ice model only varies in the vertical direction (shown in figure 4.6), the horizontal symmetry can be exploited and this procedure is only repeated by moving the light source in the vertical direction. This procedure creates the cascade tables which are used for calculating the light yield from the stochastic, point-like light emission in the muon's track. To calculate the light yield from continuous muon losses, many small cascades are assembled into a track shape and the cascade tables are added together and normalized to create a table of light yield as a function of track zenith angle, position, and time. Both the continuous losses and stochastic losses are used to calculate light yield at each DOM from the muon whose propagation track was calculated by MMC.

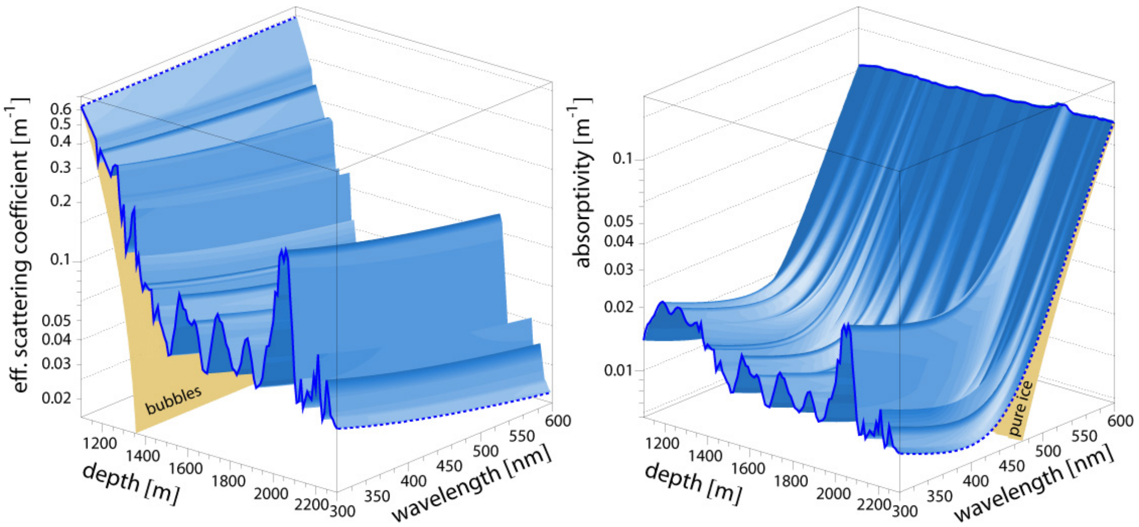

Figure 4.6: Maps of optical scattering and absorption for deep South Pole ice. The depth dependence between 1100 and 2300 m and the wavelength dependence between 300 and 600 nm (left) for the effective scattering coefficient and (right) for absorptivity are shown as shaded surfaces, with bubbles contributing to the scattering and the pure ice contributing to the absorption superimposed as (partially obscured) steeply sloping surfaces. The dashed lines at 2300 m show the wavelength dependences: a power-law due to dust for scattering and a sum of two components (a power-law due to dust and an exponential due to ice) for absorption. The dashed line for scattering at 1100 m shows how scattering on bubbles is independent of wavelength. The slope in the solid line for absorptivity at 600 nm is caused by the temperature dependence of intrinsic ice absorption. Figure from [204].

Discrete photon hits incident on the PMT surface are calculated from the probabilities obtained from photonics tables. In addition to the pulses caused by direct photon hits incident on the photocathode, other pulses may appear in the PMT: pre-pulses, after-pulses, late-pulses, and noise pulses[229] which are simulated as well. Hits are then converted to an analog current on the PMT's anode, which is then propagated through the DOM's front end electronics simulation to a voltage as measured by the DOM's two analog-to-digital converters. Then the digitization is simulated, as well as the DOM's triggering and logic to create a launch. Launches which do not meet local coincidence conditions are discarded. All of the launches from each DOM are combined and evaluated using software to simulate the DAQ. The simulation is then stored in a file with an identical format as is used for data, which allows data and simulation to be processed and reconstructed using identical processing software.

4.4 Event Reconstruction

The process of turning the data recorded by the DOMs into the direction and location of a track is called reconstruction. Figure 4.7 shows visual representation of IceCube events along with their reconstruction. The energy loss of a muon traveling through IceCube and the behavior of the light as it propagates through the ice are stochastic processes. The basic strategy will be to use a series of statistical estimators, starting with the simplest, least CPU intensive reconstruction. This is then followed by more complex, more accurate and more CPU intensive reconstructions.

Along the way, events that do not look like desirable events will be cut from consideration and will not be reconstructed with the more CPU intensive reconstructions.

4.4.1 Hit Reconstruction

The data collected by the fADC and ATWD can be used to calculate the number of photoelectrons by each DOM. A photoelectron is an electron that is created in the photocathode of the PMT and represents a discrete amount of charge recorded by the DOM. The time series of voltages on the anode of the PMT will be transformed into reconstructed photoelectron pulses, called reco-pulses. These reco-pulses contain the time that the pulse occurred, the number of photoelectrons contained in the pulse, and the width of the pulse. In order to convert from voltage to number of photoelectrons, the gain of the PMT as well as the gain of the transformer and amplifiers which couple the anode to the digitizers must be known.

First, each capacitor in the ATWD has an offset or pedestal voltage, which must be measured separately for each ATWD by shorting the ATWD (setting the voltage to zero) and measuring the charge. Once the pedestal is known the pedestal can be subtracted from each readout to get a corrected value. Next, effects in the front-end electronics must be compensated. The ATWD is inductively coupled to the anode of the PMT with a transformer. Early DOMs had a high inductance which resulted in pulses with a large number of photoelectrons to undershoot zero as the voltage dropped after the pulse, an effect known as transformer droop. After this

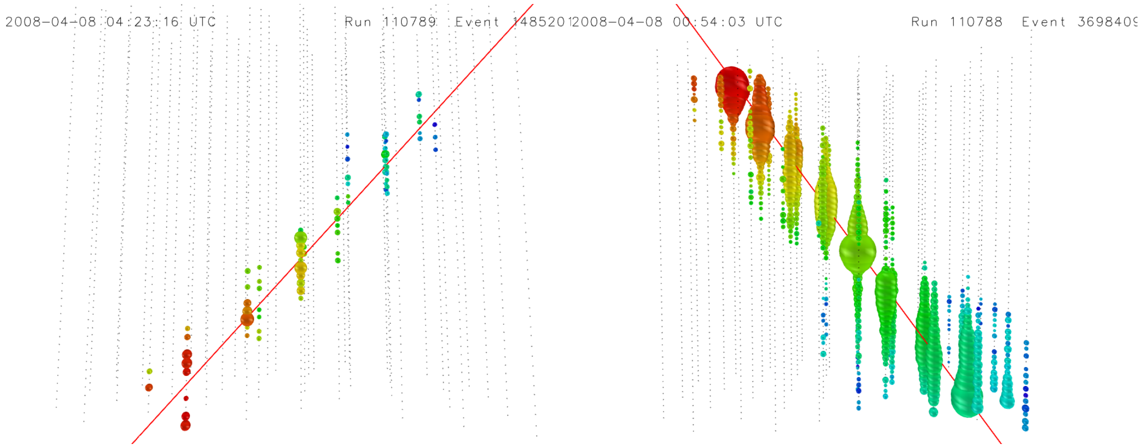

(a) Muon Neutrino Candidate (b) High Energy Cosmic Ray Muon Bundle

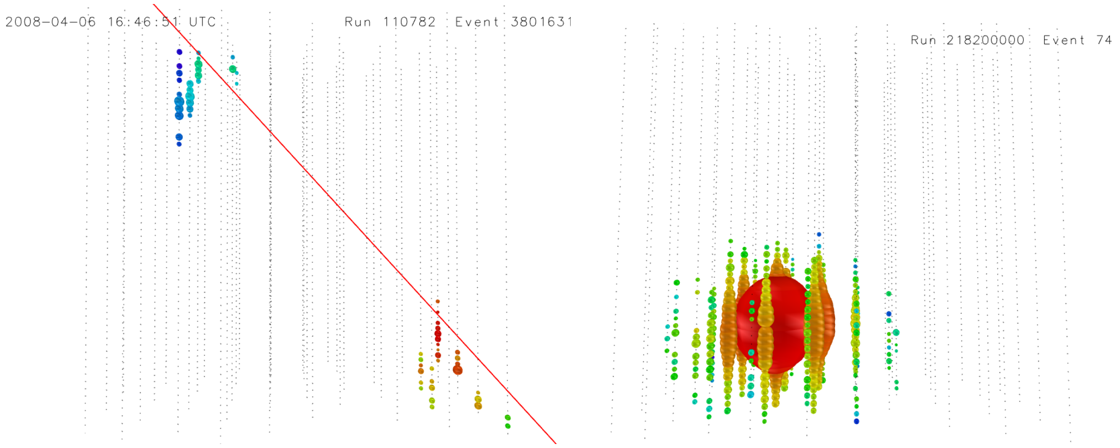

(c) Coincident Cosmic Ray Muon Bundles (d) Simulated Electron Neutrino Cascade

Figure 4.7: Visual representation of events in the IceCube detector. The colored spheres indicates observed hits where the color represents the time of the hit with red being earlier and blue later. The size of the sphere indicates the number of hits. The MPE reconstruction (section 4.4.4) is shown as a red line. (a) An upgoing muon neutrino candidate. (b) A downgoing high energy muon bundle. (c) Two downgoing cosmic ray muon bundles hit the detector in such a way that the MPE reconstruction incorrectly reconstructs the event as upgoing. (d) Simulated 3 EeV electron neutrino cascade.

effect was identified, the front-end electronics were modified to reduce this effect, but there is still a noticeable inductance in the circuit. Thus, to reconstruct the current on the anode, the transfer function of each DOM's input circuit must be corrected[230]. Finally, the high voltage and gain of the DOM are used to express the voltage measuring the DOM as a function of photoelectrons.

Next a feature extraction algorithm is used to turn the time series into discrete pulses. This algorithm has a DOM response template which predicts the voltage as a function of time for a pulse at a given time and amplitude[231] The time of the pulse is assumed to be the extrapolation of a straight line to the baseline of the rising edge of the pulse. Then the height of the pulse is used to determine how many photoelectrons are contained in the pulse. The feature extraction algorithm identifies upward slopes in the calibrated waveform as initial guesses for the time and amplitude of pulses. Then it uses an iterative Bayesian unfolding algorithm[232] to find the best match between the template and the observed waveform. Figure 4.8 shows an example of results from the feature extraction algorithm. A series of recopulses is saved with the corresponding time and charge of each pulse found for every DOM which launched in the event.

Since IceCube's trigger window includes all hits which occur within $10\mu s$ of the beginning or end of a trigger, there are often noise hits which are unrelated to the muon which triggered the event. To remove theses noise hits a procedure called time window cleaning is performed. The algorithm slides a time window with a constant length along the events time axis until it finds the time window with the most reco-pulses and keeps only the reco-pulses within this window. Based on the

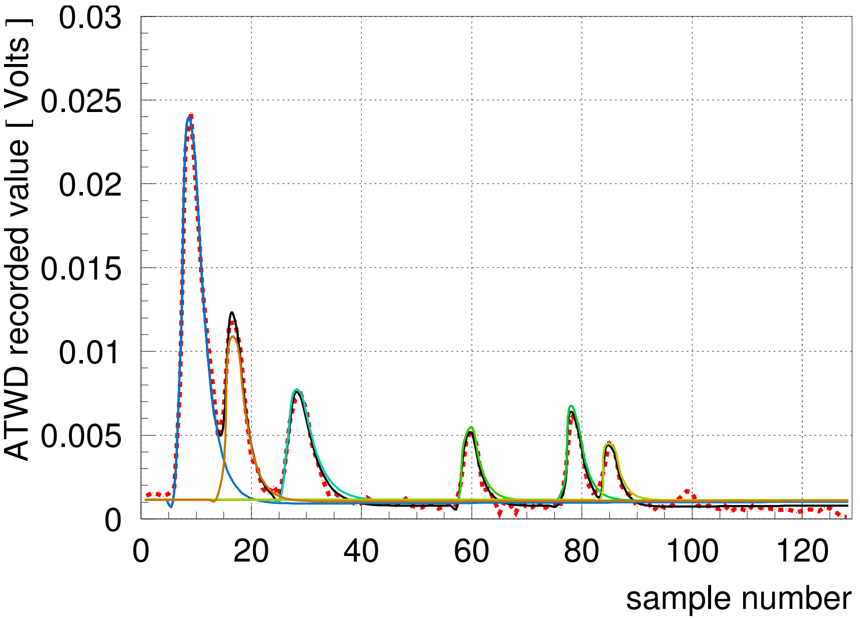

Figure 4.8: A sample waveform is shown with the red dotted line. Each sample represents approximately 3.3 ns. Each reconstructed pulse is represented as a different color solid line. Figure from [231].

size of the detector, it was determined that 6μs was longer than physically related reco-pulses could be separated in time and was therefore chosen as the length of the time window.

4.4.2 LineFit

The first reconstruction performed is called LineFit. LineFit makes the assumption that the light generated by a muon is a plane wave traveling in the same direction as the muon. This nonphysical assumption has the advantage of offering an analytic solution; a χ^2 minimization of a plane wave hitting a series of detectors can be solved exactly. For a series of detectors each located at $\vec{r_i}$, hit at a time t_i, and a muon with a vertex $\vec{R}$, and velocity $\vec{V}$ the solution is

$$\vec{V} = \frac{\langle \vec{r_i} t_i \rangle - \langle \vec{r_i} \rangle \langle t_i \rangle}{\langle t_i^2 \rangle - \langle t_i \rangle^2} \tag{4.2}$$

$$\vec{R} = \langle \vec{r_i} \rangle - \vec{V} \langle t_i \rangle \tag{4.3}$$

Although LineFit's median angular resolution is $\sim 5°$, it is analytic and therefore it is very quick to perform and can be used to seed subsequent reconstructions which require an initial first guess.

4.4.3 SPE

Reconstructions which use more realistic light propagation models than LineFit do not have closed form analytic solutions, so all further reconstructions use the method of maximum likelihood estimation. If the probability of observing a hit at time t on a DOM at location $\vec{r}$ from a muon with vertex $\vec{R}$, zenith angle θ, azimuth angle ϕ, and energy E is

$$P(\vec{r_i}, t_i | \vec{R}, \theta, \phi, E) \tag{4.4}$$

then the likelihood of observing a hit at t_1 at $\vec{r}_1$ and t_2 at $\vec{r}_2$ etc. is

$$\mathcal{L}(\vec{r}_1, t_1, \ldots, \vec{r}_n, t_n | \vec{R}, \theta, \phi, E) = \prod_{i=0}^{n} P(r_i, t_i | \vec{R}, \theta, \phi, E) \tag{4.5}$$

The most likely path of the muon is obtained by maximizing the logarithm of likelihood function with respect to $\vec{R}$, θ, and ϕ for an observed $\vec{r}_1, \ldots, \vec{r}_n$ and $t_1, \ldots, t_n$.

Since the MINUIT[233] software package does not have functions to maximize functions, only functions to minimize functions, the negative of the log of likelihood will be taken and this method will hereafter be referred to as minimum log-likelihood or least log-likelihood.

Although this method is the most accurate estimator, it has numerous potential pitfalls. Numeric minimizers require a first guess and move along the parameter space until they find a local minimum, they do not look for the global minimum. The minimizers may also get stuck in saddle points or extremely flat regions even though a good minimum may be available elsewhere. A PDF that describes all aspects of light propagation in ice, in addition to requiring intensive CPU computation, would be very complicated and create a likelihood space that is very bumpy and hard for the minimizer to navigate. For this reason a simplified PDF to describe light propagation was developed. This function, called the Pandel function, was derived by analyzing isotropic monochromatic light[234, 235] shown in figure 4.9.

$$p_{pandel}(t_{res}) = \frac{(t_{res})^{d/\lambda - 1}}{\Gamma(d/\lambda)\left(\frac{1}{\tau} + \frac{c_{medium}}{\lambda_a}\right)^{-d/\lambda}} \exp\left[-t_{res}\left(\frac{1}{\tau} + \frac{c_{medium}}{\lambda_a}\right)\right] \tag{4.6}$$

Where t_{res} is the time a photon is measured to hit a DOM minus the time expected for an unscattered photon, t_{geo}:

$$t_{\text{res}} = t_{\text{hit}} - t_{\text{geo}} \tag{4.7}$$

The Pandel function is a modified form of the gamma distribution[236]. The un-

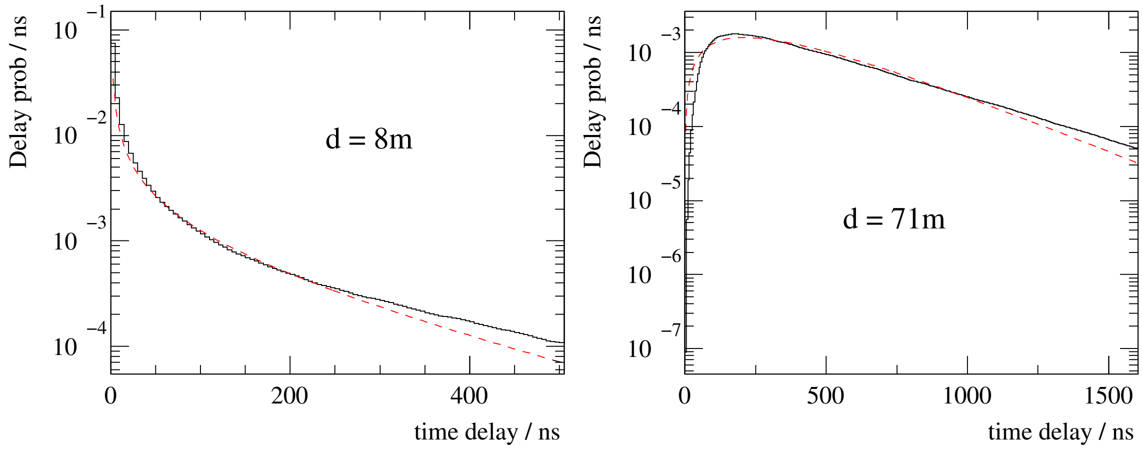

Figure 4.9: Comparison of the Pandel function (dashed curves) with the detailed simulation (black histograms) at two distances d from the muon track. The Pandel function offers a good analytic model for light propagation. Figure taken from [235].

scattered photon time from a Cherenkov cone can be calculated from geometry, see figure 4.10:

$$t_{geo} = t_0 + \frac{\hat{V} \cdot (\vec{r_i} - \vec{r_0}) + d \tan\theta_c}{c_{\text{vac}}} \tag{4.8}$$

λ_a is the scattering length, τ and λ are unspecified parameters that were empirically determined:

$$\tau = 557\text{ns}, \tag{4.9}$$

$$\lambda = 33.3\text{m}, \tag{4.10}$$

$$\lambda_a = 98\text{m}, \tag{4.11}$$

$$d_{\text{eff}} = a_0 + a_1 d, \tag{4.12}$$

$$a_0 = 3.1 - 3.9\cos(\eta) + 4.6\cos^2(\eta)m, \tag{4.13}$$

$$a_1 = 0.84 \tag{4.14}$$

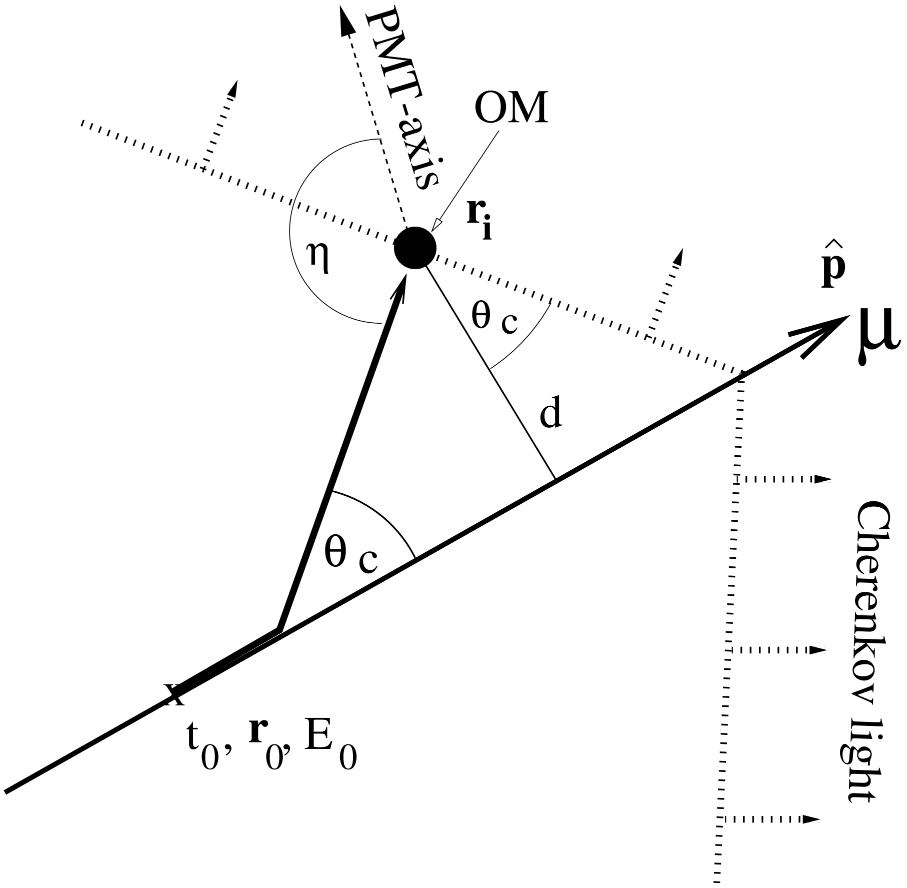

Figure 4.10: The Geometry used to reconstruct the photon travel time. For a muon which travels through $\vec{r}_0$ at time t_0 and emit light in a Cherenkov pattern with angle θ_c[226, 227], the expected hit time for an unscattered photon is given by equation 4.8. Figure taken from [235].

Where it is necessary to replace d with d_{eff} to account for the fact that light traveling toward the bottom of a DOM can hit the PMT directly, while light traveling in the opposite direction must be scattered in the reverse direction to hit the PMT. The time it would take an unscattered photon to hit the DOM from the Cherenkov cone based on geometry is t_{geo}. When a photon is observed to hit a DOM the residual time, t_{res}, is defined as the hit time minus t_{geo}:

This is a good function to approximate photon arrival time, but it has a few drawbacks. It is zero for all $t_{res} < 0$ and can be singular at $t = 0$ for smaller values of d. Because of both effects in the PMT, when signals are propagated through the PMT faster than expected and the errors in the time calibration procedure, it is not uncommon to get hits with negative t_{res}. To accommodate this, the Pandel function is convolved with a Gaussian. This allows for negative values of $t_{res} < 0$ and removes the possible discontinuity at $t_{res} = 0$.

$$p_{conv}(t_{res}) = \int_{-\infty}^{\infty} \frac{1}{\sqrt{2\pi}\sigma_{Jitter}} \exp\left[-\left(\frac{t_{res} - t}{\sigma_{Jitter}}\right)^2\right] p_{pandel}(t)\mathrm{d}t \tag{4.15}$$

Where σ_{Jitter} is the width of the Gaussian to convolved with the Pandel function. In theory, σ_{Jitter} should be the total uncertainty in the hit time. However, there are other reasons why an event may have a hit such as a noise hit or a PMT prepulse. For this analysis, it was found empirically that $\sigma_{Jitter} = 15$ ns gives the best reconstructions.

There are two reconstructions which compensate for the fact that the minimizer may pick a local minimum and not the global minimum. The first is the half sphere reconstruction which performs two minimizations: one confined to the upgoing hemisphere and the other confined to the downgoing hemisphere and it picks the minimum with the lowest value. In the second, thirty two directions are randomly selected for the initial value of the minimization and the best minimization is picked. Since performing minimization based reconstructions accounts for the majority of the computer time used to reconstruct data, the number of iterations needs to be optimized. For the 40 string configuration, the best trade off between computer time spent minimizing and finding the global minimum was found to be 32 iterations. Both of these techniques will prevent reconstructions which are in directions very far from correct, but will not improve the angular resolution of reconstructions that were correct the first time.

4.4.4 MPE

The PDF used for reconstruction in section 4.4.3 is correct only if a single photon hits the DOM. However, if multiple photons hit the DOM it is still simpler to use only the first photon from each DOM in the reconstruction. This is justified since the first photon is less likely to have scattered significantly, therefore it contains more information than later photons. MPE is a correction to SPE given the Bayesian prior that the photon you are looking at is the first of N, not a random photon. The correct PDF for the first photon, when a DOM is hit by n photons, is:

$$MPE(t_{res}) = n \cdot SPE(t_{res}) \cdot \left[\int_{t_{res}}^{\infty} SPE(t)\mathrm{d}t\right]^{n-1} \tag{4.16}$$

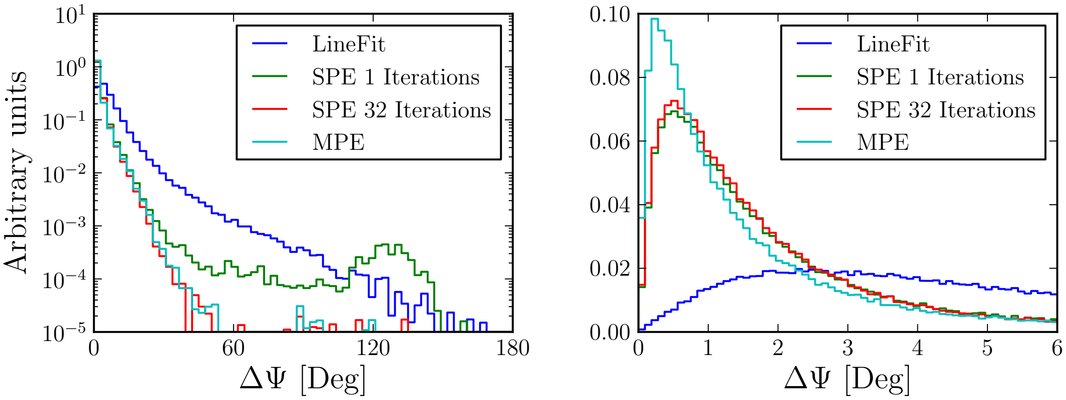

Figure 4.11: Comparison between the angular resolution of different reconstructions. Left: the angle difference ($\Delta\Psi$) between a simulated muon track and the reconstructed direction. Right: same plot zoomed in the low angle portion. LineFit has a soft peak at a larger angle than the minimization based reconstructions as well as a much larger tail. SPE with 32 iterations is almost identical to SPE with a single iteration at small angles but shows significant improvement at larger angles. Since MPE uses SPE with 32 iterations as its seed, its large angle behavior is very similar to SPE with 32 iterations, but it shows significant improvement at smaller angles.

Computing this integral is computationally intensive, however, accurate approximations[237,238] have been devised that allow this PDF to be calculated in a reasonable amount of time. Using a minimization with this PDF can be more accurate if it is close to the correct solution, but since it is more complicated, it will often have more local minimum. To solve this, a reconstruction with SPE is performed followed by the MPE reconstruction using the results of the SPE fit as a seed, so that MPE fits are run with only one iteration. A comparison between the MPE, SPE with 32 iterations, SPE with one iteration, and LineFit is shown in figure 4.11.

4.4.5 Paraboloid

The paraboloid fit is a reconstruction designed to estimate the angular uncertainty of a minimization based reconstruction[239]. It starts with the results of an MPE reconstruction, then forms a grid of points in a 4° by 4° region of zenith and azimuth space. For each point on the grid, paraboloid does a 3 parameter MPE fit, where zenith and azimuth directions are fixed, but the X,Y, and Z location of the vertex are varied. It then creates a two dimensional function of log-likelihood in zenith and azimuth space. Near the 2-dimensional minimum the log-likelihood function should have a paraboloid shape. The paraboloid reconstruction fits this space to a paraboloid using a χ^2 minimization. When the log-likelihood function is half the value at the minimum, it should correspond to the 1σ contour line. Thus, paraboloid calculates the 1σ error ellipse around the minimum. Paraboloid diagonalizes this ellipse to find the major axis length and the minor axis length. For well reconstructed events, the ellipse should have a low eccentricity, and it is simpler to deal with one error radius denoted σ_ν.

$$\sigma_\nu \equiv \sqrt{\frac{1}{2}\left(\sigma_1^2 + \sigma_2^2\right)} \tag{4.17}$$

Where σ_1 and σ_2 are the semi-major axis and the semi-minor axis. σ_ν is taken as an overall measure of event reconstruction quality. Due to a mismatch between the Pandel function and the real arrival time distribution of photons, there was a slight energy dependent mismatch between the paraboloid error and the true error, this was corrected using a method developed by the point source working group[240].

4.4.6 Bayesian Fit

Some reconstructions are not designed to be the best estimator of a parameter. In order to identify events that have been erroneously reconstructed as upgoing but were caused by downgoing events, the Bayesian Reconstruction is used. The Bayesian reconstruction is intentionally biased in the zenith direction. Using Bayes's theorem

$$P(\theta|a) = \frac{P(a|\theta)P(\theta)}{P(a)} \tag{4.18}$$

and interpreting $P(a|\theta)$ as the convolved pandel function from section 4.4.3 and $P(\theta)$ as the probability of observing a background event with zenith angle θ:

$$P(\theta) = A_0\,(\cos\theta)^{A_1}\exp\left(-\frac{A_2}{\cos\theta}\right) \tag{4.19}$$

Where A_0,A_1, and A_2 are fit empirically to the observed distribution of downgoing cosmic ray muons and P(a) ensures proper normalization. The probability of an event with track parameters a and with zenith angle θ can be calculated. Using this $P(\theta|a)$ as the PDF in a minimization reconstruction will result in a reconstruction that is biased in the zenith direction to the downgoing region. Events that were caused by downgoing events but were erroneously reconstructed by SPE as upgoing often lie in shallow minimum so that their biased reconstruction will usually result in a minimum of similar depth or deeper. Events caused by true upgoing particles will be poorly reconstructed when biased in this fashion so that the depth of the minimum will be significantly worse than with the unbiased function. Thus the difference between the depth of the SPE32 reconstruction and the depth of the Bayesian weighted reconstruction will become a powerful cut parameter to separate upgoing from downgoing events.

4.4.7 Energy Reconstruction

All of the preceding reconstructions were used to reconstruct the direction of muon events. Since the spectrum of GRB neutrinos is expected to be harder than the background of atmospheric neutrinos, an energy reconstruction will help to differentiate signal from background. Energy reconstruction is possible because above $\sim$ 1TeV muon losses are dominated by processes whose cross section is proportional to the energy of the muon (see figure 4.5), thus the energy loss will be a good proxy for the total muon energy. Reconstruction of the energy of the muon is performed by reconstructing the average energy loss per unit track length ($\mathrm{d}E/\mathrm{d}X$) of the muon[241, 242]. This energy of the muon as it travels through the detector is a lower bound on the original neutrino's energy as the neutrino's interaction vertex may have occurred far from the detector resulting in energy losses between the vertex and the detector. Since muons may lose a significant fraction of their energy on a length scale the size of IceCube, the energy of the muon in a particular event is dependent on the location of the muon during the event. It has been determined that the energy of the muon as it makes its closest approach to the event's center of gravity (CoG) is the most suitable definition of the muon's energy, denoted $E_{\mu,\mathrm{CoG}}$. The center of gravity for an event is defined as the mean of the locations of all

DOMs which were hit in that event.

The preceding reconstructions all used the arrival time of the first photon for each DOM, as the first photon is most likely to have not scattered than the subsequent photons, thus the first photon carries more information about the direction of the muon than later photons. To reconstruct the energy loss of the muon, all observed photons must be accounted for in order to get an accurate measure of the amount of energy deposited in the ice by the muon. In addition, the preceding reconstructions used a PDF that assumed light propagation that is uniform throughout the detector. This assumption does not affect timing as much as it affects the number of photons that arrive. In order to successfully reconstruct the energy, it is necessary to account for the depth dependence of scattering and absorption of the ice. To accomplish this, photon reconstruction or photorec tables were created. These tables contain the PDF of photon arrival binned in time, the distance of the DOM from the muon track, the muon track zenith angle, and the z position. Photorec tables are based on the photonics tables which are used for simulation discussed in section 4.3, but they differ in two ways: they are more coarsely binned so that a typical computer can load the entire table into memory at once, and they simultaneously account for stochastic and continuous energy losses which are handled separately in photonics tables. The energy reconstruction uses a 1 dimensional likelihood reconstruction to estimate the average energy loss along the track obtained from the MPE fit. Thus, having an accurate direction reconstruction before attempting energy reconstruction is very important to getting an accurate energy.

The exact relationship between $\mathrm{d}E/\mathrm{d}X$ and $E_{\mu,CoG}$ must be determined from simulation. Since there is a large spread in this relationship, confidence intervals[243–245] are used. Using simulation discussed in section 4.3 weighted with the spectrum from section 2.6, the distribution of $\mathrm{d}E/\mathrm{d}X$ for each value of $E_{\mu,CoG}$ is calculated and 1σ (68%) central confidence limits are calculated, see figure 4.12. Splines are used to create a continuous function to convert $\mathrm{d}E/\mathrm{d}X$ to the $E_{\mu,CoG}$ and find the 1σ error estimate. These functions would have been used as an estimate of the energy of individual neutrino events had any significant events been observed.

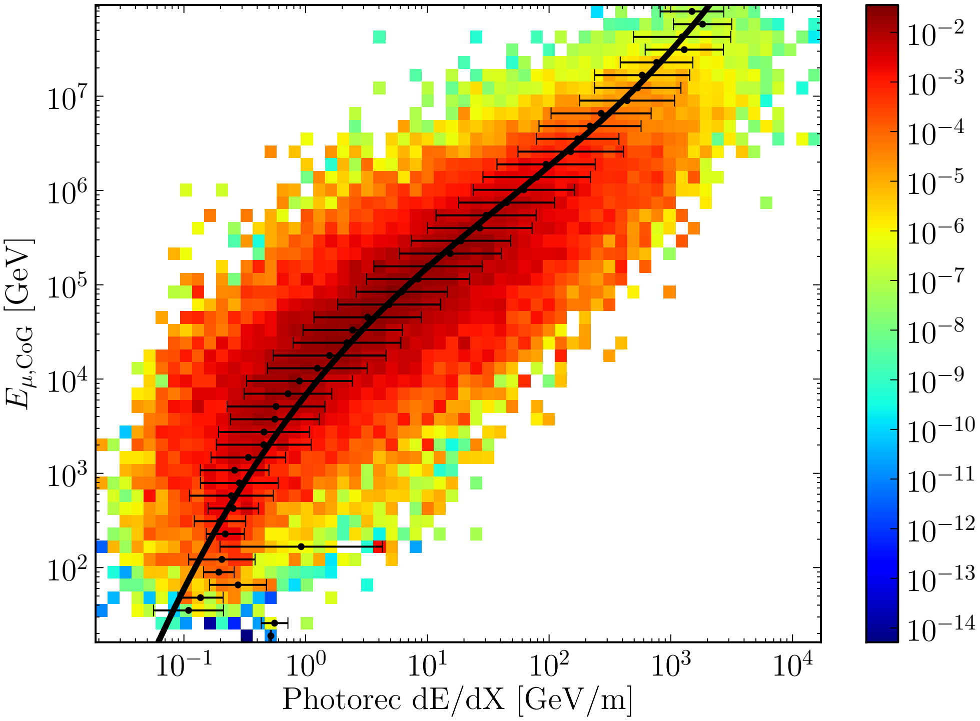

Figure 4.12: The energy resolution of the detector is measured using simulation. On the y-axis is the simulated muon's energy as it passes closest to the center of gravity of the hits it causes ($E_{\mu,CoG}$). The y-axis is the reconstructed energy loss per unit length of the muon ($\mathrm{d}E/\mathrm{d}X$). The color map shows the density of simulated neutrino events weighted to the expected GRB spectrum. The black error bars show the full-width/half-max of the distribution of $\mathrm{d}E/\mathrm{d}X$ for each $E_{\mu,CoG}$ bin. The black line shows the spline fit to the center of each $\mathrm{d}E/\mathrm{d}X$ distribution. Inverting the error bars to be errors on measuring the energy gives errors on measuring the energy of $\Delta\log(E_{\mu,CoG}) \sim 0.3 - 0.4$

Chapter 5

GRB Selection

Although the satellites that observe GRBs produce catalogs of bursts, these catalogs are often not available within the timescale needed to analyze IceCube data in a timely fashion. Thus, this analysis was performed with a custom catalog of GRBs produced from data gathered in GCN circulars[184].

This catalog includes bursts that occurred during the 410 days between April 5, 2008 and May 20 ,2009, when IceCube was operating in its 40 string configuration. During this time there were 277 bursts reported via GCN, of those 128 had a declination in the Northern Hemisphere. Several of the *Fermi* GRBs were removed from the catalog because they did not report a gamma-ray fluence or because the burst was extremely weak and poorly localized. Four bursts with no fluence measurement were kept, three of them were detected by SuperAGILE, which does not report fluence measurements, and one *Fermi* GBM burst detected, GRB081110, where *Fermi* reported only that it was bright and hard[246].

5.1 Detector Stability

It was necessary to remove certain bursts because IceCube was not operating in a state to record reliable data. GRB080521 and GRB090515 were removed because they occurred during calibration runs which used the DOM LED flashers, and

GRB081113 occurred while IceCube was down for maintenance. During GRB090422 and GRB090423, IceCube was running a test mode in the 59 string configuration. These bursts were treated as 59 string data and were considered in the 59 string analysis instead of this analysis.

Several GRBs needed special checks to ensure high quality data was obtained. For example, several hours after GRB081024A a door was left open in the IceCube lab which caused the computers running in the server room to freeze. This resulted in data loss, however, there is no discernible effect on data within 1 hour of the burst. The Dust Logger is a laser apparatus that is lowered into the IceCube hole before the new string is deployed. It shines laser light horizontally into the ice and measures the level of reflected light to produce a map of the density of dust in the ice. The Dust Logger was operated 25 minutes after GRB090107A occurred, the extra light in the detector caused the data acquisition system to crash, but there is no indication of any detector problems before the dust logger was used. In the run in which GRB090401A occurred, string 70 suffered communication problems and many hits from string 70 were lost, but the rest of the detector was operating normally. Since the impact of this problem was minimal, it was decided that this GRB would be included in the analysis without further modification.

Since, in some instances, this analysis examines data during segments of time which are short compared to the standard eight hour run, extra care must be taken to make sure the detector was not acting anomalously for these segments. In order to examine this, the rate of the muon filter (discussed in section 6.1) is used to indicate any anomalies. The normal muon filter rate is dominated by misreconstructed downgoing atmospheric air shower muons. This rate is dependent on the density of the upper atmosphere[247,248], because, in order for an air shower to create a muon, a charged meson must decay, and in a denser atmosphere, charged mesons are more likely to interact with an air nucleus rather than decay[249]. This effect, shown in figure 5.1, creates a seasonal variation in the muon filter rate with an amplitude of approximately 20% of the maximum rate. Thus, the rate fluctuates and is maximum during the austral summer when the atmosphere is less dense, and minimum during the austral winter when the atmosphere is denser. To look for any variations in the detector's performance on the scale of minutes, all of the events within a two hour time window about the bursts were histogrammed as a function of time into bins with a width of one minute. The results, shown in figure 5.2, indicate no unusual behavior.

Data from June 2008 suffered from a bug in the online cascade filter, which did not affect any of the data used in this analysis. However, data from this period was reprocessed from tape. This caused some data losses due to physical damage to the tape, which resulted in a few 3 minute segments of data becoming corrupt. Two such gaps were found close to GRBs: one instance during GRB080607 and another instance fifteen minutes before GRB080603A. In the case of the former, the data was replaced by the original satellite transmitted data with the bug in the cascade filter. In the latter case, no action was taken as it was outside the on-source time window. No further anomalies in the rate were observed.

Any detector anomaly should also become apparent by looking at the distribution time intervals between subsequent events (Δt). If the events occur randomly in

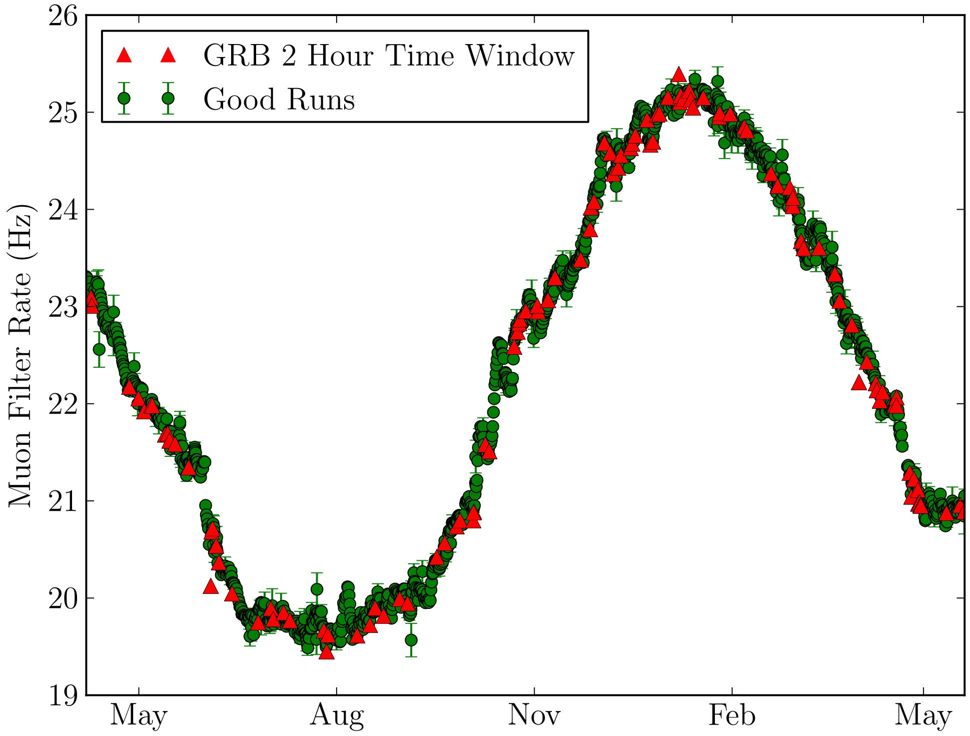

Figure 5.1: The green circles indicate the muon filter rate for all IceCube runs flagged as good runs during the 40 string operations which fluctuates with the downgoing muon rate. The seasonal variation due to changes in air density is apparent. The red triangles indicate the muon filter rate during the 2 hour time window around GRBs. Almost all are consistent with the rate around them. A few outliers are observed: GRB090107A, GRB090401A, and GRB080603A all of which are discussed in the text.

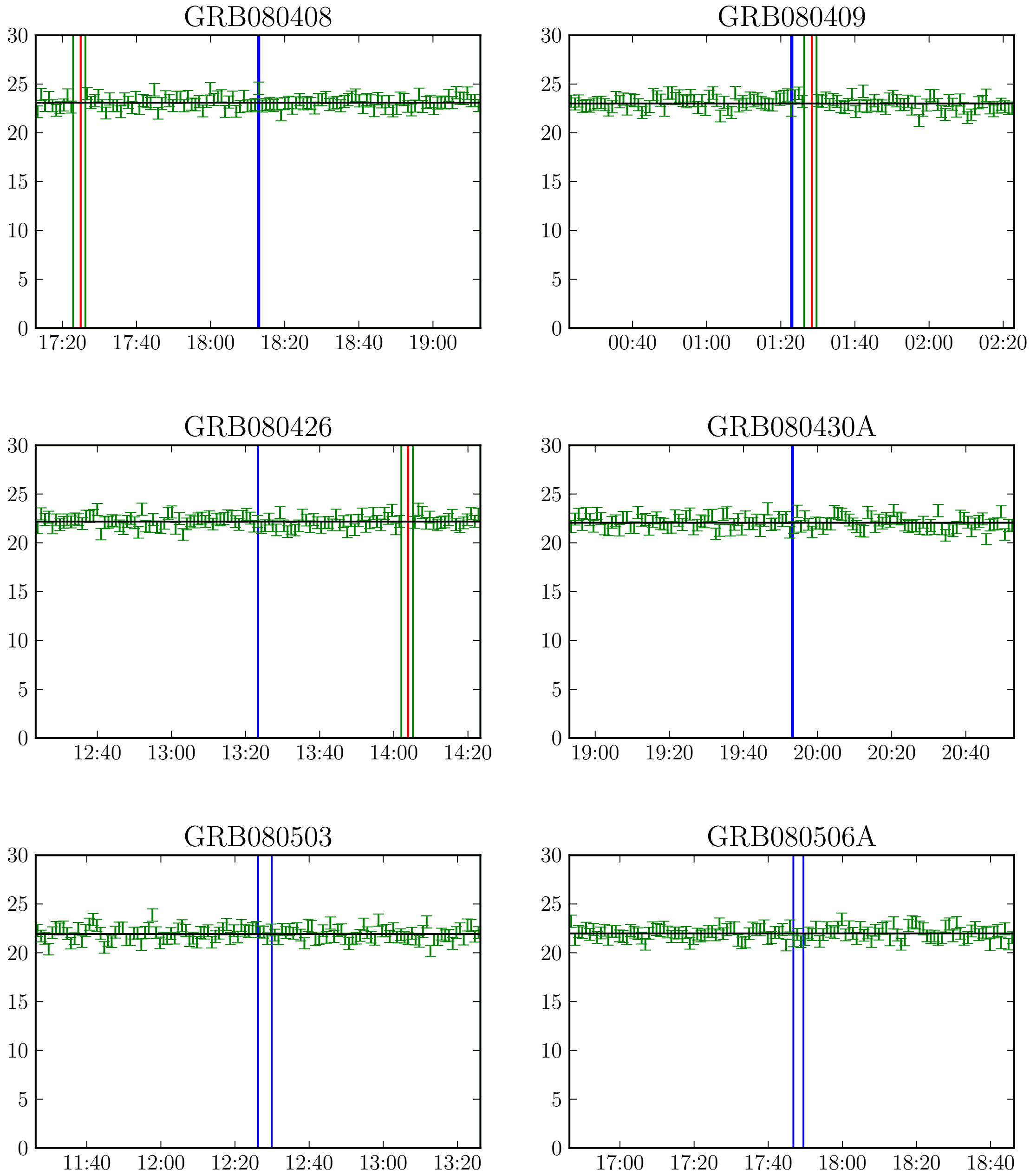

Figure 5.2: The Muon Filter rate vs time for a two hour time window about several example GRBs. The overall rate is calculated by doing a 1 dimensional χ^2 fit to a constant function. These plots were used to find any pathological behavior in the detector on the order of minutes. Vertical blue lines indicate the time bound of the GRB reported in the GCN circular. Vertical green lines indicate the run boundary as reported by the first and last event of the run, while red lines represent the DAQ transition from one run to another.

time with a rate r, then the distribution of Δt should be the Poissonian probability of discovering one event with rate r:

$$p_{\text{poisson}}(1; r) = re^{-r\Delta t} \tag{5.1}$$

Any detector outages would show up as a significant outlier. Using this technique no significant gaps in data were discovered. Examples of Δt histograms are shown in figure 5.3.

5.2 Burst Parameters

After removing the bursts where IceCube was not operating properly, there remained a total of 117 bursts. Table 5.1 shows the complete catalog containing all information taken from GCN circulars. The catalog was assembled by considering all GCN circulars and reports for each GRB.

The start time and stop time, T_1 and T_2 respectively, are relative to the nominal trigger time T_0. These values are the earliest and latest time that any satellite performed a spectral fit to data or reported observing gamma-rays. If more than one satellite observed gamma-rays, T_1 and T_2 may have come from different satellites. Values of T_1 and T_2 were verified by examining the light curves produced by the satellites, see figure 5.4.

GCN circulars report GRB trigger times in Universal Time (UT), while IceCube measures event times in Coordinated Universal Time (UTC). Although the maximum discrepancy between these two time systems is < 0.9 s, several bursts in

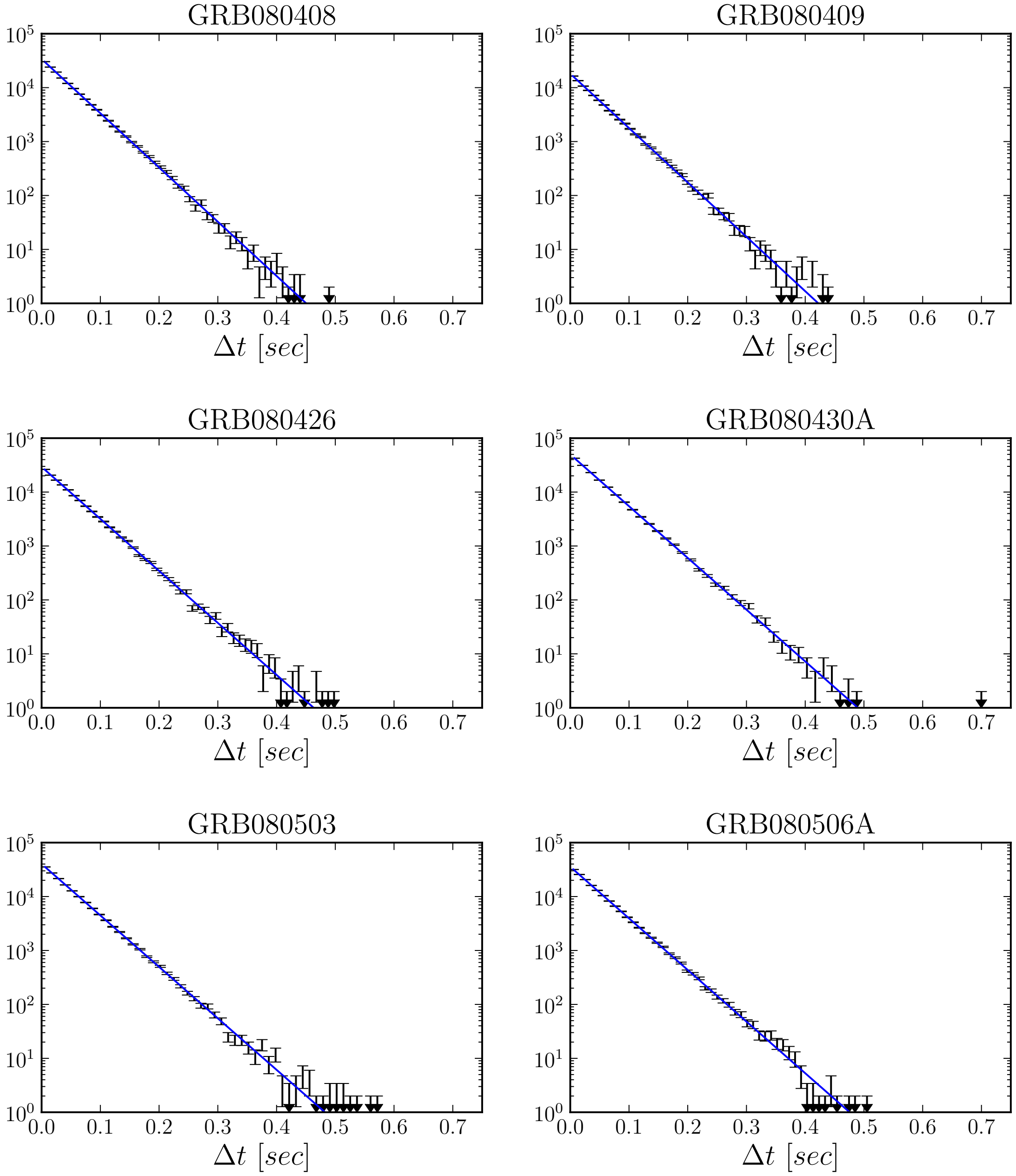

Figure 5.3: The time difference between two events, Δt, are plotted for six GRBs. The distribution of Δt should be a negative exponential (Poisson probability of one event). The histogram is fit to a exponential.

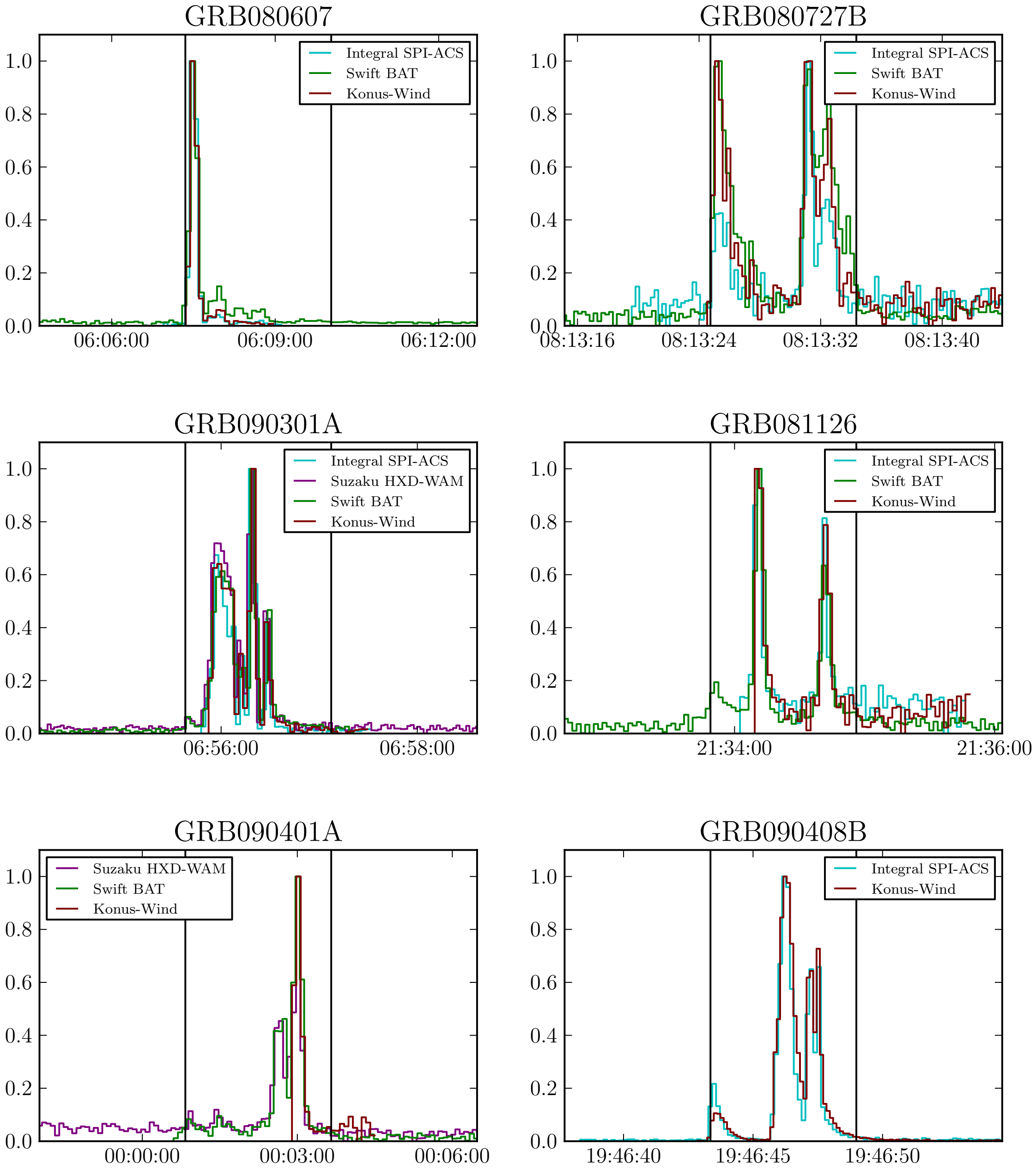

Figure 5.4: Example of light curves from GRBs. Vertical axis is arbitrary and scaled independently for each satellite. T_1 and T_2 are shown as vertical black lines. Light curves were obtained from satellites' respective web pages[250].

the sample have durations lasting less than this and require time correction. Times reported by INTEGRAL and Konus-Wind were corrected for the gamma-ray's time of flight from the detector to the Earth using the positions of the GRB and the satellite[251].

The Right Ascension (RA), Declination (Dec) and positional uncertainty σ_{GRB} come from whichever circular reported the lowest positional uncertainty except for bursts localized by the GBM in which case the *Fermi* GBM burst catalog[252] was used. Positional uncertainties reported as 90% confidence intervals are scaled to 68% confidence intervals assuming a two dimensional Gaussian PDF. For bursts where IPN localization gave the best position, the positional uncertainty was determined as one third of the distance to the farthest corner of the reported 3σ error box.

GRBs can be divided into several different categories, Short-Hard Bursts (SHB) and Long-Soft Bursts (LSB) are the main division. SHBs typically have short durations, a harder spectrum, and little to no spectral lag, while long bursts have a long duration, softer spectrum, and long spectral lag. The long group is further broken down into x-ray flashes(XRF), x-ray rich bursts (XRR), and regular GRBs (referred to as LSB), where XRF are weaker bursts with softer spectra, while XRR represent an intermediate class between XRF and LSB. Although the mechanism which creates the prompt emission in different classes is believed to be the same, the energetics which effect neutrino production can be significantly different. Therefore, it is necessary to treat the classes differently in assigning parameters.

A burst was assigned to a category if it was identified as such in a GCN circular or report. GRB080515 was the only burst identified as an XRF[253]. Despite their short duration, GRB080426[254] and GRB081228[255] were identified as long based on their spectral lag and soft spectra. Many GRBs were identified as short based on their hard spectrum and low spectral lag including GRB080503[256], GRB081024A[257], GRB081209[258], GRB081211B[259], GRB081216[260], GRB090227B[261], and GRB090426[262]. Bursts with $T_{90} < 2$ sec which were not identified as either type were classified as SHBs. These include GRB080702, GRB081024B, GRB081102B, GRB081105B, GRB081119, GRB081204B, GRB081223, GRB081229A, GRB090108A, GRB090206A, GRB090219, GRB090328B, where T_{90} is the time interval over which 90% of the GRBs fluence occurs. All other bursts were classified as LSB.

If spectral parameters are available from more than one satellite, the parameters were taken preferentially using the following order: *Fermi* GBM, Konus-Wind, Suzaku WAM, and finally *Swift*. Since the theory discussed in section 2.6 is based on broken power-laws, but the spectral fits reported by satellites are reported as either simple power-laws, power-laws with an exponential cutoff, or a Band function, the parameters are adjusted to broken power-law parameters. For bursts where spectral information was not available and bursts where the best fit was a power-law or power-law with exponential cutoff which do not contain all spectral information needed, average values from the BATSE catalog[54, 263] were used. Although this analysis used a sample of GRBs from many different detectors, each with their own systematic biases, it was decided to use the BATSE catalog to determine average parameters. The BATSE catalog is the largest GRB catalog and covers a very wide energy range and is widely used in the literature for neutrino emission. The sample of GBM bursts, which constitutes the majority of bursts in this analysis, should be similar to the BATSE catalog. A discussion on the validity of using average parameters can be found in [264]. For bursts with simple power-laws fits, α_γ was set to the measured power-law, ϵ_γ is assumed to be 200 keV for LSB and 1000 keV for SHB with $\beta_\gamma = \alpha_\gamma + 1$. For bursts with an exponential cutoff, ϵ_{cutoff} is used for ϵ_γ, and β_γ is assumed to be $\alpha_\gamma + 1$. The broken power-law which best represents a Band function has $\epsilon_\gamma = \epsilon_{band}(\alpha_\gamma - \beta_\gamma)/(2 + \alpha_\gamma)/e$[265] where e is Euler's number. The normalization of the gamma spectrum is found by setting the fluence of the broken power-law equal to the fluence in the observed energy band. The one XRF in the sample was fit to a Band function and did not require the use of average parameters for the spectrum. For the four bursts with no fluence measurement the fluence normalization was set to $f_\gamma(1MeV) = 7.41\mathrm{MeV}^{-1}\ \mathrm{cm}^{-2}$ which is equivalent to a fluence of $\mathcal{F}_\gamma = 5.8 \times 10^{-5}$ erg cm^{-2}.

For bursts with redshift measurements, the value from whichever circular claimed the smallest uncertainty on the redshift was used. Average values are used for bursts with no measurements. Since only a few BATSE bursts had observed redshifts, the BATSE catalog could not be used to determine average values for redshift. For LSB and XRF, the average value of $z = 2.15$ was taken from a catalog of 77 *Swift* bursts[266]. At the time these parameters were chosen, there had only been 19 SHBs with measured redshift. The average of these was used for SHB $z = 0.50$.

The neutrino flux is dependent on the density of photons at the source which was expressed in the model derived in section 2.6 as L_{iso}, the isotropic luminosity. For bursts with a redshift measurement, the isotropic luminosity in the GRB's reference frame is calculated as

$$L_{iso} = \frac{4\pi D_L^2 \mathcal{F}_\gamma}{T_{90}(1+z)} \tag{5.2}$$

where D_L is the cosmological luminosity distance, which can be calculated from the burst's redshift, z, using the standard model of cosmology[267, 268]:

$$D_L(z) = \frac{c}{h_0}(1+z)\int_0^z \frac{\mathrm{d}z'}{\sqrt{\Omega_m(1+z')^3+\Omega_\Lambda}} \tag{5.3}$$

This equation assumes a flat universe ($\Omega_k = 0$) and neglects radiation. The cosmological parameters are taken from the *Wilkinson Microwave Anisotropy Probe* 7 year data: $h_0 = 70.3$km/s/Mpc, $\Omega_\Lambda = 0.729$ and $\Omega_m = 1 - \Omega_\Lambda$[269]. For bursts with no redshift measurement, average values were used. $L_{iso} = 10^{52}$ ergs was used for LSB and $L_{iso} = 10^{51}$ ergs for SHB and XRF.

Since the predicted neutrino flux depends on Γ^4, this is by far the most important parameter. The current state of measurements is reviewed in section 2.4, but only three bursts in this sample have measured Γ. A method for estimating the boost factor from the spectral information has been proposed[156], but if bursts were misaligned this would lead to a misinterpretation of the boost factor. It was decided that it would be safer to use a constant value for all bursts. Since the Lorentz factor is constrained to $100 < \Gamma < 1000$, the geometric mean $\Gamma = 316$ was used as the value for all bursts. The time scale of variation in the central engine's output, t_{var}, is estimated to be 10 ms based on simulation of LSB fireballs[270], while SHB are assumed to vary on a shorter timescale so $t_{var} = 1$ ms is used. There is no theory to determine the equipartition fractions ξ_e and ξ_B but based on typical values of the observed gamma-ray break energy, they cannot be too far below one[89]. Values of 0.1 are typical in the literature[156, 271–273] and are what is used here.

The distribution of the parameters used are shown in figure 5.5. An individual neutrino spectrum was then calculated for each of the 117 bursts in the sample according to section 2.6, the results are shown in figure 5.6.

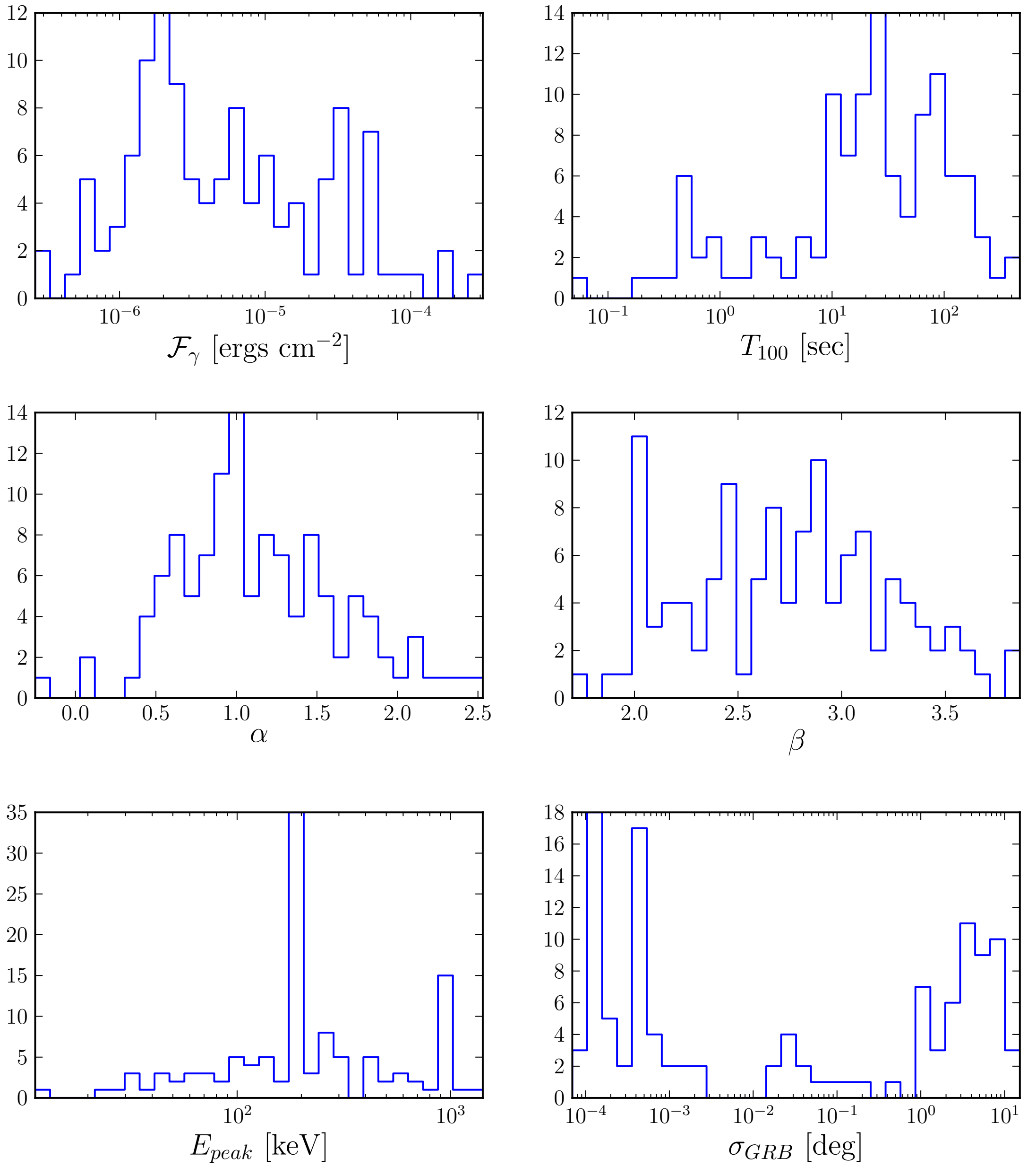

Figure 5.5: The distribution of different burst properties used in this analysis.

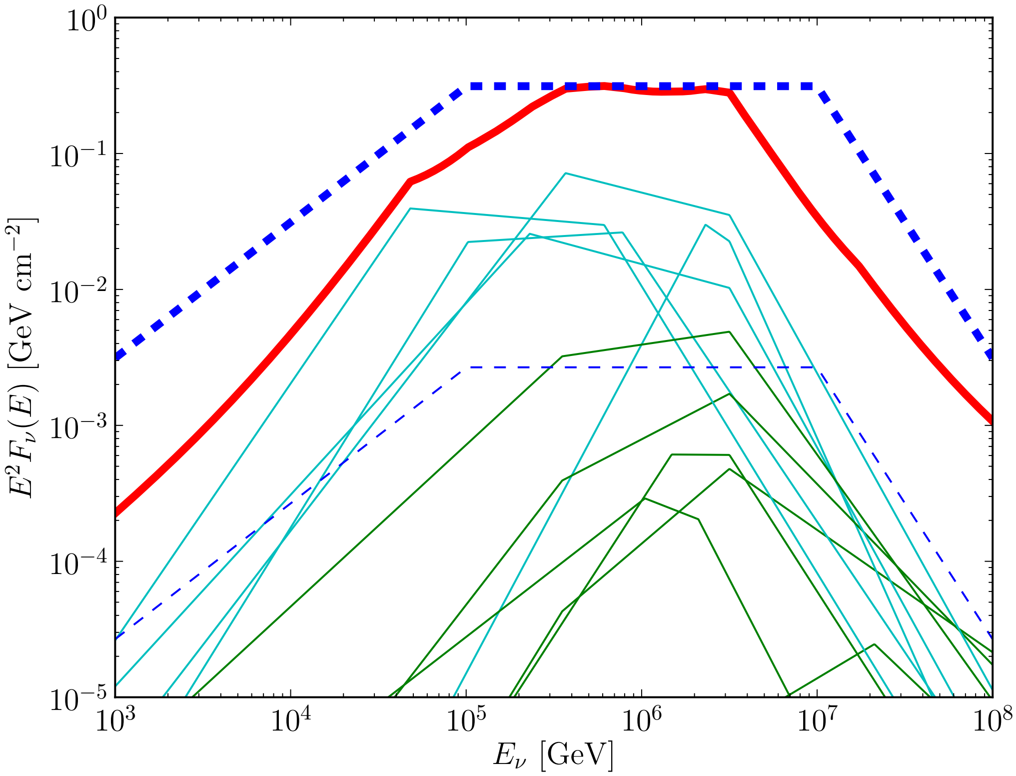

Figure 5.6: The neutrino spectra, including oscillations, of the five brightest GRBs are shown (thin cyan lines) along with eight randomly selected bursts (thin green lines). A single burst with Waxman and Bahcall parameters[274], assuming a cosmic ray energy density of 10^{44} erg Mpc^{-3} yr^{-1}, is shown by a thin dashed blue line. The sum of all 117 individual bursts is shown as a thick solid red line along with the Waxman and Bahcall prediction for 117 bursts in a thick dashed blue line.

Table 5.1: Catalog of GRB parameters as measured by satellites compiled from GCN notices and circulars. GRBs are named after the day they were detected, in year-month-day format, for example GRB080409 occurred on April 9, 2008. For dates with more than one burst, a letter suffix is added. T_0 denotes trigger time in UT. T_1 and T_2 are the start and stop of the gamma emission relative to T_0 in seconds. RA and Dec are the Right Ascension and Declination of the GRB in decimal degrees as measured by the observation with the smallest σ_{GRB}, where σ_{GRB} is the spatial resolution (68% uncertainty) of the GRB location, z is the redshift. f_γ is the gamma-ray fluence at ϵ_γ in $MeV^{-1}cm^{-2}$, ϵ_γ is the spectral break in MeV, and α_γ and β_γ are the spectral indices. f_ν is the neutrino fluence at e_ν^b in $GeV^{-1}cm^{-2}$, ϵ_ν^b and ϵ_ν^s are breaks in the neutrino spectrum in TeV, and α_ν, β_ν and γ_ν are the neutrino spectral indices. † denotes that the value was not measured and an average value was substituted.

Name	T_0 (UT)	T_1	T_2	RA	Dec	σ_{GRB}	z	f_γ	ϵ_γ	α_γ	β_γ	f_ν	ϵ_ν^b	ϵ_ν^s	α_ν	β_ν	γ_ν
080408	18:12:48	0.0	20.0	114.7	33.3	$0.4''$	2.15†	1.85e+02†	0.20†	1.0†	2.0†	6.68e-14	0.35	3.17	1.0	2.0	4.0
080409	01:22:57	-12.5	11.0	84.3	5.1	$1.4''$	2.15†	3.58e+00	0.20†	2.1	3.1†	3.45e-16	0.35	3.17	-0.1	0.9	2.9
080426	13:23:22	1.0	3.2	26.5	69.5	$1.3''$	2.15†	4.78e+01	0.05	1.8	3.8†	1.05e-16	1.28	3.17	-0.8	1.2	3.2
080430A	19:53:02	-0.2	21.4	165.3	51.7	$0.4''$	0.77	1.18e+01	0.20†	1.7	2.7†	5.70e-18	1.12	24.44	0.3	1.3	3.3
080503	12:26:13	0.6	221.0	286.6	68.8	$0.2''$	0.50†	5.43e−01	1.00†	2.0	3.0†	8.45e-16	0.31	2.10	0.0	1.0	3.0
080506A	17:46:21	26.0	189.0	329.4	39.0	$0.4''$	2.15†	1.06e+01	0.20†	1.9	2.9†	1.08e-15	0.35	3.17	0.1	1.1	3.1
080507	07:45:00	0.0	49.0	233.7	56.4	$0.5''$	2.15†	1.04e+02	0.42	0.9	2.9†	2.02e-13	0.17	3.17	0.1	2.1	4.1
080513	05:14:32	-21.1	11.1	163.3	28.2	$11.0'$	2.15†	1.25e+02	0.22	1.5	3.5†	1.86e-14	0.32	3.17	-0.5	1.5	3.5
080514B	09:55:56	0.0	13.2	322.8	0.7	$0.4''$	2.15†	6.88e+02	0.11	0.6	2.5	2.77e-14	0.64	3.17	0.5	2.4	4.4
080515	06:01:13	-1.8	24.8	3.2	32.6	$2.7''$	3.20	1.59e+03	0.03	0.9	2.9†	7.96e-16	1.59	1.99	0.1	2.1	4.1
080517	21:22:51	0.1	69.3	102.2	50.7	$1.3''$	2.15†	7.03e+00	0.20†	1.5	2.5†	9.71e-16	0.35	3.17	0.5	1.5	3.5
080524	04:13:00	-2.0	8.0	268.4	80.1	$1.8'$	2.15†	6.04e+00	0.20†	1.1	2.1†	1.77e-15	0.35	3.17	0.9	1.9	3.9
080603A	11:18:11	0.0	180.0	279.4	62.7	$0.2''$	1.69	1.74e+02	0.20†	1.0†	2.0†	2.35e-14	0.48	4.78	1.0	2.0	4.0
080603B	19:38:13	0.2	75.6	176.5	68.1	$0.2''$	2.69	1.60e+02	0.10	1.2	3.2†	3.20e-15	0.50	3.57	-0.2	1.8	3.8
080604	07:27:01	-27.1	67.3	237.0	20.6	$0.4''$	1.42	7.37e+00	0.20†	1.8	2.8†	4.44e-18	0.60	23.04	0.2	1.2	3.2
080605	23:47:57	-4.7	30.9	262.1	4.0	$0.4''$	1.64	1.65e+02	0.25	1.0	3.0†	5.53e-14	0.40	2.16	-0.0	2.0	4.0
080607	06:07:27	-5.9	154.7	194.9	15.9	$0.4''$	3.04	1.70e+02	0.42	1.1	3.1†	2.13e-12	0.10	0.78	-0.1	1.9	3.9
080613A	09:35:21	0.0	30.0	213.3	5.2	$0.4''$	2.15†	2.26e+01	0.20†	1.0†	2.0†	8.13e-15	0.35	3.17	1.0	2.0	4.0
080625	12:28:31	-5.0	80.0	298.4	56.3	$0.4''$	2.15†	3.42e+00	0.50	1.7	3.7†	3.59e-15	0.14	3.17	-0.7	1.3	3.3

Table 5.1: GRB Catalog (continued)

Name	T_0 (UT)	T_1	T_2	RA	Dec	σ_{GRB}	z	f_γ	ϵ_γ	α_γ	β_γ	f_ν	ϵ_ν^b	ϵ_ν^s	α_ν	β_ν	γ_ν
080701A	10:13:37	-2.1	25.2	45.8	75.5	$1.2''$	$2.15^\dagger$	3.42e+00	$0.20^\dagger$	2.2	$3.2^\dagger$	3.33e-16	0.35	3.17	-0.2	0.8	2.8
080702A	11:50:43	0.7	1.2	313.1	72.3	$1.3''$	$0.50^\dagger$	6.65e−02	$1.00^\dagger$	1.3	$2.3^\dagger$	1.16e-16	0.31	2.10	0.7	1.7	3.7
080707	08:27:53	-1.1	27.3	32.6	33.1	$0.8''$	1.23	4.86e+00	$0.20^\dagger$	1.8	$2.8^\dagger$	3.61e-18	0.70	21.21	0.2	1.2	3.2
080710	07:13:10	-96.1	44.1	8.3	19.5	$0.4''$	0.84	1.92e+01	$0.20^\dagger$	1.5	$2.5^\dagger$	3.00e-18	1.03	47.66	0.5	1.5	3.5
080726	01:26:10	0.0	12.0	20.4	13.9	$3.5'$	$2.15^\dagger$	$1.85\text{e+}02^\dagger$	$0.20^\dagger$	$1.0^\dagger$	$2.0^\dagger$	6.68e-14	0.35	3.17	1.0	2.0	4.0
080727B	08:13:24	0.8	10.3	276.9	1.2	$1.3''$	$2.15^\dagger$	4.17e+01	0.28	0.8	$2.9^\dagger$	2.44e-14	0.25	3.17	0.1	2.1	4.2
080727C	23:07:35	-2.9	116.7	32.6	64.1	$1.1''$	$2.15^\dagger$	1.84e+02	0.14	0.9	$2.9^\dagger$	1.21e-14	0.49	3.17	0.1	2.1	4.1
080810	13:10:12	-20.9	111.7	356.8	0.3	$0.4''$	3.35	5.85e+01	0.31	0.9	$2.9^\dagger$	2.26e-13	0.12	1.70	0.1	2.1	4.1
080816A	12:04:18	-1.0	69.0	156.2	42.6	2.0°	$2.15^\dagger$	4.95e+02	0.15	0.6	$2.6^\dagger$	4.91e-14	0.48	3.17	0.4	2.4	4.4
080818B	22:40:49	-1.3	10.0	98.1	7.4	7.3°	$2.15^\dagger$	9.46e+01	0.08	1.3	$3.3^\dagger$	6.83e-16	0.88	3.17	-0.3	1.7	3.7
080822B	21:02:52	1.0	65.0	63.6	25.8	$2.5'$	$2.15^\dagger$	5.06e−01	$0.20^\dagger$	2.5	$3.5^\dagger$	5.17e-17	0.35	3.17	-0.5	0.5	2.5
080830	08:50:16	-3.0	28.0	160.1	30.8	2.5°	$2.15^\dagger$	4.42e+01	0.28	0.9	$2.9^\dagger$	2.43e-14	0.25	3.17	0.1	2.1	4.1
080903	01:12:23	-10.2	68.3	86.8	51.3	$1.1''$	$2.15^\dagger$	1.83e+02	0.06	0.8	$2.8^\dagger$	6.37e-16	1.17	3.17	0.2	2.2	4.2
080916B	14:44:47	-3.0	36.0	163.7	69.1	$3.6''$	$2.15^\dagger$	8.41e+00	$0.20^\dagger$	1.5	$2.5^\dagger$	1.24e-15	0.35	3.17	0.5	1.5	3.5
080920	06:25:48	-6.0	79.0	121.6	8.9	5.4°	$2.15^\dagger$	3.19e+01	0.16	1.4	$3.4^\dagger$	1.95e-15	0.43	3.17	-0.4	1.6	3.6
080925	18:35:55	-8.1	21.9	96.1	18.2	1.2°	$2.15^\dagger$	1.55e+03	0.05	0.5	2.3	5.65e-15	1.36	3.17	0.7	2.5	4.5
080927	11:30:32	-1.3	20.2	61.3	27.4	4.6°	$2.15^\dagger$	3.25e+03	0.01	0.7	1.7	5.94e-16	3.17	6.22	1.3	3.3	5.3
081003A	13:46:12	-12.0	18.0	262.4	16.6	$2.8''$	$2.15^\dagger$	6.94e+00	$0.20^\dagger$	$1.0^\dagger$	$2.0^\dagger$	2.50e-15	0.35	3.17	1.0	2.0	4.0
081003B	20:48:08	0.0	30.0	285.0	16.7	$1.1'$	$2.15^\dagger$	1.04e+02	$0.20^\dagger$	1.0	$2.0^\dagger$	3.75e-14	0.35	3.17	1.0	2.0	4.0
081003C	15:27:17	-4.0	51.0	259.1	35.4	6.9°	$2.15^\dagger$	3.39e+01	$0.30^\dagger$	1.4	$2.4^\dagger$	1.77e-14	0.23	3.17	0.6	1.6	3.6
081009	03:20:58	-0.1	49.3	250.5	18.4	1.0°	$2.15^\dagger$	1.99e+04	0.03	0.1	3.4	5.61e-15	2.31	3.17	-0.4	2.9	4.9
081011	00:28:50	-0.4	9.5	220.3	33.5	$0.4''$	$2.15^\dagger$	2.19e+00	$0.20^\dagger$	1.5	$2.5^\dagger$	3.33e-16	0.35	3.17	0.5	1.5	3.5
081022	14:23:48	-8.5	208.1	226.6	12.4	$1.0'$	$2.15^\dagger$	2.66e+01	$0.20^\dagger$	1.7	$2.7^\dagger$	3.16e-15	0.35	3.17	0.3	1.3	3.3
081024A	05:53:08	-0.8	1.2	27.9	61.3	$1.3''$	$0.50^\dagger$	3.00e−01	$1.00^\dagger$	1.2	$2.2^\dagger$	5.86e-16	0.31	2.10	0.8	1.8	3.8
081024B	21:22:41	-0.5	0.0	322.9	21.2	$9.6'$	$0.50^\dagger$	1.55e−01	$1.00^\dagger$	1.2	$2.2^\dagger$	3.00e-16	0.31	2.10	0.8	1.8	3.8
081025	08:22:02	61.8	90.1	245.4	60.5	$4.7''$	$2.15^\dagger$	4.14e+01	0.25	0.3	$2.4^\dagger$	3.21e-14	0.28	3.17	0.6	2.6	4.7

Table 5.1: GRB Catalog (continued)

Name	T_0 (UT)	T_1	T_2	RA	Dec	σ_{GRB}	z	f_γ	ϵ_γ	α_γ	β_γ	f_ν	ϵ_ν^b	ϵ_ν^s	α_ν	β_ν	γ_ν
081028A	00:25:00	30.1	442.3	121.9	2.3	$1.1''$	3.04	4.89e+02	0.06	1.2	$3.2^\dagger$	9.31e-16	0.74	5.89	-0.2	1.8	3.8
081102A	17:44:39	-19.7	63.3	331.2	53.0	$1.1''$	$2.15^\dagger$	1.09e+03	0.03	0.4	2.4	6.81e-16	2.16	3.17	0.6	2.6	4.6
081102B	08:45:00	0.3	1.3	225.3	22.0	8.6°	$2.15^\dagger$	6.58e−01	1.00	1.1	$3.1^\dagger$	1.16e-14	0.07	3.17	-0.1	1.9	3.9
081105B	14:43:51	0.2	0.3	215.8	38.7	11.4°	$0.50^\dagger$	1.20e−01	$1.00^\dagger$	1.2	$2.2^\dagger$	2.51e-16	0.31	2.10	0.8	1.8	3.8
081107	07:42:01	-0.1	1.8	51.0	17.1	3.5°	$2.15^\dagger$	6.12e+02	0.03	-0.2	2.8	2.73e-16	2.17	3.17	0.2	3.2	5.2
081110	14:25:43	0.0	20.0	111.7	21.4	1.8°	$2.15^\dagger$	$1.85\text{e+}02^\dagger$	$0.20^\dagger$	$1.0^\dagger$	$2.0^\dagger$	6.68e-14	0.35	3.17	1.0	2.0	4.0
081119	04:25:27	-0.4	0.1	346.5	30.0	15.2°	$0.50^\dagger$	1.86e−01	$1.00^\dagger$	1.3	$2.3^\dagger$	3.38e-16	0.31	2.10	0.7	1.7	3.7
081122A	12:28:12	-0.8	26.2	339.1	40.0	1.0°	$2.15^\dagger$	8.66e+01	0.20	0.8	$2.8^\dagger$	1.90e-14	0.35	3.17	0.2	2.2	4.2
081126	21:34:10	-21.1	46.2	323.5	48.7	$0.4''$	$2.15^\dagger$	3.53e+01	0.32	0.8	$2.8^\dagger$	3.02e-14	0.22	3.17	0.2	2.2	4.2
081127	07:05:08	-30.3	9.7	332.1	6.9	$1.2''$	$2.15^\dagger$	2.87e+00	$0.20^\dagger$	2.1	$3.1^\dagger$	2.77e-16	0.35	3.17	-0.1	0.9	2.9
081128	17:18:44	-68.3	63.4	20.8	38.1	$1.3''$	$2.15^\dagger$	5.18e+02	0.05	1.1	$3.1^\dagger$	6.02e-16	1.56	3.17	-0.1	1.9	3.9
081203A	13:57:11	-68.3	405.7	233.0	63.5	$0.4''$	$2.15^\dagger$	2.85e+01	0.58	1.3	$3.3^\dagger$	7.06e-14	0.12	3.17	-0.3	1.7	3.7
081203B	13:52:02	-33.1	50.4	228.8	44.4	$0.4''$	$2.15^\dagger$	2.91e+02	0.26	1.2	$3.2^\dagger$	8.61e-14	0.28	3.17	-0.2	1.8	3.8
081204B	12:24:26	-0.3	-0.1	150.8	30.5	10.2°	$0.50^\dagger$	2.55e−01	$1.00^\dagger$	1.2	$2.2^\dagger$	5.26e-16	0.31	2.10	0.8	1.8	3.8
081206A	06:35:53	-6.1	15.4	120.1	32.8	6.4°	$2.15^\dagger$	3.69e+01	0.18	0.1	$2.1^\dagger$	1.38e-14	0.39	3.17	0.9	2.9	4.9
081207	16:18:47	9.1	66.5	112.4	70.5	1.2°	$2.15^\dagger$	4.22e+02	0.31	0.7	2.4	4.86e-13	0.23	3.17	0.6	2.4	4.3
081209	23:31:56	0.3	0.7	45.3	63.5	4.9°	$0.50^\dagger$	2.22e+00	0.30	0.5	2.0	2.66e-16	1.05	2.10	1.0	2.5	4.5
081211B	06:15:02	0.0	102.0	168.3	53.8	$1.4''$	$0.50^\dagger$	3.71e−01	$1.00^\dagger$	1.7	$2.7^\dagger$	5.17e-16	0.31	2.10	0.3	1.3	3.3
081215A	18:48:37	-1.9	13.4	125.6	54.0	1.0°	$2.15^\dagger$	6.00e+01	0.12	0.6	2.1	4.70e-15	0.60	3.17	0.9	2.4	4.4
081216	12:44:00	-0.1	0.8	129.2	7.6	4.4°	$0.50^\dagger$	6.11e+00	0.51	0.7	2.2	2.75e-15	0.60	2.10	0.8	2.3	4.3
081217	23:34:49	0.0	18.4	116.8	26.8	2.0°	$2.15^\dagger$	3.95e+02	0.09	0.6	2.7	7.19e-15	0.76	3.17	0.3	2.4	4.4
081223	10:03:57	0.1	0.6	112.5	33.2	3.8°	$0.50^\dagger$	5.98e+00	0.28	0.6	$2.6^\dagger$	3.72e-16	1.11	2.10	0.4	2.4	4.4
081224	21:17:55	0.0	20.0	201.7	75.1	1.0°	$2.15^\dagger$	6.94e+00	0.45	0.8	$2.8^\dagger$	1.70e-14	0.16	3.17	0.2	2.2	4.2
081226C	03:44:52	-3.2	11.1	193.0	26.8	2.4°	$2.15^\dagger$	1.18e+02	0.08	1.0	$3.0^\dagger$	1.06e-15	0.86	3.17	-0.0	2.0	4.0
081228	01:17:40	0.7	3.6	39.5	30.9	$2.0''$	$2.15^\dagger$	5.22e−01	$0.20^\dagger$	2.1	$3.1^\dagger$	5.03e-17	0.35	3.17	-0.1	0.9	2.9
081229	04:29:02	-0.2	0.1	172.6	56.9	8.8°	$0.50^\dagger$	9.97e−01	0.81	0.4	$2.4^\dagger$	1.50e-15	0.38	2.10	0.6	2.6	4.6

Table 5.1: GRB Catalog (continued)

Name	T_0 (UT)	T_1	T_2	RA	Dec	σ_{GRB}	z	f_γ	ϵ_γ	α_γ	β_γ	f_ν	ϵ_ν^b	ϵ_ν^s	α_ν	β_ν	γ_ν
090102	02:55:45	-13.0	20.2	128.2	33.1	$0.8''$	1.55	5.61e+01	0.45	0.9	$2.9^\dagger$	1.09e-13	0.24	2.69	0.1	2.1	4.1
090107A	04:48:04	0.5	13.2	302.4	4.7	$1.7'$	$2.15^\dagger$	2.39e+00	$0.20^\dagger$	1.7	$2.7^\dagger$	2.78e-16	0.35	3.17	0.3	1.3	3.3
090107B	16:20:36	-2.0	27.3	284.8	59.6	$1.3''$	$2.15^\dagger$	5.16e+01	0.11	0.7	$2.7^\dagger$	1.50e-15	0.66	3.17	0.3	2.3	4.3
090108A	00:29:02	0.2	1.1	260.8	46.0	3.8°	$0.50^\dagger$	1.39e+02	0.04	0.5	2.0	2.04e-16	2.10	8.22	1.0	3.0	5.0
090109	07:58:30	-3.3	0.8	129.6	51.8	9.8°	$2.15^\dagger$	4.15e−01	1.00	1.5	$3.5^\dagger$	3.33e-15	0.07	3.17	-0.5	1.5	3.5
090111	23:58:21	-2.2	26.3	251.7	0.1	$1.2''$	$2.15^\dagger$	2.40e+00	$0.20^\dagger$	2.4	$3.4^\dagger$	2.40e-16	0.35	3.17	-0.4	0.6	2.6
090112B	17:30:15	0.0	11.0	192.3	25.4	1.7°	$2.15^\dagger$	3.06e+02	0.07	0.8	2.4	2.33e-15	1.03	3.17	0.6	2.2	4.2
090113	18:40:39	-0.7	10.2	32.1	33.4	$1.2''$	$2.15^\dagger$	8.85e+00	$0.20^\dagger$	1.6	$2.6^\dagger$	1.13e-15	0.35	3.17	0.4	1.4	3.4
090118	13:54:02	66.0	85.0	49.8	18.4	$5.0''$	$2.15^\dagger$	6.31e+00	$0.20^\dagger$	1.4	$2.4^\dagger$	1.16e-15	0.35	3.17	0.6	1.6	3.6
090126A	02:01:15	0.0	60.0	3.7	81.4	$1.6''$	$2.15^\dagger$	$1.85\text{e+}02^\dagger$	$0.20^\dagger$	$1.0^\dagger$	$2.0^\dagger$	6.68e-14	0.35	3.17	1.0	2.0	4.0
090126B	05:26:22	-4.4	5.9	189.2	34.1	3.6°	$2.15^\dagger$	1.94e+02	0.05	1.0	$3.0^\dagger$	2.78e-16	1.48	3.17	0.0	2.0	4.0
090131	02:09:21	-1.8	49.2	352.3	21.2	1.0°	$2.15^\dagger$	5.21e+03	0.03	1.3	2.3	2.38e-15	2.42	3.17	0.7	1.7	3.7
090206	14:52:42	0.1	0.7	156.2	8.8	8.7°	$0.50^\dagger$	1.23e+00	0.71	0.7	$2.6^\dagger$	1.07e-15	0.44	2.10	0.4	2.4	4.3
090207	18:39:10	-1.2	16.2	252.7	34.9	3.8°	$2.15^\dagger$	1.19e+00	1.00	1.6	$3.6^\dagger$	8.19e-15	0.07	3.17	-0.6	1.4	3.4
090219	01:46:18	-0.0	0.6	26.5	59.2	5.2°	$0.50^\dagger$	3.04e−01	$1.00^\dagger$	1.4	$2.4^\dagger$	4.92e-16	0.31	2.10	0.6	1.6	3.6
090222	04:17:09	-2.1	15.3	118.6	45.0	4.3°	$2.15^\dagger$	3.07e+01	0.16	1.0	$3.0^\dagger$	2.43e-15	0.45	3.17	0.0	2.0	4.0
090227B	18:31:01	0.3	0.8	11.8	32.2	1.8°	$0.50^\dagger$	6.65e+00	1.42	0.5	3.0	3.80e-14	0.22	2.10	-0.0	2.5	4.5
090228B	23:25:01	-1.4	5.8	357.6	36.7	3.3°	$2.15^\dagger$	1.58e+01	0.15	0.7	$2.7^\dagger$	1.38e-15	0.48	3.17	0.3	2.3	4.3
090301A	06:55:55	-16.9	72.3	338.1	26.6	$0.7'$	$2.15^\dagger$	5.31e+02	0.25	0.9	2.6	2.29e-13	0.28	3.17	0.4	2.1	4.1
090301B	07:33:37	-0.6	4.6	352.8	9.5	5.0°	$2.15^\dagger$	3.85e+00	0.55	1.0	$3.0^\dagger$	1.28e-14	0.13	3.17	-0.0	2.0	4.0
090305B	01:14:35	0.2	3.2	135.0	74.3	5.4°	$2.15^\dagger$	1.16e+01	0.26	0.5	1.9	1.55e-14	0.27	3.17	1.1	2.5	4.5
090306C	05:52:05	-3.7	6.5	137.0	57.0	4.1°	$2.15^\dagger$	2.53e+01	0.11	0.6	$2.6^\dagger$	8.46e-16	0.66	3.17	0.4	2.4	4.4
090313	09:06:27	-20.9	67.0	198.4	8.1	$0.4''$	3.38	1.08e+01	$0.20^\dagger$	1.9	$2.9^\dagger$	1.38e-15	0.18	3.20	0.1	1.1	3.1
090320B	19:13:46	-7.3	52.1	183.4	49.8	9.5°	$2.15^\dagger$	7.30e+01	0.07	1.1	$3.1^\dagger$	4.07e-16	0.98	3.17	-0.1	1.9	3.9
090323	00:02:42	-1.4	154.2	190.7	17.1	$0.4''$	3.57	1.07e+02	0.70	0.9	$2.9^\dagger$	1.71e-11	0.05	0.61	0.1	2.1	4.1
090328B	17:07:04	0.8	1.1	155.7	33.4	7.9°	$0.50^\dagger$	6.26e−01	1.05	0.9	2.5	1.48e-15	0.30	2.10	0.5	2.1	4.1

Table 5.1: GRB Catalog (continued)

Name	T_0 (UT)	T_1	T_2	RA	Dec	σ_{GRB}	z	f_γ	ϵ_γ	α_γ	β_γ	f_ν	ϵ_ν^b	ϵ_ν^s	α_ν	β_ν	γ_ν
090401A	00:00:59	-9.0	160.4	350.9	29.8	$0.7'$	$2.15^\dagger$	1.57e+02	0.22	1.3	$3.3^\dagger$	2.63e-14	0.32	3.17	-0.3	1.7	3.7
090404	15:56:30	-34.8	95.0	239.2	35.5	$1.3''$	$2.15^\dagger$	1.26e+01	$0.20^\dagger$	2.3	$3.3^\dagger$	1.25e-15	0.35	3.17	-0.3	0.7	2.7
090408B	19:46:38	5.4	11.0	44.0	26.6	$29.4'$	$2.15^\dagger$	2.52e+03	0.19	0.7	2.7	5.29e-13	0.37	3.17	0.3	2.3	4.3
090409	06:54:01	0.4	5.5	302.1	1.1	9.6°	$2.15^\dagger$	1.09e+01	0.14	1.2	$3.2^\dagger$	4.64e-16	0.51	3.17	-0.2	1.8	3.8
090410	16:57:52	-58.6	151.4	335.0	15.4	$1.3'$	$2.15^\dagger$	1.06e+02	$0.20^\dagger$	1.2	$2.2^\dagger$	2.60e-14	0.35	3.17	0.8	1.8	3.8
090411B	23:47:44	-7.0	21.8	38.5	5.1	2.4°	$2.15^\dagger$	3.01e+02	0.07	0.8	2.0	4.14e-15	1.01	3.17	1.0	2.2	4.2
090417B	15:20:03	279.0	617.4	209.7	47.0	$3.5''$	$2.15^\dagger$	1.93e+01	$0.20^\dagger$	1.9	$2.9^\dagger$	1.99e-15	0.35	3.17	0.1	1.1	3.1
090418A	11:07:40	-8.3	61.3	269.3	33.4	$0.4''$	1.61	1.70e+01	0.61	1.3	$3.3^\dagger$	1.74e-14	0.17	4.62	-0.3	1.7	3.7
090418B	08:59:02	20.2	145.0	225.9	17.2	$1.3'$	$2.15^\dagger$	6.13e+02	0.12	1.2	$3.2^\dagger$	1.55e-14	0.60	3.17	-0.2	1.8	3.8
090424	14:12:09	-0.8	103.5	189.5	16.8	$0.5''$	0.54	1.28e+03	0.12	0.9	2.9	6.44e-16	2.48	17.10	0.1	2.1	4.1
090425	09:03:30	-0.0	80.6	118.6	68.1	2.1°	$2.15^\dagger$	1.80e+02	0.14	1.6	$3.6^\dagger$	6.92e-15	0.50	3.17	-0.6	1.4	3.4
090426	12:48:47	0.2	1.5	189.1	33.0	$0.5''$	2.61	6.04e−02	$1.00^\dagger$	1.9	$2.9^\dagger$	3.38e-14	0.05	0.16	0.1	1.1	3.1
090428A	10:34:38	-0.1	2.5	210.1	39.5	4.2°	$2.15^\dagger$	3.36e+01	0.10	0.6	$2.6^\dagger$	7.90e-16	0.73	3.17	0.4	2.4	4.4
090428B	13:15:11	-9.1	15.4	0.8	11.5	3.9°	$2.15^\dagger$	3.27e+02	0.07	1.9	$3.9^\dagger$	1.22e-15	1.08	3.17	-0.9	1.1	3.1
090429B	05:30:03	-4.1	2.8	210.7	32.2	$0.4''$	$2.15^\dagger$	7.41e+01	0.04	0.5	$2.5^\dagger$	1.02e-16	1.67	3.17	0.5	2.5	4.5
090429C	12:43:25	-1.3	11.7	260.0	54.3	4.8°	$2.15^\dagger$	1.41e+00	1.00	1.4	$3.4^\dagger$	1.28e-14	0.07	3.17	-0.4	1.6	3.6
090429D	18:03:57	-12.7	1.6	124.4	7.9	5.0°	$2.15^\dagger$	1.18e+01	0.22	0.9	$2.9^\dagger$	3.23e-15	0.32	3.17	0.1	2.1	4.1
090511	16:25:16	-4.7	4.5	161.9	51.3	7.0°	$2.15^\dagger$	4.72e+00	0.39	0.9	$3.0^\dagger$	6.57e-15	0.18	3.17	0.0	2.0	4.0
090518	01:54:44	-2.1	7.6	120.0	0.8	$1.1''$	$2.15^\dagger$	4.76e−01	1.00	1.6	$3.6^\dagger$	3.27e-15	0.07	3.17	-0.6	1.4	3.4
090519	21:08:56	-12.0	60.8	142.3	0.2	$0.4''$	3.85	2.72e+01	$0.20^\dagger$	1.0	$2.0^\dagger$	6.75e-14	0.15	1.48	1.0	2.0	4.0

Chapter 6

Event Selection

IceCube is bombarded with a steady stream of downgoing muons from cosmic ray air showers. These downgoing muons trigger IceCube's multiplicity trigger at a rate of about 1 kHz in the 40 string configuration. In order to use IceCube as a neutrino telescope, a procedure must be developed to reject downgoing muons and accept only upgoing neutrino induced muons. The next most abundant source of events in IceCube is atmospheric muon neutrinos which occur at a rate of about 1 mHz from all directions in the sky. Atmospheric neutrinos are indistinguishable from neutrinos from astrophysical sources (aside from their energy spectrum.) They are considered an irreducible background on the intended signal of astrophysical neutrinos.

Although the muon reconstructions discussed in section 4.4 are highly accurate, a very small fraction of events will be misreconstructed as upgoing. Since the actual upgoing sample of atmospheric neutrinos occur at a rate 10^6 times smaller than the small fraction of misreconstructed downgoing events, misreconstructed downgoing events will still overwhelm the neutrinos. In order to reduce the sample to a pure sample of atmospheric and astrophysical neutrinos, a series of quality cuts are developed to reject misreconstructed events. Processor time and satellite bandwidth from the South Pole must be considered. The basic strategy is to perform a series of reconstructions starting with the simplest, least CPU-intensive reconstructions, and then progressing to more complex, more CPU-intensive reconstructions. Between each level of reconstruction, events that are clearly downgoing based on the previous level of reconstruction will be cut out of the analysis and not reconstructed in subsequent levels.

The result of this analysis will be based on an unbinned likelihood method where a significance is assigned to each individual event. However, before this analysis can be performed it is necessary to remove obvious background so as to constrain the analysis to a sample of events which are mostly neutrinos. The goal of this analysis is discovery, so all decisions and optimizations are made with the goal of increasing the chance of discovery. The procedure for optimizing the quality cuts for discovery on the full unbinned likelihood method is possible but computationally intensive. Instead, quality cuts were optimized with a procedure where the unbinned likelihood method is approximated by a discrete analysis referred to as the binned method. This chapter will describe the optimization of cuts using the binned method.

6.1 Muon Filter

Since there is insufficient bandwidth from the South Pole to transfer all events that trigger IceCube, filters are applied immediately after the DAQ assembles the event. The muon filter looks for upgoing events by running three reconstructions: LineFit which is used as a seed for the other two reconstructions, a single iteration of the SPE fit, and the half sphere reconstruction. In order for an event to pass the muon filter it must contain 10 hit DOMs after time window hit cleaning (see section 4.4.1) and both the single SPE fit and the hemispherical SPE fit must reconstruct with a zenith angle of $\theta_{SPE32,Zenith} \geq 80°$. This results in a stream of events occurring at about 22 Hz, which satisfies the satellite bandwidth constraints. Other filters exist for finding other classes of events including cascade events, downgoing contained, extremely high energy events, IceTop events, and low energy events. These filters were not used in this analysis and will not be discussed further.

6.2 Off-line processing

The data is sent via satellite to University of Wisconsin's data warehouse. From there every event that passed the Online Muon Filter is then reconstructed with a 32 iteration SPE fit. Based on this reconstruction, another quality cut called the good upgoing track cut, is applied. This cut keeps events which reconstruct with a $\theta_{SPE32,Zenith} \geq 80°$ and with $rlogl < 12$, where $rlogl$ is the reduced log-likelihood, the value of the minimum log-likelihood divided by the number of degrees of freedom. The number of degrees of freedom is the number of DOMs used in the reconstruction minus the number of reconstructed parameters. Events that are well reconstructed should be at the bottom of a deep valley in the likelihood space and hence have a smaller $rlogl$, while events that reconstruct poorly often contain a shallow minimum and have a larger $rlogl$. A comparison of data and simulation which pass this criteria is shown in figures 6.1 and 6.2, these cuts are still very far from neutrino level so no comparison to neutrino simulation is made.

If an event passes the cuts described above further reconstructions are performed: the Bayesian weighted zenith reconstruction discussed in section 4.4.6 for further discrimination between upgoing and downgoing tracks, the MPE reconstruction from section 4.4.4 for increased angular resolution, the paraboloid fit from section 4.4.5 for direction uncertainty estimation, and finally Photorec dE/dX from section 4.4.7 for energy estimation.

6.3 Final Cuts

The good upgoing track cuts reduces the background to a rate of about 2.5 Hz. Strong cuts are still needed in order to reduce the data set to a sample on the order of atmospheric neutrinos. The following four variables were found to be the best cut variables for separating signal from background:

N_{dir} The number of DOMs with direct hits, where a direct hit is defined as a hit with $-15\text{ns} > t_{res} > 75\text{ns}$, where t_{res} is the residual time defined in section 4.4.3. A large fraction of hits from a well reconstructed events are expected to be within this threshold, while an event where the reconstructed direction is in a different direction than the true track will have very few direct hits.

L_{dir} The length of direct hits, using the same definition of direct hit, L_{dir} is the length along the reconstructed track from the point where the first direct hit was emitted to the point where the last direct hit was emitted. A well reconstructed track is expected to have direct hits evenly spaced along the

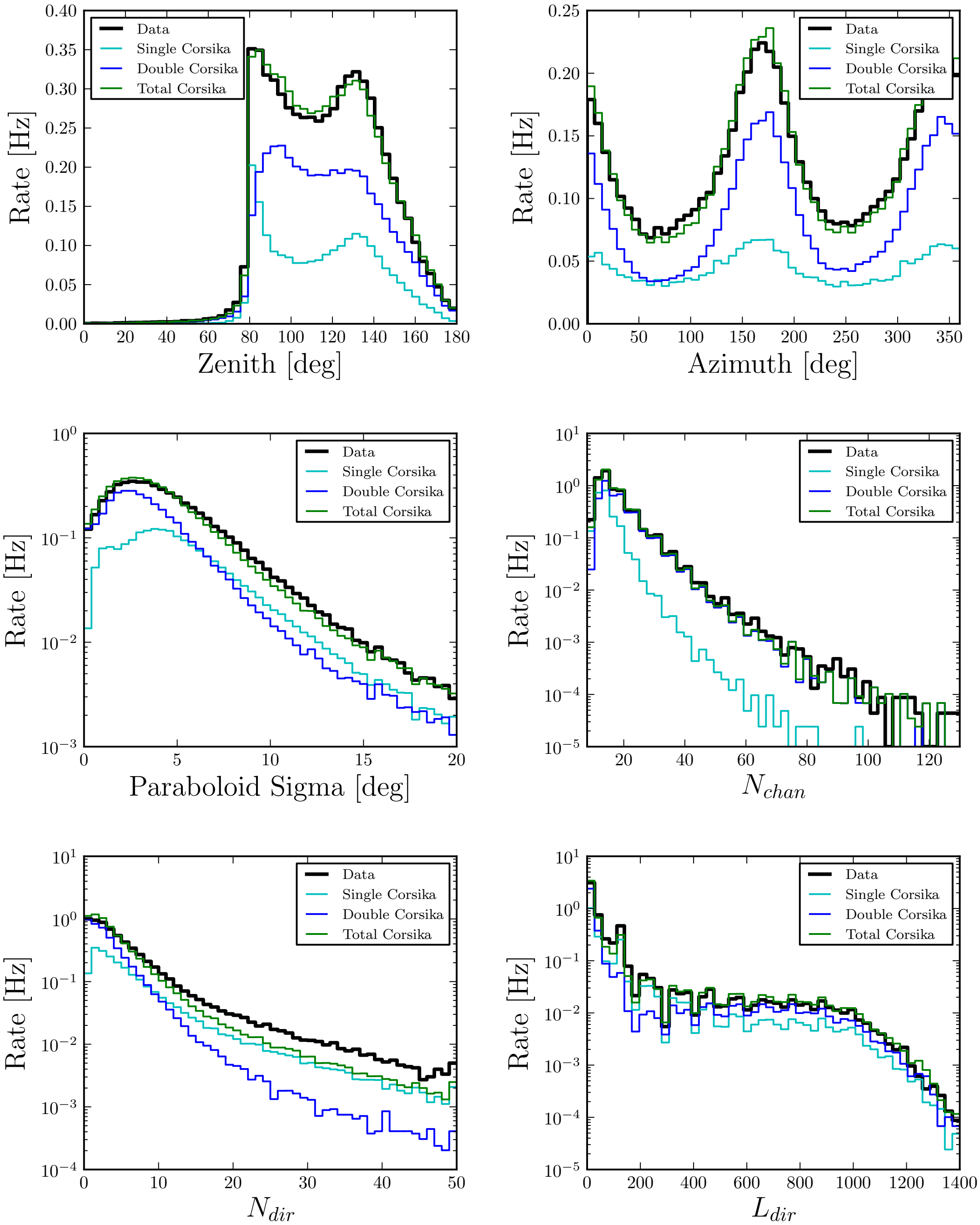

Figure 6.1: Comparison of data and simulation after the good upgoing track cut. Data is shown in black, CORSIKA events containing a single air shower in cyan, CORSIKA simulation with two air showers in blue, the sum of single and double CORSIKA air showers in green. Good agreement is seen in most variables. Disagreement is seen in $N_{dir} > 10$, this discrepancy is not well understood. However, the agreement is acceptable in the region where the final N_{dir} cut is made.

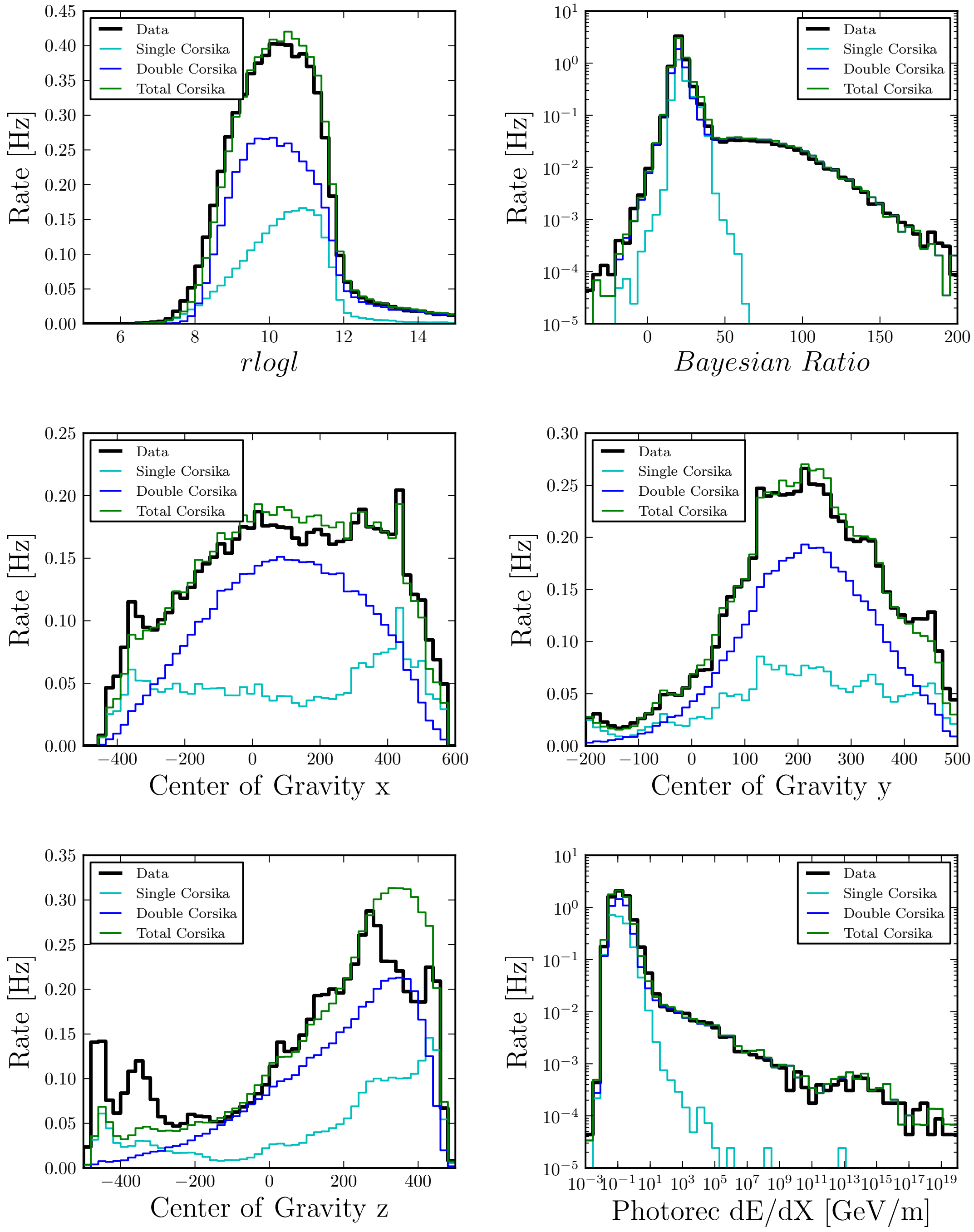

Figure 6.2: Comparison of data and simulation after the good upgoing track cut. Data is shown in black, CORSIKA events containing a single air shower in cyan, CORSIKA simulation with two air showers in blue, the sum of single and double CORSIKA air showers in green. Good agreement is seen in most variables. The disagreement seen in the z coordinate of center of gravity is suspected to be a result of improper modeling of ice properties as a function of z.

track, so there should be a long distance between the first and last direct hit. A poorly reconstructed event will usually have what direct hits they do have close together.

rlogl The value of the log-likelihood value at the minimum is an indicator of how good the reconstruction is. Well reconstructed events will often have deep minima, while poor reconstructions will often be in shallow minima. However, since the log-likelihood is the sum of PDFs for each hit, events with more hits will have a larger log-likelihood value. To compare events with different numbers of hit DOMs, the log-likelihood value is divided by the number of degrees of freedom. This is the number of hits minus the number of free parameters, where the five free parameters are 3 position parameters and 2 direction parameters.

BayesianRatio The Bayesian ratio is the ratio of the minimum log-likelihood value of the zenith weighted Bayesian reconstruction to the unbiased reconstruction. A good reconstruction is expected to occupy a deep valley in likelihood space, while a poor reconstruction is expected to occupy a shallow valley. Biasing the reconstruction so that it finds a minimum in the downgoing direction will greatly affect a likelihood value that found a deep valley, while hardly affecting a likelihood value that was poor to begin with. Well reconstructed events are expected to have a much poorer zenith weighted reconstruction compared to the unbiased reconstruction, and therefore a much higher log-likelihood value than the biased reconstruction. While poor reconstructions are expected to have more similar values for the biased and unbiased reconstructions. Therefore, the log of the ratio of the unbiased reconstruction likelihood to the biased reconstruction likelihood should be higher for well-reconstructed events.

6.4 Optimizing cuts

In order to find the optimum cuts, the Model Discovery Potential (MDP) method is used[275, 276]. This procedure requires doing a full analysis for each point in the cut parameter space that one wishes to investigate. The unbinned likelihood used in the final analysis that will be described in chapter 7 is too slow to effectively use the MDP procedure. Instead, a simplified binned analysis was used to determine the optimal cuts.

In the simplified procedure, an event is considered to be from a GRB if it falls within a set time bin and space bin reducing the result to a counting experiment. The time bin was defined to be the T_{100} time window plus 15 sec on each side. The spatial bin was defined as a circular bin centered on each GRB with a 5° radius. The mean number of observed signal events which fall into the bin for a given cut level, μ_s, is calculated from neutrino simulation weighted by the GRB neutrino spectra calculated in section 5.2. The mean number of background events, μ_b, is calculated using six months of data excluding runs which occurred at the same time as GRBs.

The MDP is then calculated based on μ_s and μ_b. First, the critical number of events required to obtain a discovery, n_{crit}, assuming only background with discovery threshold α is calculated:

$$P_{poisson}(\geq n_{crit}|\mu_b) < \alpha \tag{6.1}$$

Since this is a counting experiment, Poisson statistics are used. The least detectable signal, μ_{lds}, is the signal required to obtain a p-value less than the discovery threshold with statistical power $1 - \beta$:

$$P_{poisson}(\geq n_{crit}|\mu_b + \mu_{lds}) = 1 - \beta \tag{6.2}$$

The model discovery potential is the least detectable signal at a certain cut level divided by the expected signal at the same cut level:

$$MDP = \frac{\mu_{lds}}{\mu_s} \tag{6.3}$$

The cut level which minimizes the MDP has the greatest probability of discovering the given model.

For a 5σ discovery potential ($\alpha = 2.9 \times 10^{-7}$) and a statistical power of $1-\beta = 90\%$, as shown in figure 6.3 the location in cut parameter space with the lowest discovery potential was found to be:

- $rlogl < 8$
- $N_{dir} \geq 5$
- $Ldir > 175$
- $Bayesian\ Ratio > 26$

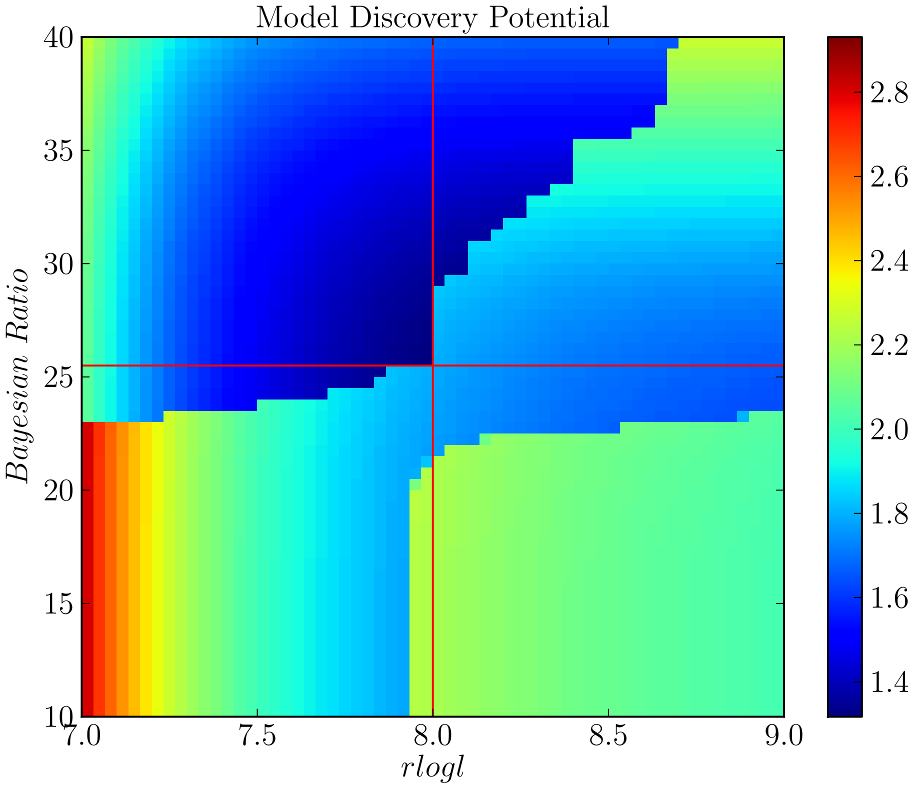

Figure 6.3: The model discovery potential as a function of a 2-dimensional slice of the 4-dimensional cut parameter space. The lower the model discovery potential the larger the chances of discovering the model. The global minimum is marked with red lines to obtain the optimal cut at *rlogl* < 8 and *Bayesian Ratio* > 26. The jumps in the potential are a result of the discrete nature of the Poisson distribution: in the top left region of the plot 2 events are required for a discovery, 3 events in the middle, and 4 events in the bottom right.

After these cuts the background is significantly reduced to 1.5 mHz. These cuts were also found to be close to the optimum cut using the model rejection factor method[277] which finds the parameters most likely to set the lowest limit. A summary of the rates at each cut level is shown in table 6.1. The effects of these cuts on neutrino simulation and off-source data are shown in figures 6.4, 6.5, and 6.6. These cuts reduce the predicted signal from 4.2 total events for all cataloged GRBs to 2.8 events. It is important to note that although it appears that a significant fraction of the signal is removed with these cuts, most of the removed events are events where, although the neutrino was able to trigger the detector, the hit pattern left behind is such that there was insufficient information to properly reconstruct the direction of the neutrino. This can be seen in figure 6.7 where the signal events which are cut have large angular separation between the original direction and the reconstructed direction.

Data and simulation were compared after the final cuts were applied and are seen to be consistent. Plots of this comparison are shown in figures 6.8 and 6.9. After the final cuts the median angular resolution of the signal simulation is 0.95°; the cumulative point spread function is shown in figure 6.10. The resultant effective area of the detector for this analysis is 100 m^2 at 10^5 GeV, the peak of the neutrino

Cut	Data Rate	
Trigger	1100	Hz
Muon Filter	22	Hz
Good Upgoing Cut	2.5	Hz
Final Cuts	1.5	mHz

Table 6.1: Summary table of filter rates.

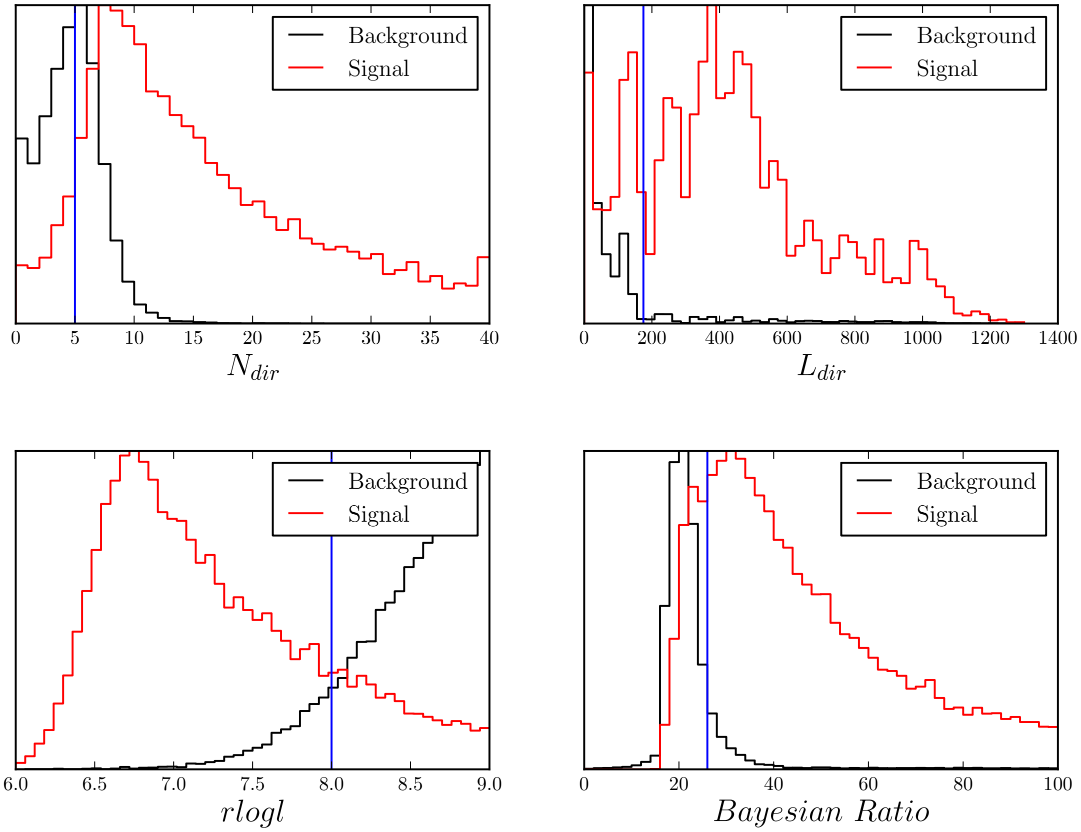

Figure 6.4: Results of model discovery potential cuts are shown. Neutrino simulation is in red and off-source data is shown in black. The y axis is arbitrary; signal and background are normalized separately. The blue vertical lines represent the optimal cut values.

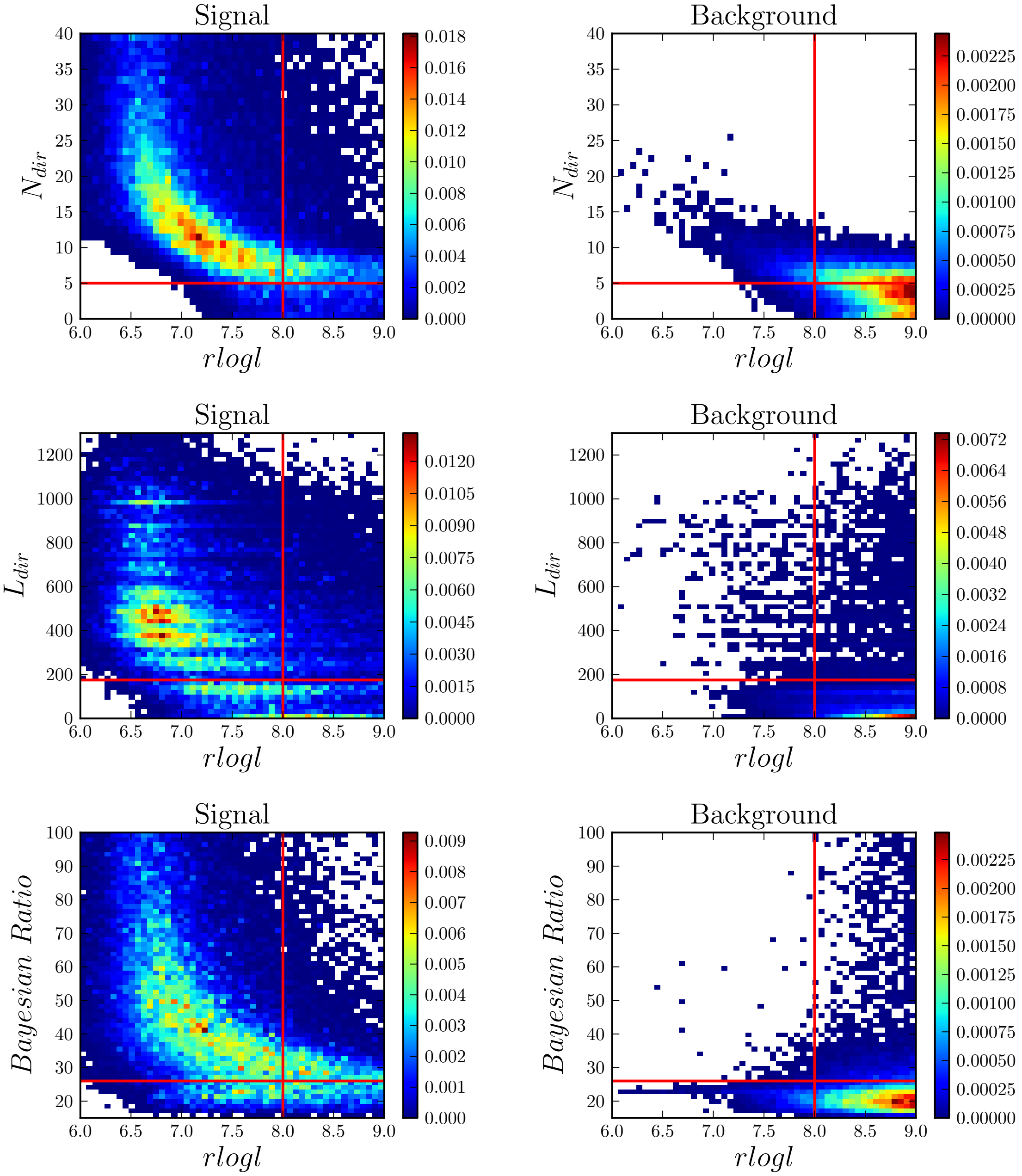

Figure 6.5: Two dimensional plots showing the cut parameter space. Neutrino simulation is to the left and off-source data to the right. Cuts are shown as red lines.

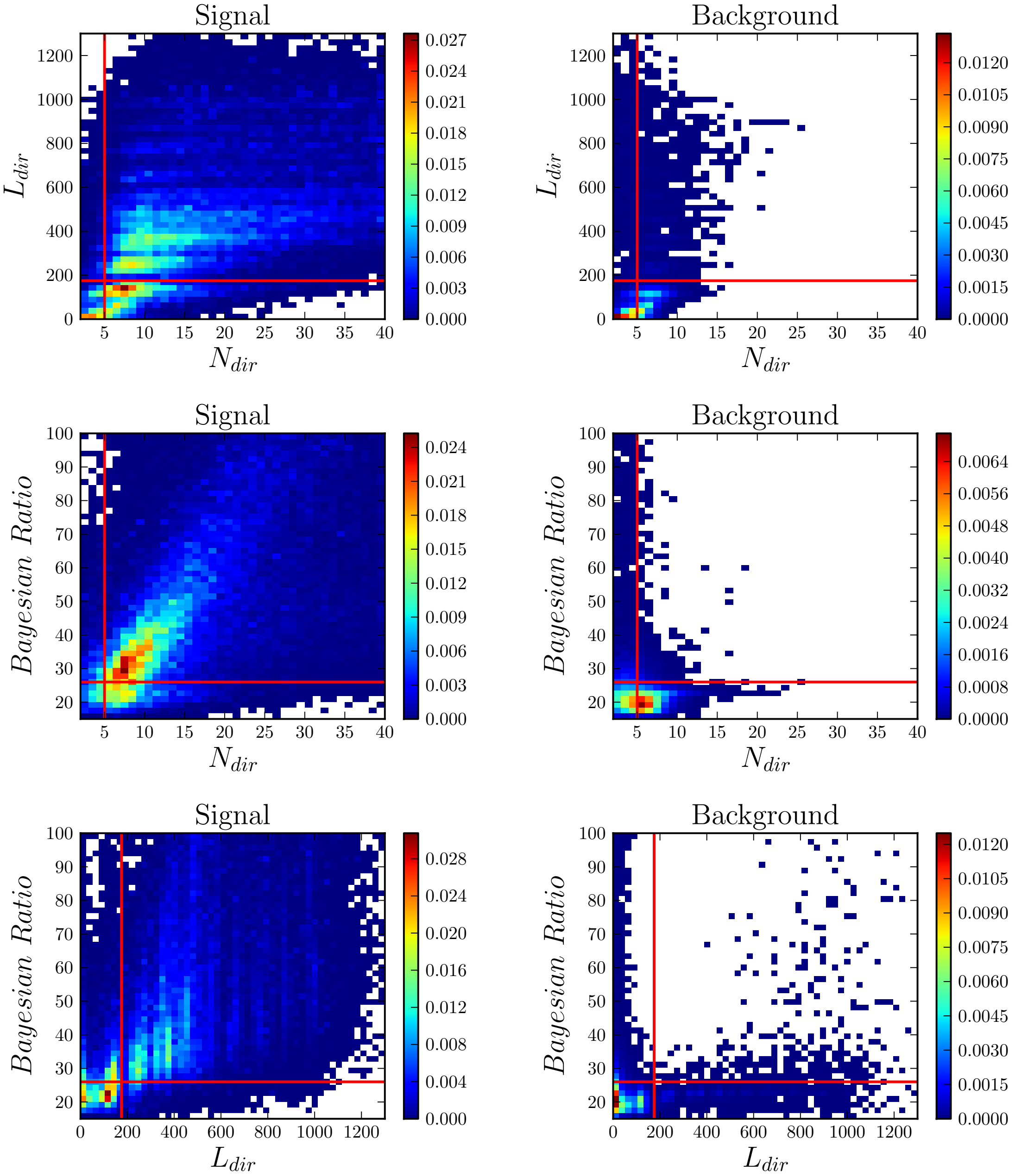

Figure 6.6: Two dimensional plots showing the cut parameter space. Neutrino simulation is to the left and off-source data to the right. Cuts are shown as red lines.

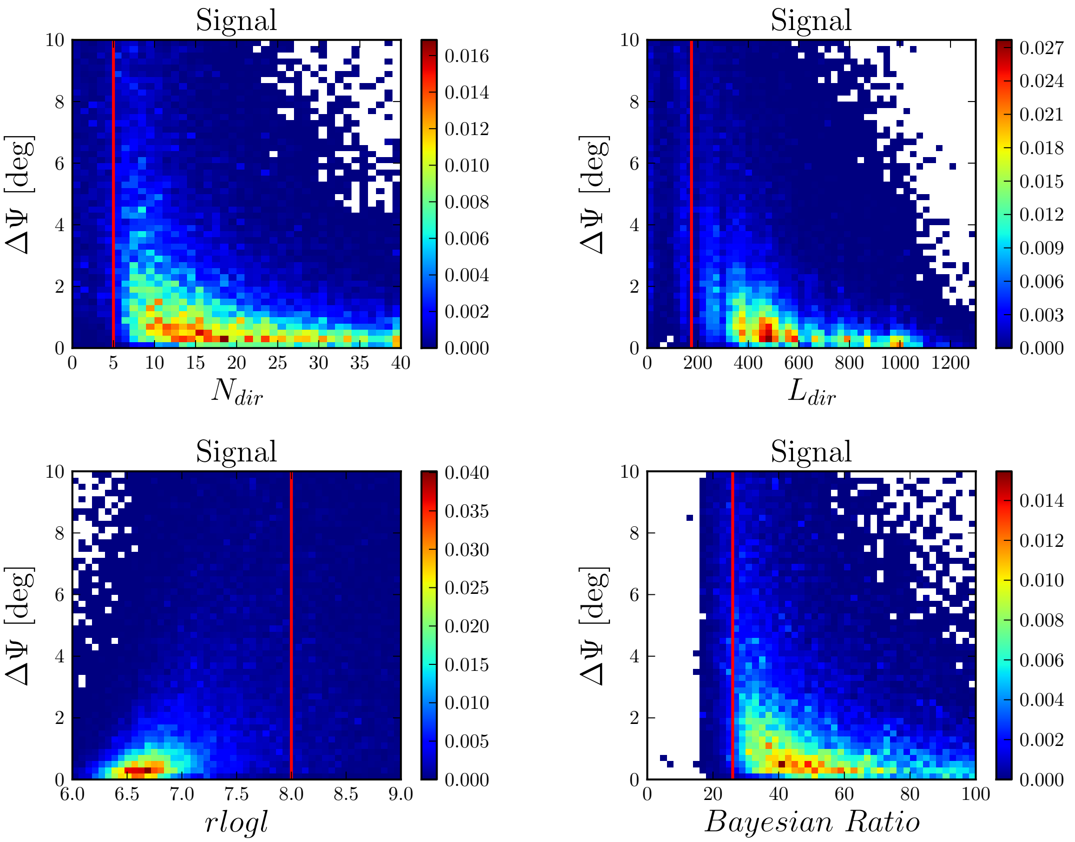

Figure 6.7: Signal event cut variables vs Delta Angle. Delta Angle is the directional difference between the simulated GRB and the reconstruction of the simulated event. Although some signal events are eliminated by the cuts, they have a very broad delta angle distribution signifying that they are poorly reconstructed signal events.

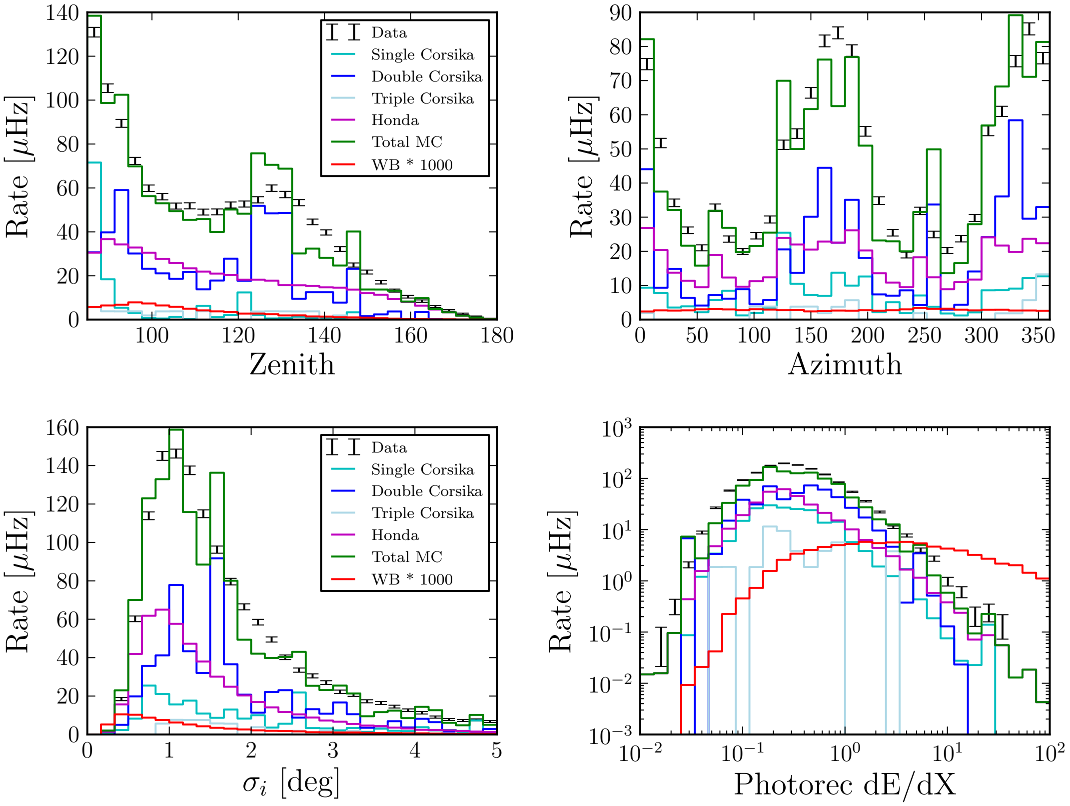

Figure 6.8: Comparison between data and simulation after final cuts. Data is shown in black with error bars. Single, double, and triple down-going air showers simulated with CORSIKA are shown in cyan, blue, and light blue. Atmospheric neutrinos simulated with neutrino-generator and weighted using the predicted flux of Honda is in purple. The sum of expected background events (CORSIKA and Honda) is in green. For comparison, signal neutrinos using the Waxman and Bahcall flux times 1000 are shown in red. Although the statistics are very low for the CORSIKA simulation, data-simulation agreement is acceptable.

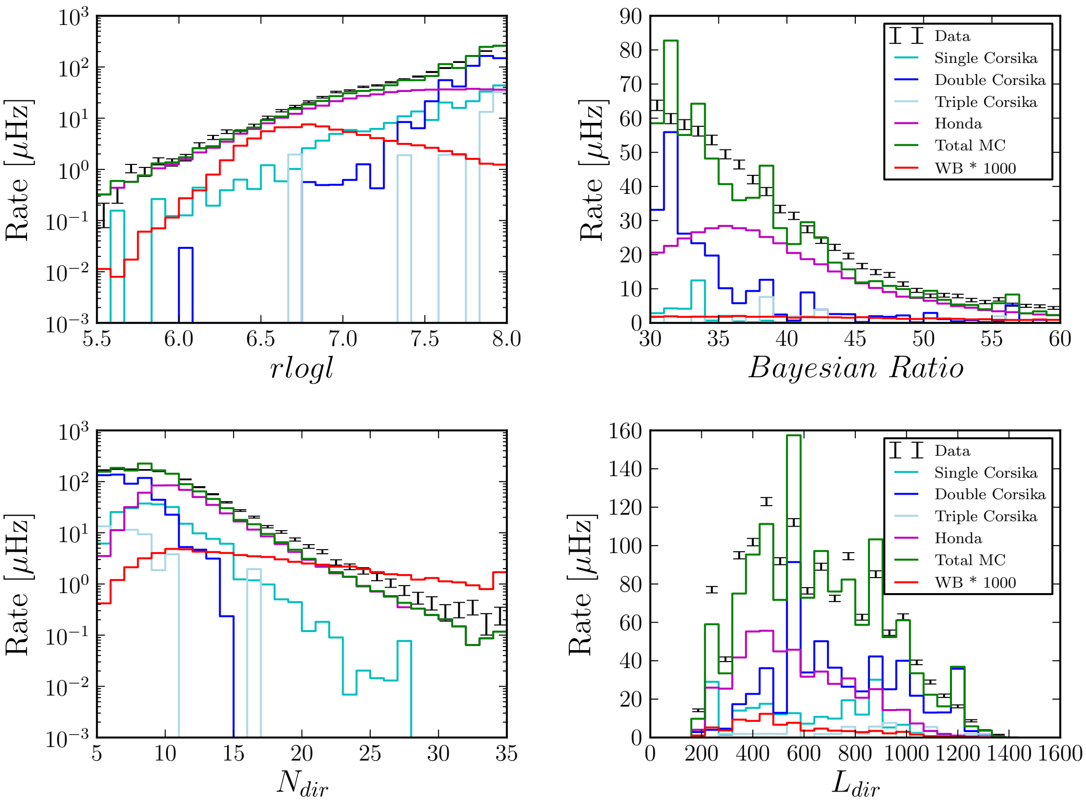

Figure 6.9: Comparison between data and simulation after final cuts. Data is shown in black with error bars. Single, double, and triple down-going air showers simulated with CORSIKA are shown in cyan, blue, and light blue. Atmospheric neutrinos simulated with neutrino-generator and weighted using the predicted flux of Honda is in purple. The sum of expected background events (CORSIKA and Honda) is in green. For comparison, signal neutrinos using the Waxman and Bahcall flux times 1000 are shown in red. Although the statistics are very low for the CORSIKA simulation, data-simulation agreement is acceptable.

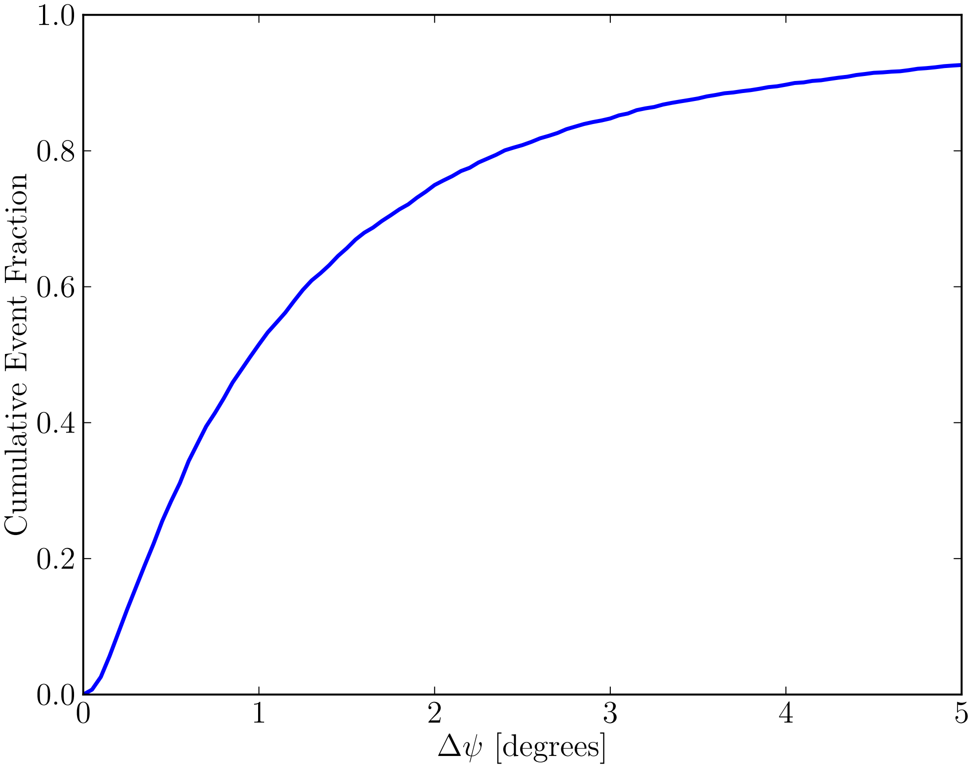

Figure 6.10: Cumulative Point Spread Function of simulated signal events $\Delta\psi$ where $\Delta\psi$ is the angle between the simulated neutrino primary and the MPE reconstruction. The median $\Delta\psi$ is 0.95°.

spectrum. A plot of the effective area as a function of energy and zenith angle is shown in figure 6.11. The simulation samples available for downgoing air showers is limited in size, but is enough to get a rough estimate on the composition of the final event sample. The final sample consists of approximately 15% single downgoing muons, 45% multiple coincident downgoing muons, and 40% atmospheric neutrinos.

It is important to note that there is little reason to cut any harder than necessary in order to get the misreconstructed background on the same order as the irreducible atmospheric neutrino background. Cuts designed to identify coincident downgoing muons, such as split reconstructions, were considered in addition to the cuts listed above but judged to remove too much signal. Most of the misreconstructed downgoing events will have a reconstructed energy that is lower than expected from signal. Adding this as a cut parameter was also considered but the energy will be used in the unbinned method in chapter 7, thus, adding an explicit cut on energy did not improve the sensitivity of the experiment.

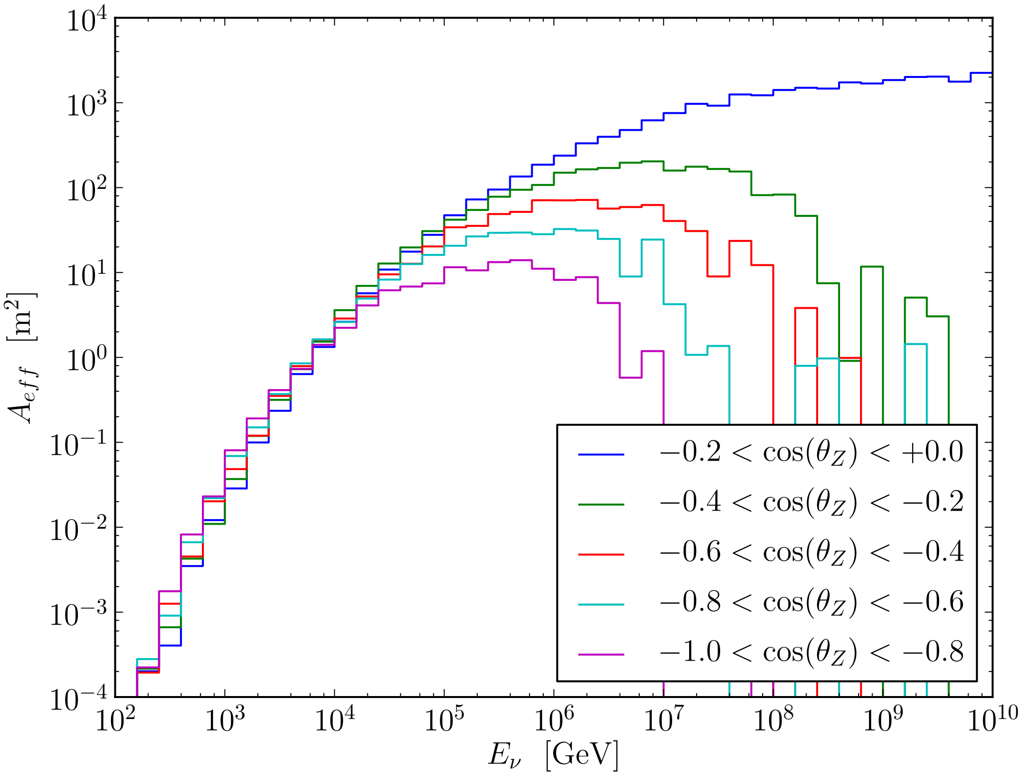

Figure 6.11: Effective Area of IceCube as a function of neutrino energy and zenith angle (θ_Z) after all quality cuts. Effective Area rises sharply with energy between 100 GeV and 100 TeV due to increasing neutrino cross section, increasing muon track length, and increasing light yield. At higher energies the neutrino cross section becomes less dependent on neutrino energy (see figure 4.4), as well as the increased track length and light yield contributing less to detection efficiency. In addition, neutrino losses in the Earth before reaching the detector attenuate the signal at higher zenith angles.

Chapter 7

Unbinned Likelihood Method

This analysis uses an unbinned likelihood method to determine the significance of the experimental measurement. In a binned analysis, the test statistic is the number of discrete events which pass a certain criteria and the significance of observing each number is determined by Poisson statistics. An unbinned analysis differs by assigning a real number value of how signal-like and how background-like each event is. This method is based on the unbinned likelihood analysis developed to look for steady state point sources in IceCube[278]. Only events which passed the quality cuts obtained in chapter 6 are used in the unbinned analysis. The signal-likeness and background-likeness of each event can be expressed as a probability such that given an event is signal, the probability of observing such an event with property x is $S(x)$ and, likewise, given an event is background, the probability of observing such an event with property x is $B(x)$, where x can be any measured property of an event. This method is more sensitive to signal, as signal events which have a high $S(x)$ and a low $B(x)$ will be more significant than observing an additional signal event in Poisson statistics. This method is also more robust against false discoveries, as background events with high $B(x)$ and low $S(x)$ will be less significant than observing an additional background event in Poisson statistics.

A function is needed to convert an observation of N events with properties

$\{x_i\} = x_1, x_2, \ldots, x_N$, where N is unknown before the observation is made, and probabilities $S(x)$ and $B(x)$ into a single test statistic. This function, which is based on the principle of maximum likelihood is derived in appendix A. The definition of the signal and background probabilities used in this analysis are described in the next section. There is no analytic probability distribution function that will represent the distribution of the test statistic. Instead, the distribution of the test statistic is derived numerically using a large number of pseudo-experiments as described below in section 7.2.

7.1 Definition of probabilities

In order for this analysis to significantly distinguish a GRB neutrino from background, $S(x_i)$ and $B(x_i)$ must be as different as possible. The most straightforward separation are spatial and temporal differences; a neutrino must come from the same direction as the GRB in question. For temporal separation, this analysis assumes that neutrinos are generated in the fireball and thus arrive at the same time or close to the same time as the gamma-ray emission. In addition, the energy spectrum of GRBs is expected to be much harder than the background of atmospheric neutrinos and misreconstructed cosmic ray air showers. Thus, the signal and background probabilities will each be defined as the product of three normalized PDFs.

$$S(x_i) = PDF^{S}_{sig}(\vec{x_i}) \times PDF^{T}_{sig}(t_i) \times PDF^{E}_{sig}(E_i) \tag{7.1}$$

$$B(x_i) = PDF^{S}_{bg}(\vec{x_i}) \times PDF^{T}_{bg}(t_i) \times PDF^{E}_{bg}(E_i) \tag{7.2}$$

where each term is a normalized PDF with subscripts denoting signal or background and superscripts representing space, time, or energy. $\vec{x_i}$ represents the spatial coordinate of an event, t_i represents the time of an event, and E_i represents the energy of an event.

7.1.1 Spatial PDF

The spatial PDF for signal is defined as a 2-dimensional Gaussian

$$PDF^{S}_{sig}(\vec{x_i}) = \frac{1}{2\pi\sigma_i^2}\exp\left(-\frac{r_i^2}{2\sigma_i^2}\right) \tag{7.3}$$

where r_i is the angular difference between the direction of the GRB and the reconstructed direction of event i. The width of the Gaussian is a combination of the localization error of the GRB, σ_{GRB} (defined in section 5.2), and the paraboloid error of neutrino direction reconstruction, σ_ν (defined in section 4.4.5).

$$\sigma_i^2 = \sigma_{GRB}^2 + \sigma_\nu^2 \tag{7.4}$$

The background spatial PDF is constructed by creating a 2-dimensional histogram of the direction of all off-source events, shown in figure 7.1. A 2-dimensional spline was fit to the histogram using the statistical error as the fitting tolerance. Discontinuities within PDFs are undesirables, thus the three copies of the histogram were tiled in the azimuthal direction so that near azimuth=0° the spline fit will take bins near azimuth=360° into account and vice versa. Similarly, the bins at the

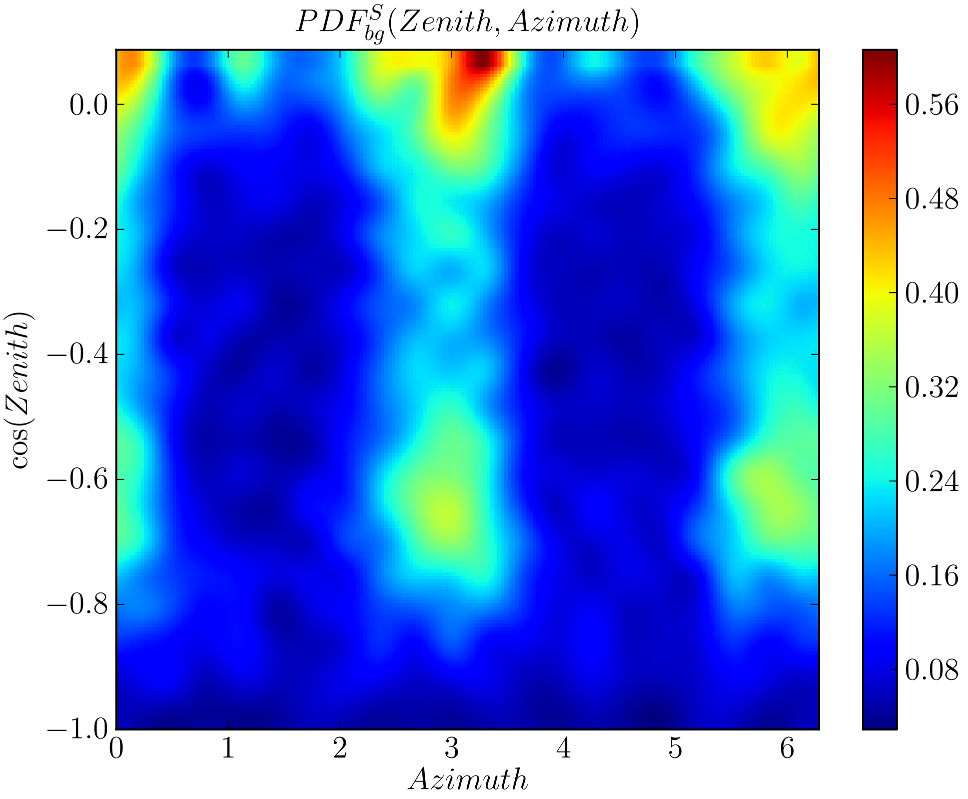

Figure 7.1: The normalized background PDF. The color indicates the probability that an event with spatial reconstruction (Zenith,Azimuth) is a background event. This PDF was created by histogramming all off-source events in detector coordinates and fitting to a 2-dimensional spline. The map was repeated three times in the azimuthal direction to avoid a discontinuity at Azimuth=0. An additional bin (not shown) was created at Zenith=180° to avoid a discontinuity at the pole. The Azimuthal asymmetry is a result of the geometrical asymmetry in the detector.

North Pole (zenith = 180°) were replaced with a single bin with the average value.

7.1.2 Time PDFs

The signal time PDFs are constructed assuming continuous emission during the prompt gamma-ray phase of the GRB and no emission at any other time. In order to avoid discontinuity in the PDF and to account for any timing errors that might occur on the order of one second, Gaussian tails are added to the PDF. The width of the Gaussian tails are set to $T_{100} = T_2 - T_1$ unless $T_{100} < 2$s or $T_{100} > 30$s in which case the width is set to 2s or 30s. The minimum width of 2 seconds was chosen because it is an upper bound of all possible timing errors, while a maximum of 30 seconds is imposed as 30 seconds is believed to be an upper bound on the difference in time between any gamma-ray emission and neutrino emission for bursts lasting longer than 30 seconds. Example time PDFs are shown in figure 7.2.

Changes in the atmosphere over the course of the year result in a seasonal variation in the downgoing cosmic ray air showers[247, 248]. This results in approximately 10% variation in the background rate at final cut level (shown in figure 7.3) This could in principle be introduced as a seasonal change to the background time PDF, but the effect on the analysis is very small. The background PDF is set to be a constant across the entire time window at all times of the year. The seasonal variations will be considered a systematic error on the background.

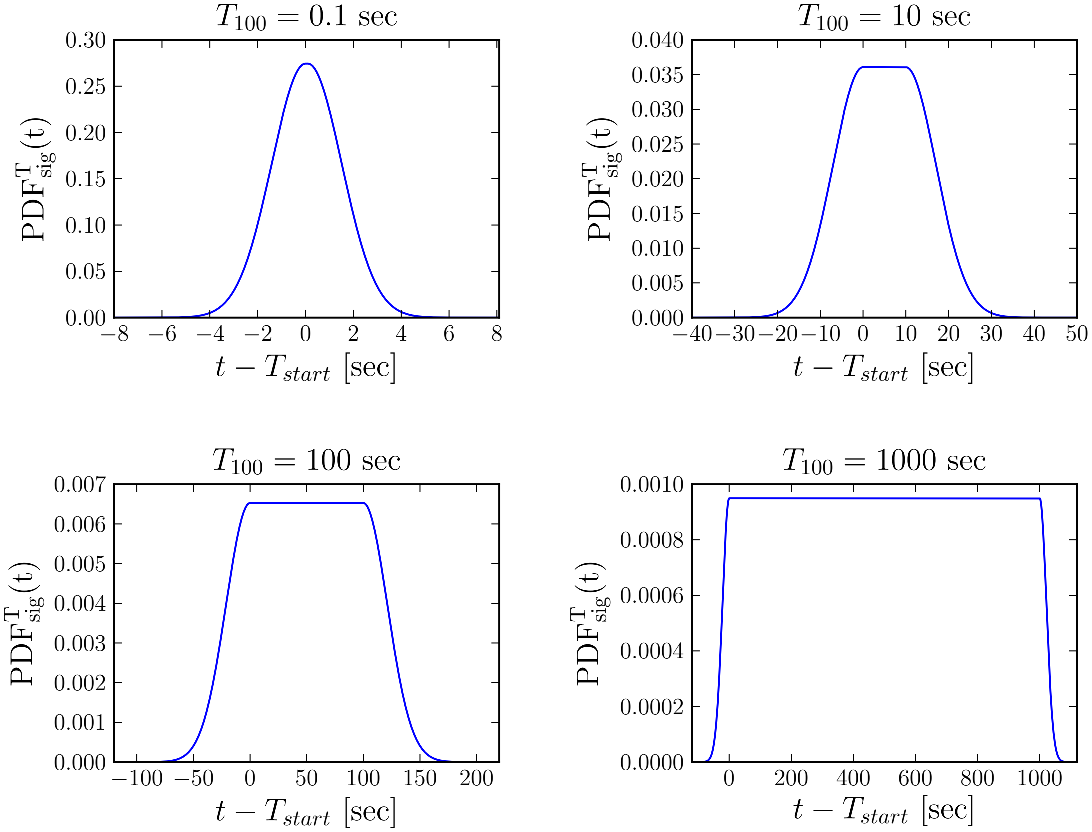

Figure 7.2: Example Time PDFs for $T_{100} = 0.1, 10, 100, 1000$ s. The PDF is flat during the prompt gamma emission phase of the GRB. Gaussian tails are added to the beginning and end of the phase in order to smooth the PDF as well as account for any timing errors or extended emission. The width of the Gaussian tail is T_{100} if $2 \text{ s} < T_{100} < 30$ s otherwise it is 2 s or 30 s.

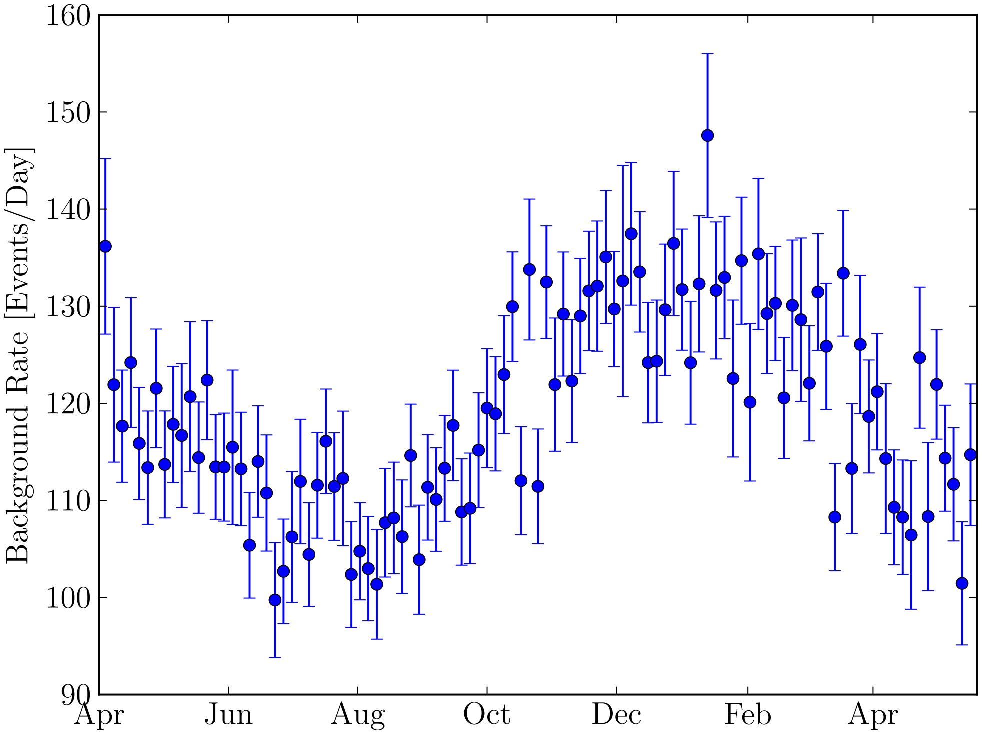

Figure 7.3: Seasonal variations in the atmosphere cause variations in the rate of off-source data at the final cut level. The amount of background fluctuation is $\sim 10\%$. Rather than include this into the unbinned method as a probability, this is treated as a systematic error.

7.1.3 Energy PDF

Since individual atmospheric neutrino events are indistinguishable from astrophysical neutrinos, no reconstruction quality cuts can be used to remove this irreducible background. The mechanisms for creating high energy neutrinos in GRBs predict a much harder spectrum than the observed atmospheric neutrino spectrum, thus to increase the sensitivity of this experiment energy will be incorporated into the likelihood. Adding an energy term to the likelihood will optimize the analysis for whichever spectrum is chosen as the signal PDF, and since the atmospheric spectrum is so soft, any signal PDF harder than the atmospheric spectrum will result in a significant gain in sensitivity for any signal spectrum harder than atmospheric.

The energy loss per unit length estimator $\mathrm{d}E/\mathrm{d}X$ from section 4.4.7 will be used as the energy proxy. The spectrum of reconstructed energy losses from the GRB simulation described in section 4.3 was used to construct the signal energy PDF. Off-source data was used to get the background PDF, however there is not enough data to get a statistically significant PDF from data above an energy loss of 10 GeV/m ($E_{\mu,CoG} \gtrsim 3 \times 10^5$GeV). Instead, atmospheric neutrino simulation is substituted for data above $\mathrm{d}E/\mathrm{d}X > 10$GeV/m. This is justified even though the fraction of atmospheric neutrinos in the sample is around 45%, because misreconstructed downgoing events usually have photorec values significantly smaller that 10 GeV/m.

Both signal and background energy PDFs are shown in figure 7.4. Since the PDFs are never evaluated individually, and only the ratio $PDF^E_{\mathrm{sig}}(E)/PDF^E_{\mathrm{bg}}(E)$ is ever evaluated, the two PDFs are first divided and then fitted with a spline to make

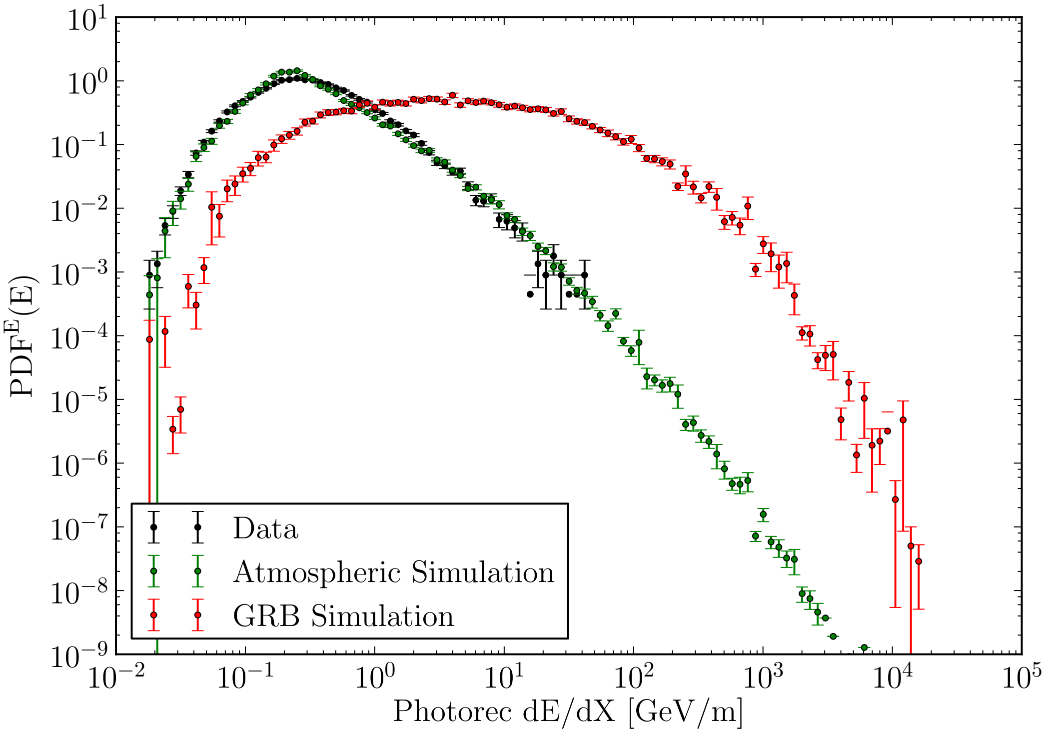

Figure 7.4: Energy PDF obtained by normalizing the observed energy spectra of signal and background. Red indicates the energy PDF of signal. Green indicates the energy PDF of atmospheric neutrinos. Black indicates the energy PDF of off-source data. The background PDF is constructed by using off-source data for $\mathrm{d}E/\mathrm{d}X < 10$ GeV/m and atmospheric simulation for $\mathrm{d}E/\mathrm{d}X > 10$ GeV/m

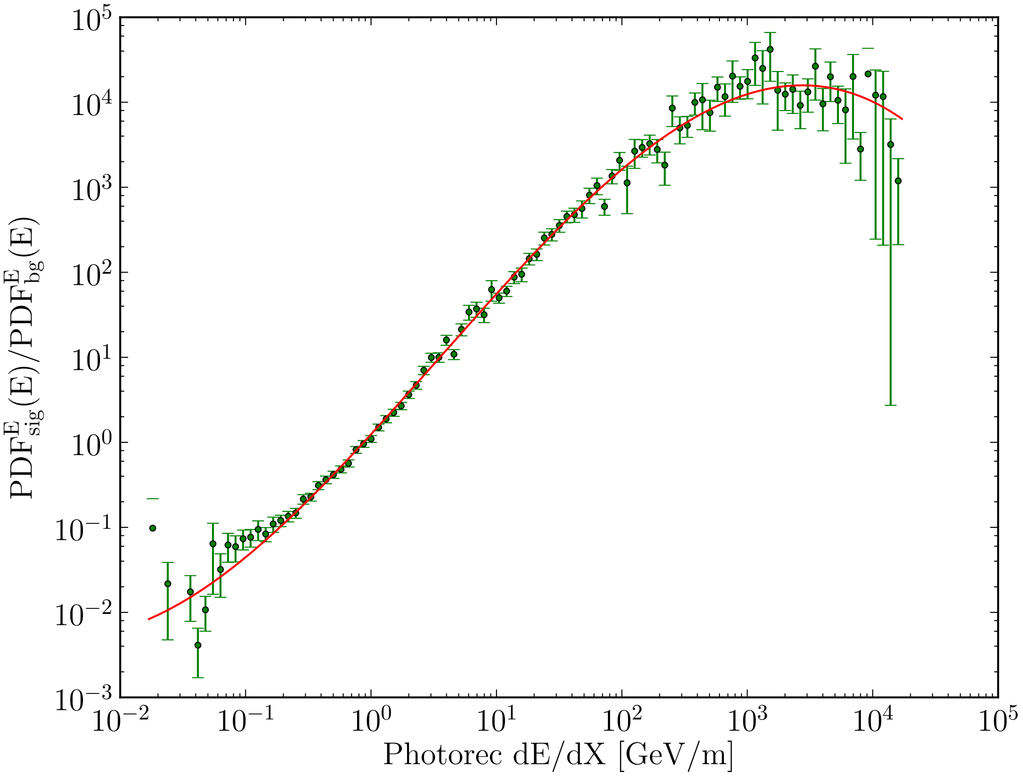

Figure 7.5: The ratio of the signal to background PDF in green with statistical error bars. The spline fit used to evaluate the PDF ratio of events is shown in red. Note the feature above $\mathrm{d}E/\mathrm{d}X > 10^3$ GeV/m is not a statistical fluctuation. The GRB spectrum softens for energies above $\sim 10^7$ GeV where the GRB spectrum is dominated by synchrotron losses in pions and muons.

the PDF ratio shown in figure 7.5.

7.2 Probability Trials

The distribution of the ratio $S(x_i)/B(x_i)$ for all events in the off-source sample and for the simulated signal is shown in figure 7.6. In order to obtain a p-value for the experiment, a test statistic must be defined. The likelihood function derived in

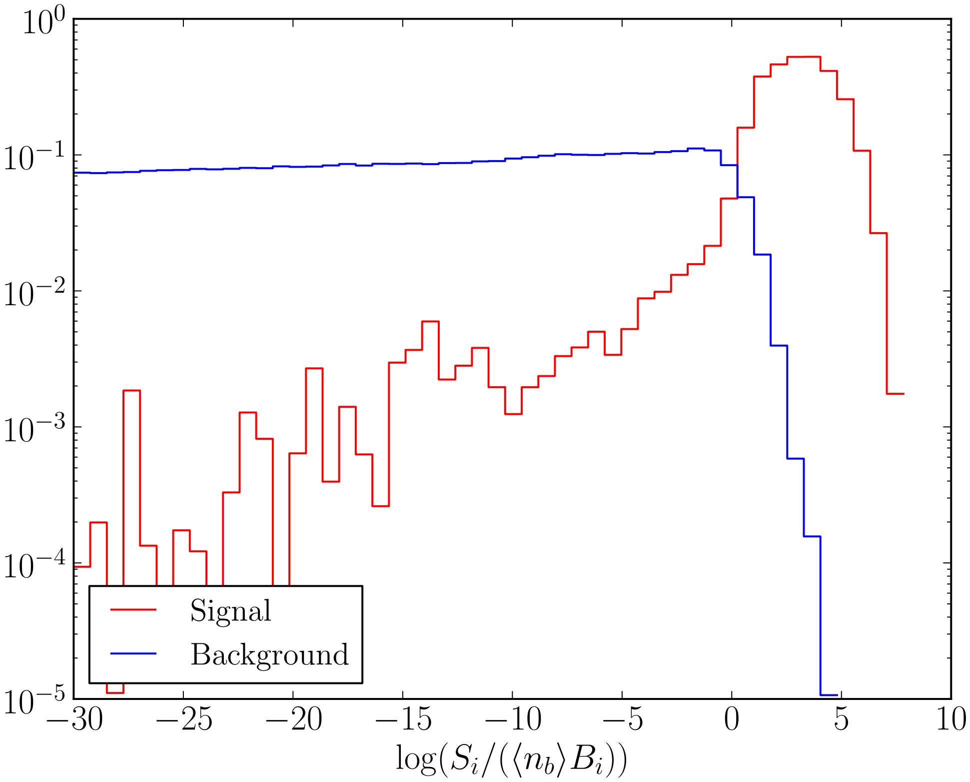

Figure 7.6: The distribution of the signal to background ratio $(S_i/(n_b B_i))$ of all events in the sample. Simulated signal events are in red, while off-source data events are blue. The signal events peak sharply around 10^3, while background events are flat below 1 and drop off sharply above 1.

appendix A is used.

$$\ln \mathcal{L}_R(\{x_i\}; n_s) = -n_s + \sum_{i=1}^{N} \ln\left(\frac{n_s S(x_i)}{\langle n_b \rangle B(x_i)} + 1\right) \tag{7.5}$$

The sum over i refers to all N events which pass the final level of quality cuts in the on-source time window. $\langle n_b \rangle$ is the number of background events expected to be in the on-source time window, which is found from off-source data to be 33.7. The estimator for the number of signal events, $\hat{n}_s$, is the value of n_s which maximizes $\mathcal{L}_R$. We define the test statistic, $\mathcal{T}$, as the value of $\mathcal{L}_R(\{x_i\}; n_s)$ at the maximum:

$$\mathcal{T} = \mathcal{L}_R(\{x_i\}; \hat{n}_s) \tag{7.6}$$

This is the value that will be used to determine the significance of the experiment.

The null PDF is determined by taking 10^8 pseudo-experiments where background data is given randomized times. To save processing time when performing random pseudo-experiments, an additional cut of $S_i/(n_b B_i) > 1$ is performed. This is justified because more than 99% of signal occurs in this region while it excludes 90% of background, as values of $S_i/(n_b B_i) \ll 1$ do not affect the value of the test statistic significantly. The processing time saved is significant.

An alternative method of obtaining the null PDF is suggested by Wilks' theorem[279] which states that the distribution of $2\mathcal{T}$ should be a χ^2 distibution. However, as pointed out by Braun *et al.*[278], this only applies when there is a suffient number of events with high signal probabilites. Thus when using Wilks' theorem

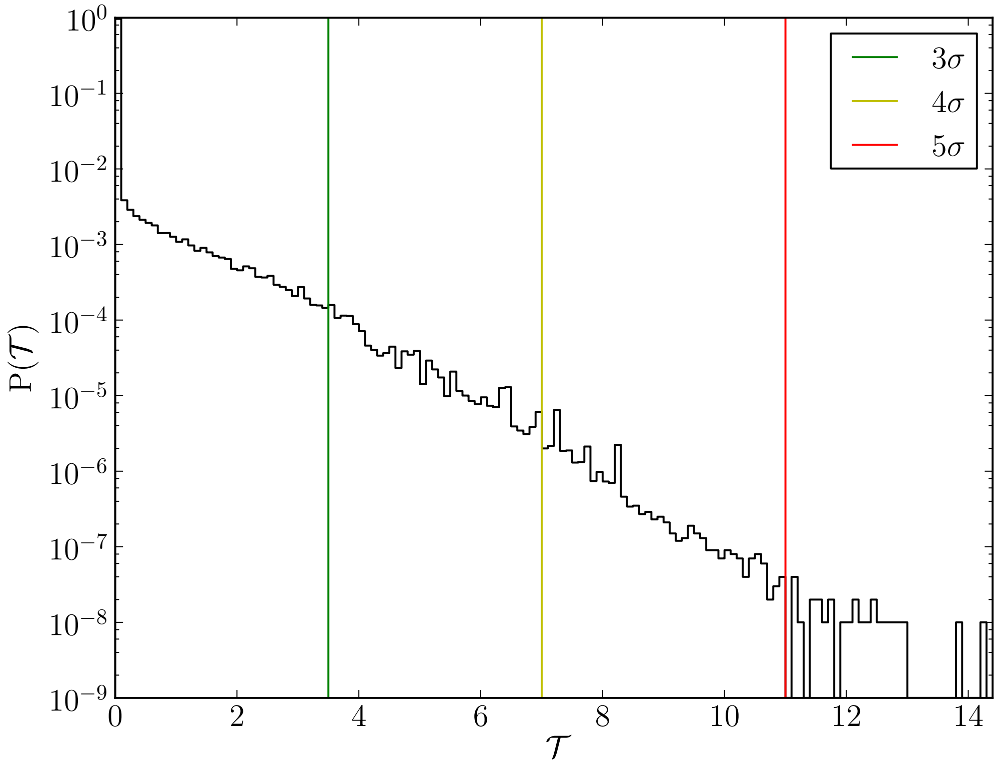

Figure 7.7: The differential null PDF is the normalized distribution of the test statistic, $\mathcal{T}$, obtained from randomized pseudo-experiments. Note: the large spike at $\mathcal{T} = 0$ indicates there is a 96% chance that no events will pass the $S_i/(n_b B_i) > 1$ cut and result in a test statistic of 0. The 3, 4, and 5 sigma discover thresholds are shown in dark green, light green, and red respectively.

to characterize the background, it is still nescessary to use pseudo-experiments to characterize part of the distribution. In addition, the $S_i/(n_b B_i) > 1$ cut removes the χ^2 distribution behavior, such that using Wilks' theorem actually increaces the time it takes to calculate the null PDF. It was for this reason that Wilks' theorem was not used.

The obtained null PDF is shown in figure 7.7. The five sigma significance threshold is determined as the value of $\mathcal{T}$ such that 28 of the 10^8 pseudo-experiments exceed it.

Next, to determine an estimator for the signal flux, pseudo-experiments are performed with simulated signal superimposed on background with randomized times. The signal simulation is reweighted with an overall signal strength μ such that $\mu = 1$ corresponds to the signal strength calculated in section 2.6. The shape of the energy spectrum of each burst, as well as the relative flux magnitudes between different bursts, remains unchanged. μ values from 0 to 3 in steps of 0.001 are evaluated. Several traces with different signal strengths are shown in figure 7.8. From these distributions, one-sided 90% confidence intervals[243–245] are constructed as follows: for each value of μ, a confidence belt is found such that, for repeated experiments, the probability of observing a test statistic greater than $\mathcal{T}_1(\mu)$ is 90%. This function is then inverted so that $\mu_1(\mathcal{T})$ is a function of $\mathcal{T}$ such that for an observed value of $\mathcal{T}$, $\mu_1(\mathcal{T})$ is an upper limit for μ at the 90% confidence level. A 2-dimensional representation of the test-statistic distribution for each value of μ with the 90% upper limit is shown in figure 7.9. It was decided to use one sided intervals rather than Feldman and Cousins' unified approach to two sided intervals[280] because, in the event of a discovery, the 90% confidence interval might be inconsistent with the observed energy spectrum.

To illustrate the power of this method, note that, in order to make a 5 sigma discovery, a test statistic of $\mathcal{T} \geq 11.0$ is required. The probability of making a discovery as a function of μ for a given discovery threshold is shown in figure 7.10: at $\mu = 1$ the chance of a 5σ discovery is 0.76. No single event in the background

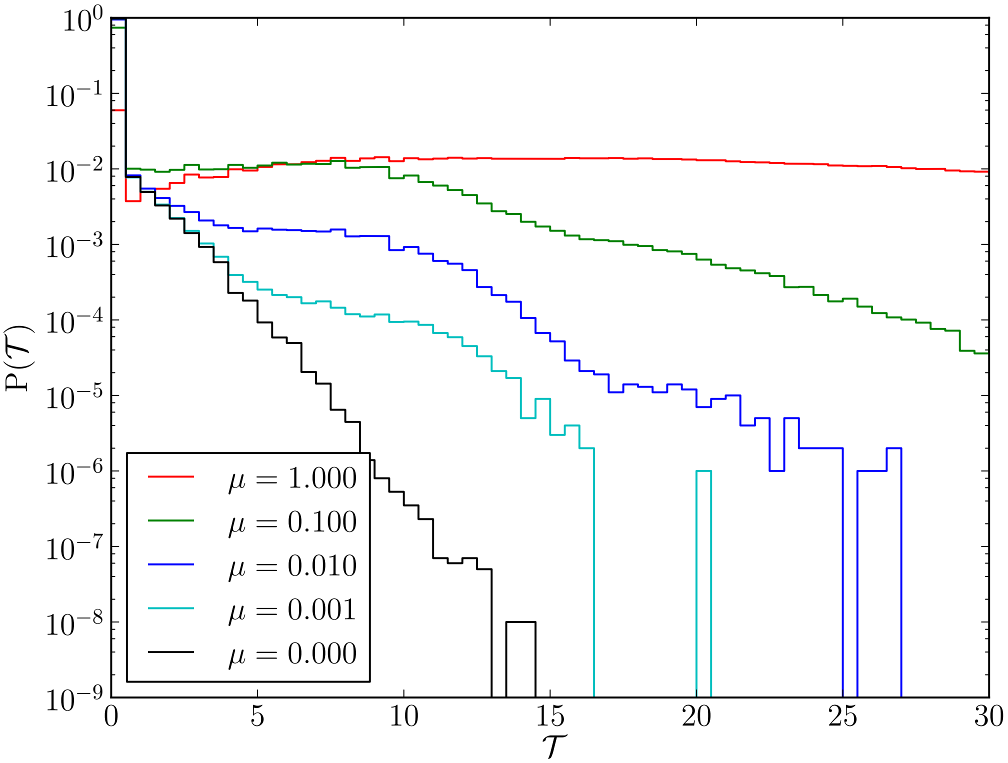

Figure 7.8: The Signal PDFs were constructed similarly to the null PDFs shown in figure 7.7, except that, in addition to background data, simulated GRB neutrinos are added. The GRB neutrino events are reweighted by a signal strength factor, μ, from the weights calculated in section 2.6. The signal PDFs are only calculated from 10^6 pseudo-experiments, resulting in lower statistics. The signal PDFs for multiple μ values are shown, as well as the null ($\mu = 0$) PDF.

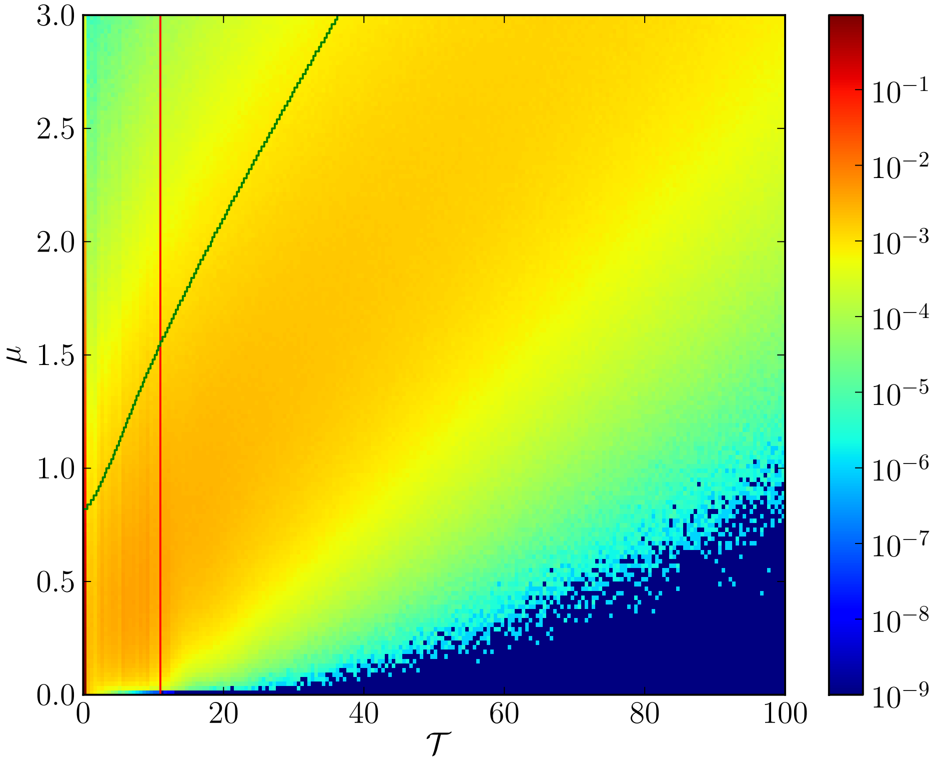

Figure 7.9: The full frequentist plane used to infer μ from $\mathcal{T}$. The color represents the probability of observing $\mathcal{T}$ given a signal strength of μ. The 5 sigma discovery threshold ($\mathcal{T} = 11.0$) is shown as a vertical red line. The 90% one-sided confidence upper-limit is shown in green.

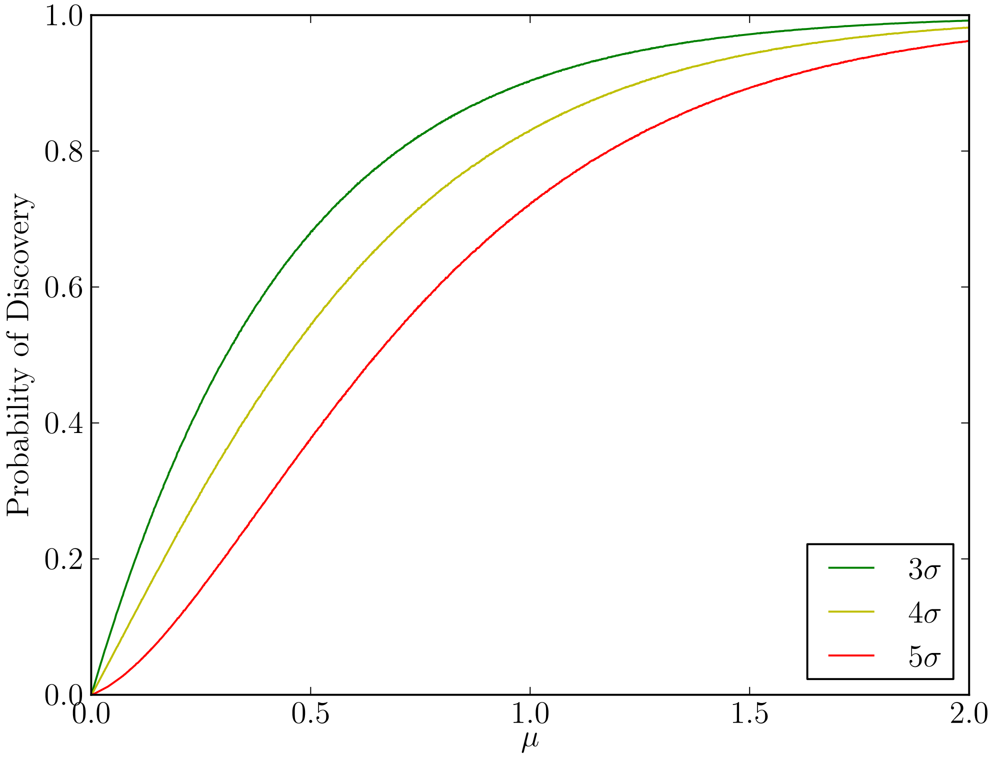

Figure 7.10: The discovery probability, given the signal expectation derived in section 2.6 ($\mu = 1.0$), is shown for 3, 4 and 5 sigma.

sample has sufficient signal to background ratio to result in a 5σ discovery. However, many events in the signal simulation sample with a primary neutrino energy > 100 TeV, would constitute a 5σ discovery as the sole observed event. This shows the power of incorporating the energy into the likelihood method since, without energy in the likelihood, at least two events would be necessary for a 5σ discovery.

The distribution of $\mathcal{T}$, assuming an experiment in which a single event is observed, versus the properties of that event are shown in figures 7.11 and 7.12. As expected there is a strong energy dependence on the test statistic. The most significant background event in the background sample has a test statistic of $\mathcal{T} = 8.2$ below the five sigma discovery threshold, while many signal events above 100 TeV will result in a five sigma discovery as a single event. Additionally, *rlogl* and *BayesianRatio* are correlated with $\mathcal{T}$ even though these quality cuts were not incorporated into the likelihood analysis.

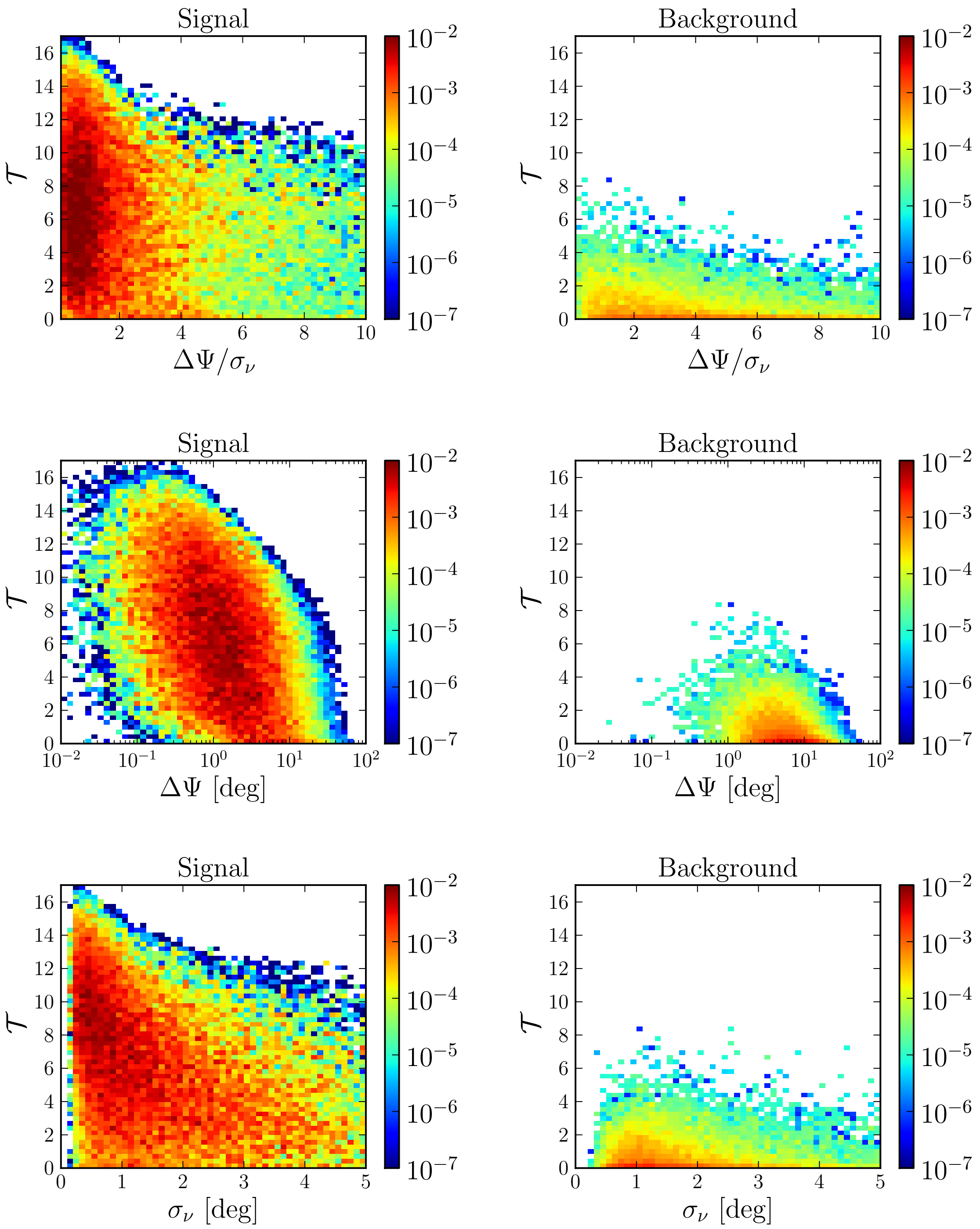

Figure 7.11: The distribution of $\mathcal{T}$ assuming a single event is observed as a function of various variables. Signal is on the left and background on the right. $\Delta\Psi$ is the angular difference between the MPE reconstruction and the GRB in question. σ_ν is the paraboloid positional uncertainty.

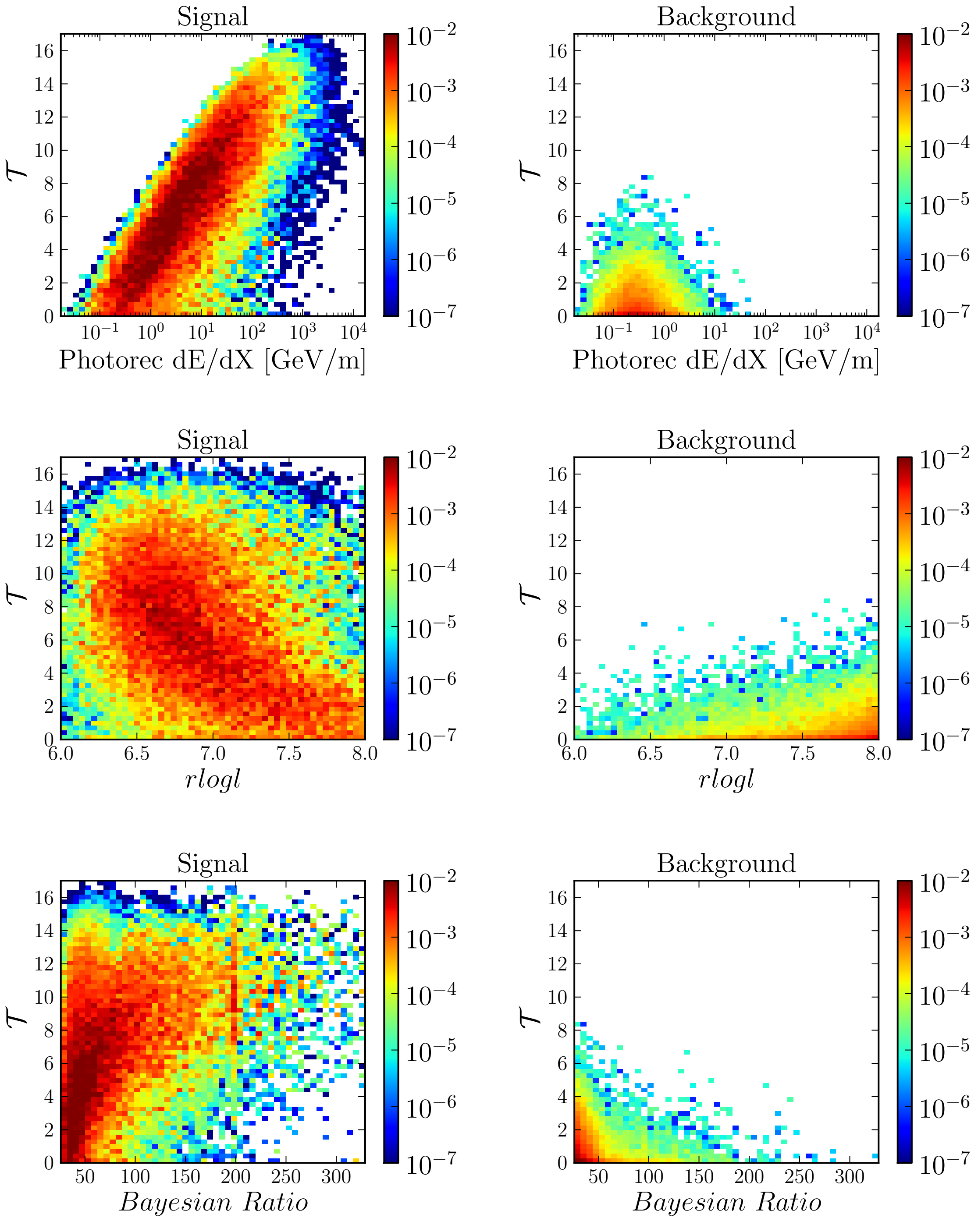

Figure 7.12: The distribution of $\mathcal{T}$ assuming a single event is observed as a function of different variables. Signal is on the left and background on the right. Note that signal events exist above the 5σ discovery threshold of $\mathcal{T} = 11.0$ while no single background event is above this threshold.

Chapter 8

Results

In order to prevent bias in this analysis, a blind analysis was utilized. In a blind analysis, the method for determining the significance of the experiment is determined before the analyzer looks at data in its final form. In this analysis, blindness is achieved using the hidden box method[281] where all data in a defined on-source region is kept blinded. The on-source region was defined to be all data during the same run as that of a GRB. (Runs can last up to eight hours.) The function used to convert on-source data into a test statistic, as well as the null PDF and 90% confidence limit, was determined solely from off-source data without looking into the on-source region. This analysis was reviewed extensively by the IceCube collaboration before unblinding was approved. Once approval was obtained, the on-source data analyzed and the significance and upper limit were determined.

The on-source data contained 36 events over the entire sky compared with the expected $\langle n_b \rangle = 33.7$. The closest of these events to a GRB in the on-source time window was 26° from GRB081126. Since all events were all far from their corresponding GRB, all of these events had $S/(n_b B) < 1$. This results in a test statistic of $\mathcal{T} = 0$ and $\hat{n_s} = 0$ which corresponds to a p-value of 1. As shown on the green line in figure 7.9, observing no events sets a 90% upper-limit on the signal strength of $\mu = 0.802$, excluding the predicted model.

8.1 Systematics

Since this analysis relied on off-source data to describe the background, the systematic uncertainties on the final limit are minimal. Systematics are incorporated into the final limit using a Bayesian marginalization procedure[282–284] where systematic uncertainties are given a Bayesian treatment which are used to calculate frequentist confidence intervals. For each systematic uncertainty, a Bayesian prior is assigned which estimates the bounds of the actual value for that variable; for example a Gaussian centered at the best known value with a width of the quoted uncertainty. The experiment was then repeated for several different values for each systematic variable and the full frequentist plane calculated. The frequentist planes are averaged together weighted by the value of their Bayesian prior. The 90% upper limit is then calculated from the resulting frequentist plane. Since each repetition takes large quantities of computer processing power, systematics were only varied one at a time. Each systematic was given a Gaussian distribution for its Bayesian prior except for the ice model. In this case, each ice model had an equal prior.

The only source of uncertainty from the background is the seasonal variation discussed in section 7.1.2. The amplitude of this variation is $\sim 10\%$, and the effect on the final limit is estimated by repeating the entire analysis with the probability of a background event occurring in the on-source window of each GRB modified by a value between -20% and $+20\%$.

There were also several sources of systematic uncertainty associated with uncertainties in parameters used in simulating the signal that affects the final limit.

Inaccuracies in simulating the propagation of photons through ice can result in inaccuracies in the simulation. The analysis was repeated using signal simulation with three different ice models: the original AHA ice model described in section 4.3, the half-stretched ice model, and the SPICE1 ice model. The half-stretched ice model is based on the AHA model with the scattering and absorption values in regions with clean ice were decreased by 100% but unchanged in regions with dirtier ice[285]. This model was motivated by studies which indicated that the clean ice was cleaner than AHA predicted. The SPICE1 model is a different ice model based on fitting the amplitude instead of the timing of flasher data[286,287]. The quantum efficiency of DOM's PMT directly impacts the amount of light detected by the DOM, the uncertainty of the quantum efficiency is estimated to be ±10% [210]. Uncertainties in the neutrino cross section are on the order of 3% [288]. Changing the neutrino cross section involves competing effects; a lower cross section will result in fewer interactions near the detector but will also result in fewer neutrinos lost while propagating through the Earth. Seven different cross section values were used and the changes in the limit were mostly effected by a few high energy events which propagated without loss through the Earth. As with the neutrino cross section, changing the muon interaction cross section also involves competing effects: higher cross sections result in more light detected while lower cross sections result in longer, but dimmer, tracks. The uncertainties of muon energy loss at the energies considered are on the order of 2-3%[225, 289]. All five muon cross sections were varied in lock-step in values between -3% and $+3\%$.

Systematic Variable	$\sigma_{\text{BaysianPrior}}$	Simulated Range
DOM Quantum Efficiency	10%	85%-115%
Neutrino Cross Section	2%	97%-103%
Muon Energy Loss	2%	97%-103%
Background Rate	10%	80%-120%

Table 8.1: Summary of systematic uncertainties. $\sigma_{\text{BaysianPrior}}$ is the width of the Gaussian used to calculate the Bayesian prior. The third column indicates the range over which frequentist planes were calculated.

The width of the Gaussian used in Bayesian prior and the range of the different values of the systematic uncertainties are listed in table 8.1. The frequentist plane was calculated separately for each point in systematics space, and the limits set by these points in systematics space are shown in figure 8.1. A single frequentist plane was then created by adding all planes together weighted by their Bayesian prior and dividing by a normalization factor. A new one-sided 90% confidence interval is constructed as in section 7.2 which accounts for systematic uncertainties. The final signal strength limit after accounting for systematics increases by 0.020 to $\mu = 0.822$ and is shown in figure 8.2 along with the results of other searches and theoretical expectations.

8.2 Summary

This thesis looked for neutrinos originating from gamma-ray bursts in an attempt to determine the origin of UHECR. Cosmic rays with energies in excess of $10^{18.6}$ eV are observed on earth and must be accelerated by very strong shocks with high magnetic fields. Gamma-ray bursts are a leading candidate for the origin of these cosmic rays because the shocks necessary to accelerate the cosmic rays are a

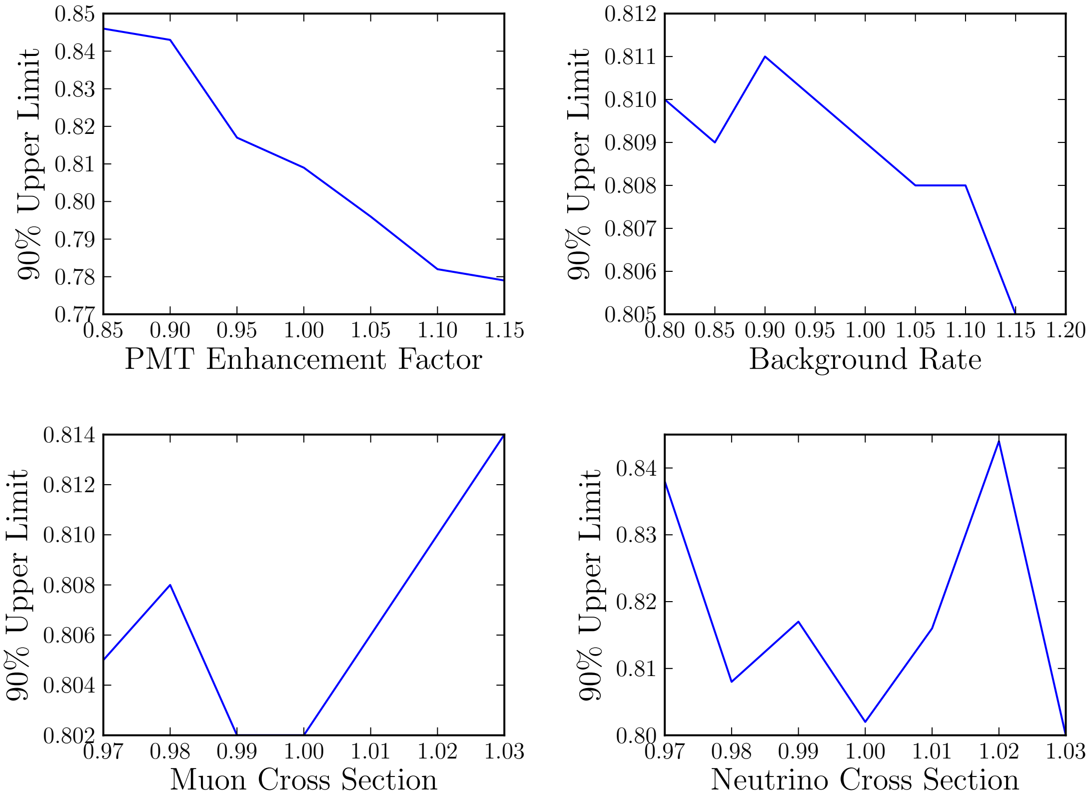

Figure 8.1: Each plot shows the limit set by this experiment through varying a single systematic variable. The horizontal axis shows the parameter which was varied and the vertical axis shows the limit obtained. The limits obtained here only represent one point in systematic variable space. These limits are combined using Bayesian marginalization to obtain a single limit which accounts for all systematics. The muon and neutrino cross sections contribute to competing effects with different Monte Carlo statistics which accounts for the shape of the curve.

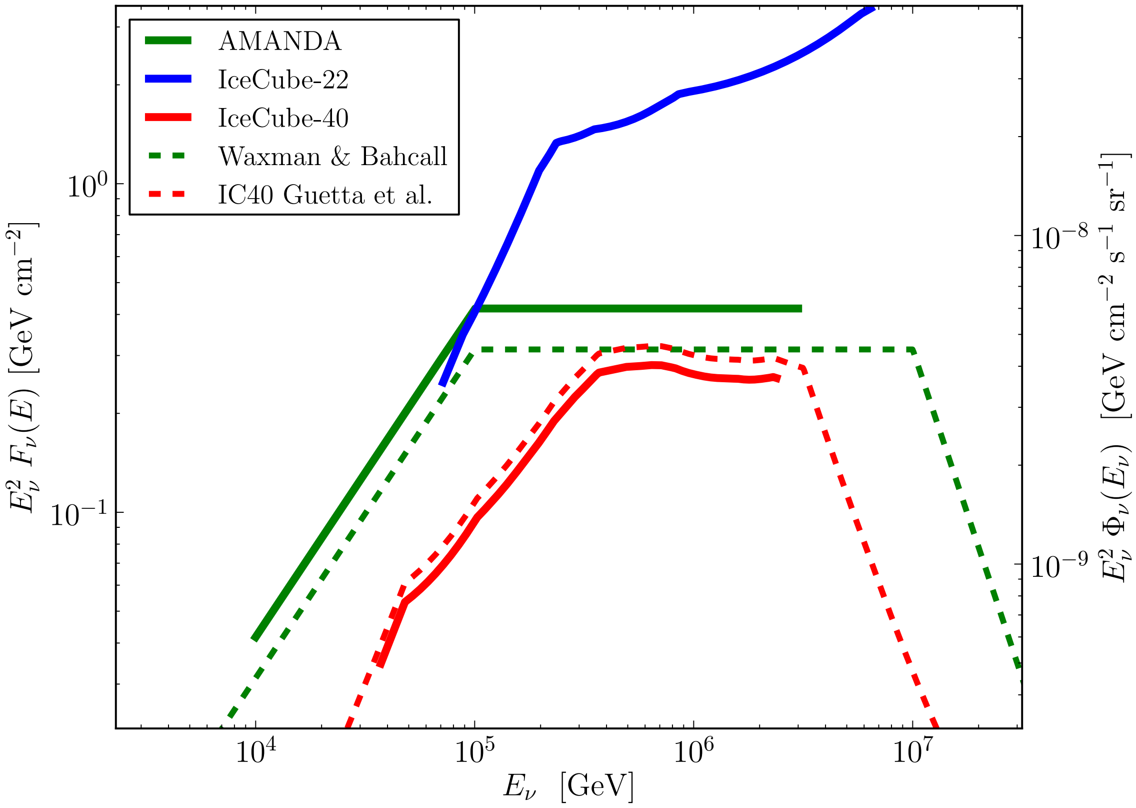

Figure 8.2: The flux limit set by this analysis including systematic error is shown in solid red along with the predicted model shown in dotted red. For comparison the IceCube 22 string limit[28] is shown in solid blue, the AMANDA limit[29] is in solid green, and the Waxman and Bahcall flux[274] in dotted green. The left axis denotes fluence scaled to 117 bursts. The right axis denotes quasi-diffuse flux assuming a total of 667 uniformly distributed bursts per year.

natural part of the fireball model, the leading theory to explain the observed gamma-ray emission. In addition, the aggregate energy flux observed by gamma-ray bursts and UHECR are the same order of magnitude. Since the observed flux of UHECR interacting with the observed flux of gamma-rays in the fireball environment will create an observable neutrino flux, but the gamma-rays and electrons alone will not produce neutrinos, observing neutrinos in coincidence will provide strong evidence that GRBs are the source of UHECR.

Gamma-ray bursts are believed to be the violent death of massive stars where $\sim 10^{51}$ ergs of non-thermal gamma-rays are emitted on the time scale of seconds to minutes. The fireball model explains how this occurs. Gamma-rays bursts can have one of two progenitors: 1) a super massive star collapses into a black hole or 2) either a neutron star-black hole system or a double neutron star collide to create a black hole. In either case a black hole is created in an environment which leads to very rapid accretion. This accretion creates a plasma at the rotational poles of the black hole which expands under radiation pressure to relativistic speeds. Collisions between different subshells of the plasma will create shock fronts which cause the first order Fermi acceleration of electrons. As the plasma spreads out it becomes transparent to gamma-rays at a certain radius. Past this radius, accelerated electrons can then radiate non-thermally to create the observed gamma-ray emission. The shells of plasma then interacts with the interstellar medium which causes the observed x-ray, optical, and radio afterglow. If hadrons are present in the fireball then they should be accelerated by the same shocks which accelerate the electrons. The accelerated hadrons should then interact with the gamma-rays through the delta resonance to create pions which decay to neutrinos.

To search for neutrinos in coincidence with GRBs the IceCube Neutrino observatory was used in a half-complete, 40 string configuration. 117 bursts were observed in the northern hemisphere by satellites while IceCube was operating in its 40 string configuration. Neutrinos are distinguished from cosmic ray muons in IceCube by selecting only upgoing events. Since the rate of misreconstructed downgoing events was much higher than the rate of neutrinos, quality cuts were devised to separate these two classes of events. In order to optimize quality cuts a neutrino signal spectrum had to be chosen. The chosen spectrum was obtained by calculating the resulting neutrinos expected from the observed cosmic ray spectrum of protons interacting with the observed gamma-ray spectrum through the Δ resonance. The quality cuts were then optimized for discovery using a simplified binned analysis that assumed Poisson statistics, with off-source data used as background and simulated neutrinos with the calculated spectrum for the signal. After applying the quality cuts the remaining sample of off-source data contained approximately 45% atmospheric neutrino and 55% misreconstructed cosmic ray muon events.

To look for neutrinos in coincidence with gamma-ray bursts an unbinned maximum likelihood analysis was used. In this method, for each event observed, the probability that an event is from a GRB is calculate in both the spatial and temporal coordinates. In addition, since the spectrum from GRBs is believed to be much harder than the atmospheric neutrino background, energy is added as a third probability. The product of all probabilities of all events in the sample are combined to form the likelihood that the sample contains emission from gamma-ray bursts. This likelihood was then used as the test statistic. The off-source data was then used to calculate the distribution of the test statistic assuming a no source hypothesis by performing 10^8 pseudo-experiments. From this distribution a five sigma discovery threshold was obtained. Then neutrino simulation weighted with the energy fluence theory of Guetta *et al.* was injected into pseudo-experiments to obtain a 90% confidence limit as a function of the test statistic.

After approval by the collaboration the on-source data was unblinded. No events were observed in coincidence with GRBs setting an upper limit on the fluence of 82% of the model after including systematic errors. The limit is plotted in figure 8.2, where the shape of the limit is obtained by adding the individual fluxes from each GRB (figure 5.6) and multiplying by the signal strength limit. The limit is only set between the energies where 5% and 95% of the expected signal events are present: 37 TeV and 2.4 PeV.

8.3 Outlook

The previous best limit was obtained from IceCube's predecessor, AMANDA, from over 400 GRBs which occurred from 1997 to 2003[29] using the Waxman and Bahcall flux[274] as the expected signal. This analysis was able to outperform the AMANDA analysis despite having one quarter fewer bursts than the AMANDA analysis due to IceCube's much larger effective area and better angular resolution. The IceCube detector was completed in December 2010 with a total of 86 strings. Simulations show that the complete IceCube detector is about a factor of 2 more sensitive due to the larger instrumented volume and greater lever arm to reconstruct muons.

The IceCube 22 string analysis, also shown in figure 8.2, was performed on only 44 bursts despite the 22 string configuration operating over a similar real time as this analysis. This analysis had significantly more GRBs because of the launch of the *Fermi* satellite which sees about 250 bursts per year in the entire sky. Although only operating for 2/3 of the real-time of this analysis, almost half of the GRBs in this analysis were observed solely by the GBM, thus it contributed significantly to the limit set. While the GBM's angular resolution is far too large for afterglow follow up studies, it is well suited for neutrino coincidence studies.

In parallel to this analysis a second GRB analysis was performed on the same data by Nathan Whitehorn. This model-independent analysis took a very different approach to the problem, as instead of optimizing on an existing neutrino emission model it sought to maximize acceptance. Instead of looking for neutrinos during and close to the prompt phase of the GRB, the model-independent analysis looked for neutrinos on timescales from 10 seconds to 1 day around the GRB. This was accomplished by starting with an interval of -10 to $+10$ seconds from the trigger time, then expanding the time window by one second increments in both directions to ± 1 day, looking for a significant excess of neutrinos at each iteration. High correlation between adjacent time windows reduces the trials correction to the significance of any excess to only a few hundred.

To ensure that no events were missed due to incorrect assumptions, the model-independent analysis was designed to maximize the number of signal neutrinos in the final analysis instead of the significance of an excess. Instead of being selected by hard cuts, events were weighted by their probabilities of being signal neutrinos[290]. The model-independent analysis was performed on all events which passed the muon filter, which totaled 161 million events. To avoid assuming a signal neutrino spectrum, the model-independent analysis made no attempt to reject the small low-energy background from atmospheric neutrinos. Each probability was the product of the event's point-spread probability density function (equation 7.3) and the probability that the event was a neutrino, determined by dividing smoothed histograms of detector data and neutrino simulation in several variables related to reconstruction accuracy. These probabilities were then summed in each time window to form the expectation of the on-source signal neutrino density, which was then compared to the expected background value obtained by scrambling the observed data in time. Of the events observed, the three most significant occurred at −2249, −3594, and −6430 seconds respectively, and were low energy ($\sim$ 1 TeV) neutrinos consistent with the atmospheric neutrino background.

These model-dependent and model-independent analyses are very complementary to each other. The model-dependent analysis is more sensitive to emission during the prompt phase of the GRB and more sensitive to harder neutrino emission models. While the model-independent is more sensitive to emission on different time scales than the prompt phase and has higher acceptance for lower quality neutrino events. Due to the complimentary nature of these two analyses, we can be confident that between these two analyses no neutrino events were missed. The results of both of theses analyses were published in *Physical Review Letters*[291].

Since the unblinding of this analysis the results of the 59 string GRB analyses have also become available[292]. The model-dependent search which was performed by Peter Redl on the 59 string data was very similar to the analysis presented in this thesis. Nathan Whitehorn repeated his model-independent analysis on the 59 string data as well. Neither of these analyses resulted in a significant observation and set a limit of 26% of the model fluence.

Although this analysis has rejected the neutrino emission model presented in section 2.2 using these specific parameters, neutrino emission from gamma-ray bursts is still far from being ruled out. The parameters used in this analysis were selected because they are consistent with GRBs being the source of UHECR. Every effort has been made to model the neutrino emission as accurately as possible, however, unknown quantities still dominate the calculations. If the GRB rate follows the star formation rate, the peak contribution to the fluence would come from bursts at $z \approx 1$ instead of the average value of $z \approx 2$ as used for most bursts in this analysis, this discrepancy results in a 50% error in the calculated fluence[293]. The uncertainty caused by not knowing the bulk Lorentz factor is even greater. Although observational limits place both upper and lower bounds on Γ, restricting it to a single order of magnitude, see section 2.2, there is no reason to believe that all GRB have the same Γ, or even the same Γ among separate peaks within the same GRB[165, 166]. The neutrino emission model presented here is very sensitive to Γ, since the total emission is proportional to $1/\Gamma^4$. However, more detailed modeling of GRB shocks shows that competing effects cause the neutrino emission to be less sensitive to Γ than the model presented here[293, 294]. The neutrino fluence would also be less sensitive to Γ if bursts are similar in the comoving frame as suggested by recent studies[295].

The ultimate goal of this analysis was to investigate whether GRBs are the source of ultra-high energy cosmic rays. Both Waxman and Bahcall[25, 274] and Guetta *et al.*[156] assume that GRBs are the source of UHECR, however, they differ in how they calculate the expected neutrino flux. Waxman and Bahcall use the cosmic ray spectrum to calculate the total energy while Guetta *et al.* use the energy of the gamma-ray emission. Waxman and Bahcall and Guetta *et al.* were assumed to be in agreement because they predicted similar neutrino spectra. Recent work by Ahlers, Gonzalez-Garcia and Halzen[273] calculates possible neutrino fluxes under the constraints of the observed gamma-ray spectrum and the observed cosmic ray spectrum. Their work finds a smaller area of available parameter space (in the very high Γ region) in which GRBs could be the source of the UHECR than Guetta *et al.* assumed in their work. Further work carried out after the results of the 40 and 59 string data were made publicly available predict lower neutrino fluences than were used in this analysis[154,296,297], although not ruled out by the present limits, these lower fluences are still testable by 10 years of the complete 86 string detector. However, recent studies of the variability time scale of GRBs show that they might be higher than the values used here[298], resulting in higher neutrino fluences. If further generations of IceCube do not observe neutrinos from gamma-ray bursts, then it will become increasingly difficult to explain the observed UHECR flux as the product of GRBs without significantly revising the current models of gamma-ray burst fireballs. If neutrinos are observed they will confirm GRBs as the source of

UHECR and their energy spectrum may be used to further understand the nature of GRBs.

Appendix A

Derivation of Unbinned Likelihood Function

In this appendix, an estimator for the number of signal events and the signal strength will be derived. The estimator derived here will rely on the principal of the maximum likelihood method[299]. In this experiment, the total number of observed events will not be known before the experiment is performed, so it is necessary to use a test statistic which not only estimates the number of signal events, but provides a way to compare results where a different number of events were observed. In general, the likelihood function is the product of many PDFs. For a given data sample $\{x_1, x_2, \ldots, x_N\}$ and a probability of obtaining each data point $p(x; a)$, where a is an unknown parameter, the likelihood is defined as

$$\mathcal{L}(\{x_i\}; a) = p(x_1; a)p(x_2; a) \cdots p(x_N; a) = \prod_{i=1}^{N} p(x_i; a) \tag{A.1}$$

where $\{x_i\}$ is shorthand for $\{x_1, x_2, \ldots, x_N\}$. The estimate for a is denoted as $\hat{a}$ and is the value of a for which the likelihood function is maximized. The probability of observing N events under the assumption that the expected total number of events (n_t) is defined by Poisson statistics:

$$P_{poisson}(N; n_t) = \frac{\mathrm{e}^{-\mathrm{n_t}}\mathrm{n_t^N}}{N!} \tag{A.2}$$

Interpreting this probability as the first probability in the likelihood function's product and the rest of the probabilities in the product as $P(x_i)$, the probability of observing an event with properties x_i. So that the likelihood function of observing N events with properties $\{x_i\}$ becomes:

$$\mathcal{L}(N, \{x_i\}; n_t) = \frac{\mathrm{e}^{-\mathrm{n_t}}\mathrm{n_t^N}}{N!} \times \prod_{i=1}^{N} P(x_i) \tag{A.3}$$

Since the logarithm is a monotonic function, the value which maximizes $\mathcal{L}$ will also maximize $\ln \mathcal{L}$ and it becomes more convenient to work with the logarithm of the likelihood than the likelihood. N can be removed from the arguments because it is the number of elements in $\{x_i\}$.

$$\ln \mathcal{L}(\{x_i\}; n_t) = -n_t - \ln N! + N \ln n_t + \sum_{i=1}^{N} \ln P(x_i) \tag{A.4}$$

The $N \ln n_t$ term can be moved inside the sum.

$$\ln \mathcal{L}(\{x_i\}; n_t) = -n_t - \ln N! + \sum_{i=1}^{N} \ln[n_t P(x_i)] \tag{A.5}$$

Now $P(x)$, the probability of observing an event with observable x, must be determined. The probability of a signal event having observables x, where x can denote one or more observables, is denoted $S(x)$, similarly the probability of a background event having observables x is $B(x)$. Thus, the probability of measuring an event with observables x is $P(x)$:

$$P(x) = p(s)S(x) + p(b)B(x) \tag{A.6}$$

Where $p(s)$ is the probability of measuring a signal event and $p(b)$ is the probability of measuring a background event. These probabilities are:

$$p(s) = \frac{n_s}{n_s + n_b} \qquad p(b) = \frac{n_b}{n_s + n_b} \tag{A.7}$$

when n_s is the number of signal events and n_b is the number of background events such that n_t is

$$n_t = n_s + n_b \tag{A.8}$$

Rearrange equation A.6 to get

$$n_t P(x) = n_s S(x) + n_b B(x) \tag{A.9}$$

Plug equation A.9 into equation A.5, and replace the parameter in the likelihood function n_t with the parameter to be measured, n_s. n_b can be omitted as a parameter because it will be replaced with the expected number of background events, $\langle n_b \rangle$, measured from off-source data.

$$\ln \mathcal{L}(\{x_i\}; n_s) = -n_s - \langle n_b \rangle - \ln N! + \sum_{i=1}^{N} \ln[n_s S(x_i) + \langle n_b \rangle B(x_i)] \tag{A.10}$$

(Contrast this with [278] which replaces n_b with $N - n_s$.) The no signal or null hypothesis of the likelihood can be calculated by setting $n_s = 0$

$$\ln \mathcal{L}_0(\{x_i\}) = \ln \mathcal{L}(\{x_i\}; 0) = -\langle n_b \rangle - \ln N! + \sum_{i=1}^{N} \ln[\langle n_b \rangle B(x_i)] \tag{A.11}$$

Dividing the likelihood by a constant number will not effect the value of the minimum. In this case dividing by the null hypothesis significantly simplifies the form of the function

$$\ln \mathcal{L}_R(\{x_i\}; n_s) = \ln\left(\frac{\mathcal{L}(\{x_i\}; n_s)}{\mathcal{L}_0(\{x_i\})}\right) = -n_s + \sum_{i=1}^{N} \ln\left(\frac{n_s S(x_i)}{\langle n_b \rangle B(x_i)} + 1\right) \tag{A.12}$$

The estimator for the number of signal events, $\hat{n}_s$, is the value of n_s which maximizes $\mathcal{L}_R$

$$\left.\frac{\partial \mathcal{L}_R(\{x_i\}; n_s)}{\partial n_s}\right|_{n_s = \hat{n}_s} = 0 \tag{A.13}$$

Define the test statistic, $\mathcal{T}$, as the value of $\mathcal{L}_R(\{x_i\}; n_s)$ at the maximum.

$$\mathcal{T} = \mathcal{L}_R(\hat{n}_s) \tag{A.14}$$

This function has several properties which make it well suited for estimating the number of signal events in a sample. For notation simplicity, the probability ratio, r_i is defined to be

$$r_i = \frac{S(x_i)}{\langle n_b \rangle B(x_i)} \tag{A.15}$$

If $\{r_i\}$ contains a single event then $\hat{n}_s$ approaches 1 as r_1 goes to ∞ see table A.1. If

$\{r_1\}$	$\hat{n}_s$	$\mathcal{T}$
$\{10^1\}$	0.900000	1.40
$\{10^2\}$	0.990000	3.62
$\{10^3\}$	0.999000	5.91
$\{10^4\}$	0.999900	8.21
$\{10^5\}$	0.999990	10.51
$\{10^6\}$	0.999999	12.82

Table A.1: This table shows the behavior of the likelihood function for experiments which observe one event. As r_1 goes to infinity $\hat{n}_s$ approaches 1 and $\mathcal{T}$ approaches $\ln(r_1) - 1$.

$\{r_i\}$	$\hat{n}_s$	$\mathcal{T}$
$\{10^4\}$	0.9999	8.21
$\{10^4, 10^4\}$	1.9999	17.81
$\{10^4, 10^4, 10^4\}$	2.9999	27.93
$\{10^4, 10^4, 10^4, 10^4\}$	3.9999	38.39
$\{10^4, 10^4, 10^4, 10^4, 10^4\}$	4.9999	49.10
$\{10^4, 10^4, 10^4, 10^4, 10^4, 10^4\}$	5.9999	60.01

Table A.2: This table shows the behavior of the likelihood function for experiments with different number of events. $\hat{n}_s$ approaches the number of events with $r_i \gg 1$.

all members of $\{r_i\}$ are much greater than one, then $\hat{n}_s$ is very close to N where N is the number of observed events, see table A.2. If values of r are added to $\{r_i\}$ which are much less than one, then $\hat{n}_s$ is hardly effected and $\hat{n}_s$ approximately equals the number of values which are much greater than one. If values are added which are on the order of 1 they will smoothly transform $\hat{n}_s$ from one integer to the next integer, see figure A.1. This likelihood function then has precisely the properties which are desired. It will essentially estimate the number of events which have a very high signal to background ratio providing a smooth transition for events with intermediate ratios while simultaneously providing comparable results for experiments where a different number of events were observed.

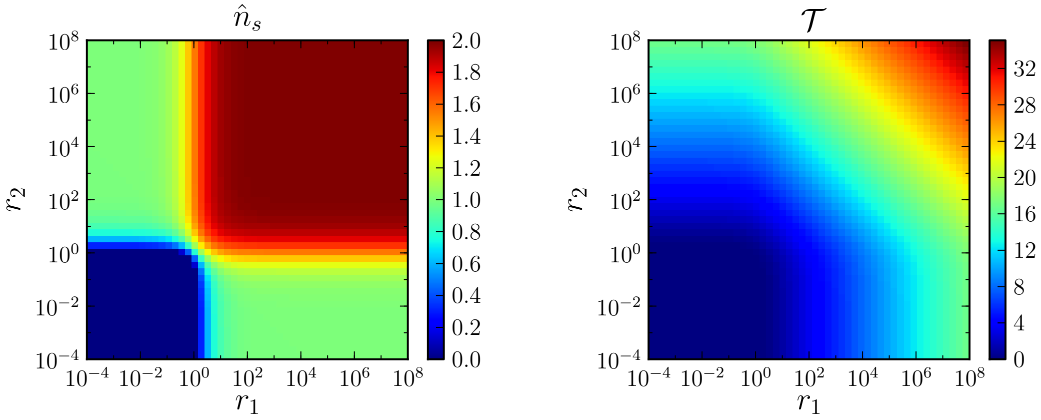

Figure A.1: Color map showing the smooth transition of the likelihood function for an experiment which observes two events, $\{r_i\} = \{r_1, r_2\}$. On the left is $\hat{n}_s$ which is ~ 0 for $r_1, r_2 \ll 1$, ~ 1 for $r_1 \ll 1$ and $r_2 \gg 1$ or $r_1 \gg 1$ and $r_2 \ll 1$, and ~ 2 for $r_1, r_2 \gg 1$ with smooth transitions between each of the regions. On the right is the value of the likelihood at the minimum which is a constant value for $r_1, r_2 \ll 1$ while values in the rest of the region are essentially additive in the $\ln(r_i)$.

Bibliography

[1] K. Koyama *et al.*, "Evidence for Shock Acceleration of High-Energy Electrons in the Supernova Remnant SN1006," *Nature* **378**, 255 (1995).

[2] A. W. Strong, I. V. Moskalenko, and V. S. Ptuskin, "Cosmic-Ray Propagation and Interactions in the Galaxy," *Annu. Rev. Nucl. Part. Sci.* **57**, 285 (2007). `astro-ph/0701517`.

[3] V. S. Ptuskin *et al.*, "Diffusion and Drift of Very High Energy Cosmic Rays in Galactic Magnetic Fields," *Astron. Astrophys.* **268**, 726 (1993).

[4] W. I. Axford, "The Origins of High-Energy Cosmic Rays," *Astrophys. J. Suppl. Ser.* **90**, 937 (1994).

[5] J. W. Cronin, T. K. Gaisser, and S. P. Swordy, "Cosmic Rays at the Energy Frontier," *Sci. Am.* **276**, 44 (Jan. 1997). `http://astroparticle.uchicago.edu/siteold/cosmic_ray_spectrum_picture.htm`.

[6] J. Abraham *et al.* (Pierre Auger Collaboration), "Measurement of the Energy Spectrum of Cosmic Rays Above 10^{18} eV Using the Pierre Auger Observatory," *Phys. Lett. B* **685**, 239 (2010). `arXiv:1002.1975`.

[7] R. U. Abbasi *et al.* (High Resolution Fly's Eye Collaboration), "Measurement of the Flux of Ultra High Energy Cosmic Rays by the Stereo Technique," *Astropart. Phys.* **32**, 53 (2009). `arXiv:0904.4500`.

[8] K. Greisen, "End to the Cosmic-Ray Spectrum?" *Phys. Rev. Lett.* **16**, 748 (1966).

[9] G. T. Zatsepin and V. A. Kuz'min, "Upper Limit of the Spectrum of Cosmic Rays," *Pis'ma Zh. Eksp. Teor. Fiz.* **4**, 114 (1966) [*JETP Lett.* **4**, 78 (1966)].

[10] D. J. Bird *et al.*, "Evidence for Correlated Changes in the Spectrum and Composition of Cosmic Rays at Extremely High Energies," *Phys. Rev. Lett.* **71**, 3401 (1993).

[11] S. Yoshida *et al.*, "The Cosmic Ray Energy Spectrum Above 3×10^{18} eV Measured by the Akeno Giant Air Shower Array," *Astropart. Phys.* **3**, 105 (1995).

[12] R. D. Blandford and J. P. Ostriker, "Particle Acceleration by Astrophysical Shocks," *Astrophys. J.* **221**, L29 (1978).

[13] A. R. Bell, "The Acceleration of Cosmic Rays in Shock Fronts: I," *Mon. Not. R. Astron. Soc.* **182**, 147 (1978).

[14] R. Blandford and D. Eichler, "Particle Acceleration at Astrophysical Shocks: A Theory of Cosmic Ray Origin," *Phys. Rep.* **154**, 1 (1987).

[15] M. S. Longair, *High Energy Astrophysics*, vol. 2, 2$^{\text{nd}}$ ed., Cambridge University Press, 1994, ch. 21.

[16] L. Anchordoqui *et al.*, "Ultrahigh Energy Cosmic Rays: The State of the Art Before the Auger Observatory," *Int. J. Mod. Phys. A* **18**, 2229 (2003). `hep-ph/0206072`. (The figure is from Murat Boratav).

[17] A. M. Hillas, "The Origin of Ultra-High-Energy Cosmic Rays," *Annu. Rev. Astron. Astrophys.* **22**, 425 (1984).

[18] E. Waxman, "Cosmological Gamma-Ray Bursts and the Highest Energy Cosmic Rays," *Phys. Rev. Lett.* **75**, 386 (1995). `astro-ph/9505082`.

[19] M. Vietri, "The Acceleration of Ultra–High-Energy Cosmic Rays in Gamma-Ray Bursts," *Astrophys. J.* **453**, 883 (1995). `astro-ph/9506081`.

[20] M. Bottcher and C. D. Dermer, "High-Energy Gamma Rays from Ultra–High-Energy Cosmic-Ray Protons in Gamma-Ray Bursts," *Astrophys. J.* **499**, L131 (1998). `astro-ph/9801027`.

[21] P. L. Biermann and P. A. Strittmatter, "Synchrotron Emission from Shock Waves in Active Galactic Nuclei," *Astrophys. J.* **322**, 643 (1987).

[22] E. Waxman, "Cosmological Origin for Cosmic Rays above 10^{19} eV," *Astrophys. J.* **452**, L1 (1995). `astro-ph/9508037`.

[23] M. Vietri, D. De Marco, and D. Guetta, "On the Generation of Ultra–High-Energy Cosmic Rays in Gamma-Ray Bursts: A Reappraisal," *Astrophys. J.* **592**, 378 (2003). `astro-ph/0302144`.

[24] E. Waxman, "Gamma-Ray Bursts: Potential Sources of Ultra High Energy Cosmic-Rays," in *Proceedings of the XIII International Symposium on Very High Energy Cosmic Ray Interactions*, edited by P. Grieder, B. Pattison, and L. Resvanis, *Nucl. Phys. B, Proc. Suppl.* **151**, 46 (2006). `astro-ph/0412554`.

[25] E. Waxman and J. Bahcall, "High Energy Neutrinos from Cosmological Gamma-Ray Burst Fireballs," *Phys. Rev. Lett.* **78**, 2292 (1997). `astro-ph/9701231`.

[26] J. P. Rachen and P. Mészáros, "Photohadronic Neutrinos from Transients in Astrophysical Sources," *Phys. Rev. D* **58**, 123005 (1998). `astro-ph/9802280`.

[27] J. P. Rachen and P. Mészáros, "Cosmic Rays and Neutrinos from Gamma-Ray Bursts," in *Fourth Huntsville Gamma-Ray Burst Symposium*, edited by C. A. Meegan, R. D. Preece, and T. M. Koshut, *AIP Conf. Proc.* **428**, 776 (1998). `astro-ph/9811266`.

[28] R. Abbasi *et al.* (IceCube Collaboration), "Search for Muon Neutrinos from Gamma-Ray Bursts with the IceCube Neutrino Telescope," *Astrophys. J.* **710**, 346 (2010). `arXiv:0907.2227`.

[29] A. Achterberg *et al.* (IceCube and IPN Collaborations), "The Search for Muon Neutrinos from Northern Hemisphere Gamma-Ray Bursts with AMANDA," *Astrophys. J.* **674**, 357 (2008). `arXiv:0705.1186`.

[30] R. C. Bay, "Search for High Energy Emission from Gamma-Ray Bursts with the Antarctic Muon and Neutrino Detector Array (AMANDA)," PhD thesis, University of California, Berkeley, 2000. `astro-ph/0008255`.

[31] R. R. Hardtke, "The Search for High Energy Neutrinos from Gamma-Ray Bursts with the AMANDA Detector," PhD thesis, University of Wisconsin–Madison, 2002.

[32] K. W. Kuehn, "The Search for Muon Neutrinos from Northern Hemisphere Gamma-Ray Bursts with AMANDA-II," PhD thesis, University of California, Irvine, 2007.

[33] A. Franckowiak, "Search for Poorly Localized Gamma-Ray Bursts in AMANDA-II Data," diploma thesis, Bergische Universität Wuppertal, Germany, 2007.

[34] E. A. Strahler, "Searches for Neutrinos from Gamma Ray Bursts with the AMANDA-II and IceCube Detectors," PhD thesis, University of Wisconsin–Madison, 2009.

[35] M. Stamatikos, "Probing for Correlated Neutrino Emission from Gamma-Ray Bursts with Antarctic Cherenkov Telescopes: A Theoretical Modeling and Analytical Search Paradigm in the Context of the Fireball Phenomenolgy," PhD thesis, State University of New York at Buffalo, 2006.

[36] R. Abbasi *et al.* (IceCube Collaboration), "Search for High-Energy Muon Neutrinos from the 'Naked-Eye' GRB 080319B with the IceCube Neutrino Telescope," *Astrophys. J.* **701**, 1721 (2009). `arXiv:0902.0131`.

[37] K. Meagher *et al.* for the IceCube Collaboration, "Search for Neutrinos from GRBs with IceCube," in *Proceedings of the 31st International Cosmic Ray Conference*, Łódź, Poland, July 2009, contribution 0515. `arXiv:1004.2093`.

[38] A. P. Roth, "A Search for Muon Neutrinos from Gamma-Ray Bursts with the IceCube 22-String Detector," PhD thesis, University of Maryland, 2009.

[39] M. R. Duvoort, "A Search for Gamma Ray Burst Neutrinos in AMANDA," PhD thesis, Universiteit Utrecht, Netherlands, 2009.

[40] A. Achterberg *et al.* (IceCube Collaboration), "Search for Neutrino-Induced Cascades from Gamma-Ray Bursts with AMANDA," *Astrophys. J.* **664**, 397 (2007). `astro-ph/0702265`.

[41] J. B. Hughey, "Rolling Search for a Cascade GRB Signal," PhD thesis, University of Wisconsin–Madison, 2007.

[42] R. Abbasi *et al.* (IceCube Collaboration), "Searching for Soft Relativistic Jets in Core-Collapse Supernovae with the IceCube Optical Follow-up Program," *Astron. Astrophys.* **539**, A60 (2012). `arXiv:1111.7030`.

[43] A. Franckowiak, "Searching for High-Energy Neutrinos from Supernovae with IceCube and an Optical Follow-up Program," PhD thesis, Rheinische Friedrich-Wilhelms-Universität Bonn, Germany, 2011.

[44] A. Homeier and M. Smith for the IceCube and Swift Collaborations, "SWIFT Follow-up of IceCube Neutrino Multiplets," in *Proceedings of the 32st International Cosmic Ray Conference*, Beijing, 2011, contribution 0535. `arXiv:1111.2741`.

[45] S. Fukuda *et al.* (Super-Kamiokande Collaboration), "Search for Neutrinos from Gamma-Ray Bursts Using Super-Kamiokande," *Astrophys. J.* **578**, 317 (2002). `astro-ph/0205304`.

[46] E. Thrane *et al.* (Super-Kamiokande Collaboration), "Search for Neutrinos from GRB 080319B at Super-Kamiokande," *Astrophys. J.* **697**, 730 (2009). `arXiv:0903.0624`.

[47] E. Thrane *et al.* (Super-Kamiokande Collaboration), "Search for Astrophysical Neutrino Point Sources at Super-Kamiokande," *Astrophys. J.* **704**, 503 (2009). `arXiv:0907.1594`.

[48] A. V. Avrorin *et al.*, "Search for Neutrinos from Gamma-Ray Bursts with the Baikal Neutrino Telescope NT200," *Astron. Lett.* **37**, 692 (2011).

[49] C. Reed, M. Bouwhuis, and E. Presani for the ANTARES Collaboration, "Searches for Neutrinos from GRBs Using the ANTARES Telescope," in *Proceedings of the 32st International Cosmic Ray Conference*, Beijing, 2011, contribution 1085. `arXiv:1112.0478`.

[50] D. Besson *et al.*, "Limits on the Transient Ultra-High Energy Neutrino Flux from Gamma-Ray Bursts (GRB) Derived from RICE data," *Astropart. Phys.* **26**, 367 (2007). `astro-ph/0605480`.

[51] A. G. Vieregg *et al.*, "The First Limits on the Ultra-High Energy Neutrino Fluence from Gamma-Ray Bursts," *Astrophys. J.* **736**, 50 (2011). `arXiv:1102.3206`.

[52] D. Band *et al.*, “BATSE Observations of Gamma-Ray Burst Spectra: I–Spectral diversity,” *Astrophys. J.* **413**, 281 (1993).

[53] M. S. Briggs *et al.*, “Observations of GRB 990123 by the *Compton Gamma Ray Observatory*,” *Astrophys. J.* **524**, 82 (1999). `astro-ph/9903247`.

[54] W. S. Paciesas *et al.*, “The Fourth BATSE Gamma-Ray Burst Catalog (Revised),” *Astrophys. J. Suppl. Ser.* **122**, 465 (1999). `astro-ph/9903205`.

[55] G. J. Fishman and C. A. Meegan, “Gamma-Ray Bursts,” *Annu. Rev. Astron. Astrophys.* **33**, 415 (1995).

[56] NASA, “BATSE: Burst and Transient Source Experiment,” Website. `http://www.batse.msfc.nasa.gov/batse/`.

[57] D. A. Kann, S. Klose, and A. Zeh, “Signatures of Extragalactic Dust in Pre-*Swift* GRB Afterglows,” *Astrophys. J.* **641**, 993 (2006). `astro-ph/0512575`.

[58] B. Zhang *et al.*, “Physical Processes Shaping Gamma-Ray Burst X-Ray Afterglow Light Curves: Theoretical Implications from the *Swift* X-Ray Telescope Observations,” *Astrophys. J.* **642**, 354 (2006). `astro-ph/0508321`.

[59] NASA, “The Vela-5B Satellite,” Website. `http://heasarc.gsfc.nasa.gov/docs/vela5b/vela5b_about.html`.

[60] R. W. Klebesadel, I. B. Strong, and R. A. Olson, “Observations of Gamma-Ray Bursts of Cosmic Origin,” *Astrophys. J.* **182**, L85 (1973).

[61] W. A. Wheaton *et al.*, “The Direction and Spectral Variability of a Cosmic Gamma-Ray Burst,” *Astrophys. J.* **185**, L57 (1973).

[62] T. L. Cline *et al.*, “Energy Spectra of Cosmic Gamma-Ray Bursts,” *Astrophys. J.* **185**, L1 (1973).

[63] C. A. Meegan *et al.*, “Spatial Distribution of γ-Ray Bursts Observed by BATSE,” *Nature* **355**, 143 (1992).

[64] C. Kouveliotou *et al.*, “Identification of Two Classes of Gamma-Ray Bursts,” *Astrophys. J.* **413**, L101 (1993).

[65] G. Kanbach *et al.*, “The Project EGRET (Eergetic Gamma-Ray Experiment Telescope) on NASA’s Gamma-Ray Observatory (GRO),” *Space Sci. Rev.* **49**, 69 (1988).

[66] J. R. Catelli, B. L. Dingus, and E. J. Schneid, “EGRET Observations of Bursts at MeV Energies,” in *Fourth Huntsville Gamma-Ray Burst Symposium*, edited by C. A. Meegan, R. D. Preece, and T. M. Koshut, *AIP Conf. Proc.* **428**, 309 (1998).

[67] K. Hurley *et al.*, "Detection of a γ-Ray Burst of Very Long Duration and Very High Energy," *Nature* **372**, 652 (1994).

[68] M. M. González *et al.*, "A γ-Ray Burst with a High-Energy Spectral Component Inconsistent with the Synchrotron Shock Model," *Nature* **424**, 749 (2003).

[69] R. Atkins *et al.* (Milagro Collaboration), "Milagrito, a TeV Air-Shower Array," *Nucl. Instrum. Meth. A* **449**, 478 (2000). `astro-ph/9912456`.

[70] R. Atkins *et al.* (Milagro Collaboration), "Evidence for TeV Emission from GRB 970417A," *Astrophys. J.* **533**, L119 (2000).

[71] R. Atkins *et al.* (Milagro Collaboration), "The High-Energy Gamma-Ray Fluence and Energy Spectrum of GRB 970417A from Observations with Milagrito," *Astrophys. J.* **583**, 824 (2003). `astro-ph/0207149`.

[72] R. Atkins *et al.* (Milagro Collaboration), "Limits on Very High Energy Emission from Gamma-Ray Bursts with the Milagro Observatory," *Astrophys. J.* **604**, L25 (2004). `astro-ph/0311389`.

[73] R. Atkins *et al.* (Milagro Collaboration), "Constraints on Very High Energy Gamma-Ray Emission from Gamma-Ray Bursts," *Astrophys. J.* **630**, 996 (2005). `astro-ph/0503270`.

[74] A. A. Abdo *et al.* (Milagro Collaboration), "Milagro Constraints on Very High Energy Emission from Short-Duration Gamma-Ray Bursts," *Astrophys. J.* **666**, 361 (2007). `arXiv:0705.1554`.

[75] G. Boella *et al.*, "BeppoSAX, the Wide Band Mission for X-Ray Astronomy," *Astron. Astrophys. Suppl. Ser.* **122**, 299 (1997).

[76] E. Costa *et al.*, "Discovery of an X-Ray Afterglow Associated with the γ-Ray Burst of 28 February 1997," *Nature* **387**, 783 (1997). `astro-ph/9706065`.

[77] M. R. Metzger *et al.*, "Spectral Constraints on the Redshift of the Optical Counterpart to the γ-Ray Burst of 8 May 1997," *Nature* **387**, 878 (1997).

[78] J. P. Halpern *et al.*, "Optical Afterglow of the γ-Ray Burst of 14 December 1997," *Nature* **393**, 41 (1998).

[79] A. N. Ramaprakash *et al.*, "The Energetic Afterglow of the γ-Ray Burst of 14 December 1997," *Nature* **393**, 43 (1998).

[80] N. Kawai *et al.*, "An Optical Spectrum of the Afterglow of a γ-Ray Burst at a Redshift of z = 6.295," *Nature* **440**, 184 (2006).

[81] J. Greiner *et al.*, "GRB 080913 at Redshift 6.7," *Astrophys. J.* **693**, 1610 (2009). `arXiv:0810.2314`.

[82] N. R. Tanvir *et al.*, "A γ-Ray Burst at a Redshift of z $\approx$ 8.2," *Nature* **461**, 1254 (2009). `arXiv:0906.1577`.

[83] R. Salvaterra *et al.*, "GRB090423 at a Redshift of z $\approx$ 8.1," *Nature* **461**, 1258 (2009). `arXiv:0906.1578`.

[84] N. Gehrels *et al.*, "A Short γ-Ray Burst Apparently Associated with an Elliptical Galaxy at Redshift z = 0.225," *Nature* **437**, 851 (2005). `astro-ph/0505630`.

[85] A. A. Abdo *et al.* (*Fermi* LAT and GBM Collaborations), "*Fermi* Observations of High-Energy Gamma-Ray Emission from GRB 080916C," *Science* **323**, 1688 (2009).

[86] M. Ackermann *et al.* (*Fermi* LAT and GBM Collaborations), "*Fermi* Observations of GRB 090510: A Short-Hard Gamma-Ray Burst with an Additional, Hard Power-Law Component from 10 keV to GeV Energies," *Astrophys. J.* **716**, 1178 (2010). `arXiv:1005.2141`.

[87] A. A. Abdo *et al.* (*Fermi* LAT and GBM Collaborations), "*Fermi* Observations of GRB 090902B: A Distinct Spectral Component in the Prompt and Delayed Emission," *Astrophys. J.* **706**, L138 (2009). `arXiv:0909.2470`.

[88] M. Ackermann *et al.* (*Fermi* LAT and GBM Collaborations), "Detection of a Spectral Break in the Extra Hard Component of GRB 090926A," *Astrophys. J.* **729**, 114 (2011). `arXiv:1101.2082`.

[89] E. Waxman, "Gamma-Ray Bursts: The Underlying Model," in *Supernovae and Gamma-Ray Bursters*, edited by K. Weiler, *Lect. Notes Phys.* **598**, 393 (2003). `astro-ph/0303517`.

[90] T. Piran, "The Physics of Gamma-Ray Bursts," *Rev. Mod. Phys.* **76**, 1143 (2004). `astro-ph/0405503`.

[91] B. Zhang and P. Mészáros, "Gamma-Ray Bursts: Progress, Problems & Prospects," *Int. J. Mod. Phys. A* **19**, 2385 (2004). `astro-ph/0311321`.

[92] P. Mészáros, "Gamma-Ray Bursts," *Rep. Prog. Phys.* **69**, 2259 (2006). `astro-ph/0605208`.

[93] B. Zhang, "Gamma-Ray Bursts in the *Swift* Era," *Chinese J. Astron. Astrophys.* **7**, 1 (2007). `astro-ph/0701520`.

[94] G. Vedrenne and J.-L. Atteia, *Gamma-Ray Bursts: The Brightest Explosions in the Universe*, Springer, Berlin, 2009.

[95] S. E. Woosley, "Gamma-Ray Bursts from Stellar Mass Accretion Disks Around Black Holes," *Astrophys. J.* **405**, 273 (1993).

[96] B. Paczynski, "Are Gamma-Ray Bursts in Star-Forming Regions?" *Astrophys. J.* **494**, L45 (1998). `astro-ph/9710086`.

[97] D. Eichler *et al.*, "Nucleosynthesis, Neutrino Bursts and γ-Rays from Coalescing Neutron Stars," *Nature* **340**, 126 (1989).

[98] T. A. Thompson, P. Chang, and E. Quataert, "Magnetar Spin-Down, Hyperenergetic Supernovae, and Gamma-Ray Bursts," *Astrophys. J.* **611**, 380 (2004). `astro-ph/0401555`.

[99] B. Paczynski, "Super-Eddington Winds from Neutron Stars," *Astrophys. J.* **363**, 218 (1990).

[100] J. Goodman, "Are Gamma-Ray Bursts Optically Thick?" *Astrophys. J.* **308**, L47 (1986).

[101] B. Paczynski, "Gamma-Ray Bursters at Cosmological Distances," *Astrophys. J.* **308**, L43 (1986).

[102] M. J. Rees and P. Mészáros, "Relativistic Fireballs: Energy Conversion and Time-Scales," *Mon. Not. R. Astron. Soc.* **258**, 41P (1992).

[103] M. J. Rees and P. Mészáros, "Unsteady Outflow Models for Cosmological Gamma-Ray Bursts," *Astrophys. J.* **430**, L93 (1994). `astro-ph/9404038`.

[104] B. Paczynski and G. Xu, "Neutrino Bursts from Gamma-Ray Bursts," *Astrophys. J.* **427**, 708 (1994).

[105] R. Sari, R. Narayan, and T. Piran, "Cooling Timescales and Temporal Structure of Gamma-Ray Bursts," *Astrophys. J.* **473**, 204 (1996). `astro-ph/9605005`.

[106] E. Waxman, "γ-Ray Burst Afterglow: Confirming the Cosmological Fireball Model," *Astrophys. J.* **489**, L33 (1997). `astro-ph/9705229`.

[107] D. L. Freedman and E. Waxman, "On the Energy of Gamma-Ray Bursts," *Astrophys. J.* **547**, 922 (2001). `astro-ph/9912214`.

[108] A. M. Bykov and P. Mészáros, "Electron Acceleration and Efficiency in Nonthermal Gamma-Ray Sources," *Astrophys. J.* **461**, L37 (1996). `astro-ph/9602016`.

[109] G. Ghisellini, "Gamma Ray Bursts: Basic Facts and Ideas," in *Jets at all Scales*, edited by G. E. Romero, R. A. Sunyaev, and T. Belloni, *Proc. IAU* **6** (S275), 335 (2011). `arXiv:1010.3015`.

[110] S. Kobayashi, T. Piran, and R. Sari, "Can Internal Shocks Produce the Variability in Gamma-Ray Bursts?" *Astrophys. J.* **490**, 92 (1997). `astro-ph/9705013`.

[111] S. Kobayashi, F. Ryde, and A. MacFadyen, “Luminosity and Variability of Collimated Gamma-Ray Bursts,” *Astrophys. J.* **577**, 302 (2002). `astro-ph/0110080`.

[112] P. N. Bhat *et al.*, “Evidence of Sub-Millisecond Structure in a γ-Ray Burst,” *Nature* **359**, 217 (1992).

[113] M. Ruderman, “Theories of γ-Ray Bursts,” in *Seventh Texas Symposium on Relativistic Astrophysics*, edited by P. G. Bergman, E. J. Fenyves, and L. Motz, *Ann. NY Acad. Sci.* **262**, 164 (1975).

[114] J. H. Krolik and E. A. Pier, “Relativistic Motion in Gamma-Ray Bursts,” *Astrophys. J.* **373**, 277 (1991).

[115] T. J. Galama *et al.*, “An Unusual Supernova in the Error Box of the γ-Ray Burst of 25 April 1998,” *Nature* **395**, 670 (1998). `astro-ph/9806175`.

[116] K. Z. Stanek *et al.*, “Spectroscopic Discovery of the Supernova 2003dh Associated with GRB 030329,” *Astrophys. J.* **591**, L17 (2003). `astro-ph/0304173`.

[117] K. Z. Stanek *et al.*, “Protecting Life in the Milky Way: Metals Keep the GRBs Away,” *Acta Astron.* **56**, 333 (2006). `astro-ph/0604113`.

[118] W. H. Lee, E. Ramirez-Ruiz, and D. Page, “Opaque or Transparent? A Link between Neutrino Optical Depths and the Characteristic Duration of Short Gamma-Ray Bursts,” *Astrophys. J.* **608**, L5 (2004). `astro-ph/0404566`.

[119] D. A. Frail *et al.*, “The Radio Afterglow from the γ-Ray Burst of 8 May 1997,” *Nature* **389**, 261 (1997).

[120] J. Goodman, “Radio Scintillation of Gamma-Ray-Burst Afterglows,” *New Astron.* **2**, 449 (1997). `astro-ph/9706084`.

[121] E. Waxman, S. R. Kulkarni, and D. A. Frail, “Implications of the Radio Afterglow from the Gamma-Ray Burst of 1997 May 8,” *Astrophys. J.* **497**, 288 (1998). `astro-ph/9709199`.

[122] G. B. Taylor *et al.*, “The Angular Size and Proper Motion of the Afterglow of GRB 030329,” *Astrophys. J.* **609**, L1 (2004). `astro-ph/0405300`.

[123] R. Sari and T. Piran, “GRB 990123: The Optical Flash and the Fireball Model,” *Astrophys. J.* **517**, L109 (1999). `astro-ph/9902009`.

[124] B. Zhang, S. Kobayashi, and P. Mészáros, “Gamma-Ray Burst Early Optical Afterglows: Implications for the Initial Lorentz Factor and the Central Engine,” *Astrophys. J.* **595**, 950 (2003). `astro-ph/0302525`.

[125] A. M. Soderberg and E. Ramirez-Ruiz, "Constraints on the Bulk Lorentz Factor of GRB 990123," in *Gamma-Ray Burst and Afterglow Astronomy 2001: A Workshop Celebrating the First Year of the HETE Mission*, edited by G. R. Ricker and R. K. Vanderspek, *AIP Conf. Proc.* **662**, 172 (2003). `astro-ph/0203241`.

[126] E. Molinari *et al.*, "REM Observations of GRB 060418 and GRB 060607A: The Onset of the Afterglow and the Initial Fireball Lorentz Factor Determination," *Astron. Astrophys.* **469**, L13 (2007). `astro-ph/0612607`.

[127] J. L. Racusin *et al.*, "Broadband Observations of the Naked-Eye γ-Ray Burst GRB080319B," *Nature* **455**, 183 (2008). `arXiv:0805.1557`.

[128] R. Xue, Y. Fan, and D. Wei, "The Initial Lorentz Factors of Fireballs Inferred from the Early X-Ray Data of *Swift* GRBs," *Astron. Astrophys.* **498**, 671 (2009). `arXiv:0902.2613`.

[129] E.-W. Liang *et al.*, "Constraining Gamma-Ray Burst Initial Lorentz Factor with the Afterglow Onset Feature and Discovery of a Tight $\Gamma_0 - E_{\gamma,iso}$ Correlation," *Astrophys. J.* **725**, 2209 (2010). `arXiv:0912.4800`.

[130] D. Gruber *et al.*, "*Fermi*/GBM Observations of the Ultra-Long GRB 091024: A Burst with an Optical Flash," *Astron. Astrophys.* **528**, A15 (2011). `arXiv:1101.1099`.

[131] A. Pe'er *et al.*, "A New Method of Determining the Initial Size and Lorentz Factor of Gamma-Ray Burst Fireballs Using a Thermal Emission Component," *Astrophys. J.* **664**, L1 (2007). `astro-ph/0703734`.

[132] F. Ryde *et al.*, "Identification and Properties of the Photospheric Emission in GRB090902B," *Astrophys. J.* **709**, L172 (2010). `arXiv:0911.2025`.

[133] A. K. Harding and M. G. Baring, "Escape of High-Energy Photons from Relativistically Expanding Gamma-Ray Burst Sources," in *Gamma-ray Bursts: Second Workshop*, edited by G. J. Fishman, J. J. Brainerd, and K. Hurley, *AIP Conf. Proc.* **307**, 520 (1994).

[134] P. Mészáros, "Gamma-Ray Burst Models: General Requirements and Predictions," in *Seventeeth Texas Symposium on Relativistic Astrophysics and Cosmology*, edited by H. Böhringer, G. E. Morfill, and J. E. Trümper, *Ann. NY Acad. Sci.* **759**, 440 (1995). `astro-ph/9502090`.

[135] E. E. Fenimore, R. I. Epstein, and C. Ho, "The Escape of 100 MeV Photons from Cosmological Gamma-Ray Bursts," *Astron. Astrophys. Suppl. Ser.* **97**, 59 (1993).

[136] E. Woods and A. Loeb, "Empirical Constraints on Source Properties and Host Galaxies of Cosmological Gamma-Ray Bursts," *Astrophys. J.* **453**, 583 (1995). `astro-ph/9503070`.

[137] M. G. Baring and A. K. Harding, "The Escape of High-Energy Photons from Gamma-Ray Bursts," *Astrophys. J.* **491**, 663 (1997). `astro-ph/9711217`.

[138] Y. Lithwick and R. Sari, "Lower Limits on Lorentz Factors in Gamma-Ray Bursts," *Astrophys. J.* **555**, 540 (2001). `astro-ph/0011508`.

[139] J. Granot, J. Cohen-Tanugi, and E. do Couto e Silva, "Opacity Buildup in Impulsive Relativistic Sources," *Astrophys. J.* **677**, 92 (2008). `arXiv:0708.4228`.

[140] D. Lazzati, G. Ghisellini, and A. Celotti, "Constraints on the Bulk Lorentz Factor in the Internal Shock Scenario for Gamma-Ray Bursts," *Mon. Not. R. Astron. Soc.* **309**, L13 (1999). `astro-ph/9907070`.

[141] E. Ramirez-Ruiz and E. E. Fenimore, "Pulse Width Evolution in Gamma-Ray Bursts: Evidence for Internal Shocks," *Astrophys. J.* **539**, 712 (2000). `astro-ph/9910273`.

[142] P. Mészáros, P. Laguna, and M. J. Rees, "Gasdynamics of Relativistically Expanding Gamma-Ray Burst Sources: Kinematics, Energetics, Magnetic Fields, and Efficiency," *Astrophys. J.* **415**, 181 (1993). `astro-ph/9301007`.

[143] J. E. Rhoads, "The Dynamics and Light Curves of Beamed Gamma-Ray Burst Afterglows," *Astrophys. J.* **525**, 737 (1999). `astro-ph/9903399`.

[144] D. A. Frail *et al.*, "Beaming in Gamma-Ray Bursts: Evidence for a Standard Energy Reservoir," *Astrophys. J.* **562**, L55 (2001). `astro-ph/0102282`.

[145] N. Wygoda, E. Waxman, and D. A. Frail, "Relativistic Jet Dynamics and Calorimetry of Gamma-ray Bursts," *Astrophys. J.* **738**, L23 (2011). `arXiv:1102.5618`.

[146] R. Sari, T. Piran, and J. P. Halpern, "Jets in Gamma-Ray Bursts," *Astrophys. J.* **519**, L17 (1999). `astro-ph/9903339`.

[147] F. A. Harrison *et al.*, "Optical and Radio Observations of the Afterglow from GRB 990510: Evidence for a Jet," *Astrophys. J.* **523**, L121 (1999). `astro-ph/9905306`.

[148] J. S. Bloom, D. A. Frail, and S. R. Kulkarni, "Gamma-Ray Burst Energetics and the Gamma-Ray Burst Hubble Diagram: Promises and Limitations," *Astrophys. J.* **594**, 674 (2003). `astro-ph/0302210`.

[149] R. Popham, S. E. Woosley, and C. Fryer, "Hyperaccreting Black Holes and Gamma-Ray Bursts," *Astrophys. J.* **518**, 356 (1999). `astro-ph/9807028`.

[150] P. Mészáros and M. J. Rees, "Poynting Jets from Black Holes and Cosmological Gamma-Ray Bursts," *Astrophys. J.* **482**, L29 (1997). `astro-ph/9609065`.

[151] E. Waxman and J. Bahcall, "High Energy Neutrinos from Astrophysical Sources: An Upper Bound," *Phys. Rev. D* **59**, 023002 (1999). `hep-ph/9807282`.

[152] K. Asano, "Cooling of Accelerated Nucleons and Neutrino Emission in Gamma-Ray Bursts," *Astrophys. J.* **623**, 967 (2005). `astro-ph/0503262`.

[153] K. Murase and S. Nagataki, "High Energy Neutrino Emission and Neutrino Background from Gamma-Ray Bursts in the Internal Shock Model," *Phys. Rev. D* **73**, 063002 (2006). `astro-ph/0512275`.

[154] S. Hümmer, P. Baerwald, and W. Winter, "Neutrino Emission from Gamma-Ray Burst Fireballs, Revised," ArXiv e-print, 2011. `arXiv:1112.1076`.

[155] W. Winter, "Neutrinos from Cosmic Accelerators Including Magnetic Field and Flavor Effects," ArXiv e-print, 2012. `arXiv:1201.5462`.

[156] D. Guetta *et al.*, "Neutrinos from Individual Gamma-Ray Bursts in the BATSE Catalog," *Astropart. Phys.* **20**, 429 (2004). `astro-ph/0302524`.

[157] J. Bahcall and E. Waxman, "High Energy Astrophysical Neutrinos: The Upper Bound is Robust," *Phys. Rev. D* **64**, 023002 (2001). `hep-ph/9902383`.

[158] K. Asano and S. Nagataki, "Very High Energy Neutrinos Originating from Kaons in Gamma-Ray Bursts," *Astrophys. J.* **640**, L9 (2006). `astro-ph/0603107`.

[159] P. Baerwald, S. Hümmer, and W. Winter, "Magnetic Field and Flavor Effects on the Gamma-Ray Burst Neutrino Flux," *Phys. Rev. D* **83**, 067303 (2011). `arXiv:1009.4010`.

[160] H. B. J. Koers and R. A. M. J. Wijers, "Enhanced High-Energy Neutrino Emission from Choked Gamma-Ray Bursts Due to Meson and Muon Acceleration," ArXiv e-print, 2007. `arXiv:0711.4791`.

[161] F. Halzen and D. Hooper, "High-Energy Neutrino Astronomy: The Cosmic Ray Connection," *Rep. Prog. Phys.* **65**, 1025 (2002). `astro-ph/0204527`.

[162] J. G. Learned and S. Pakvasa, "Detecting ν_τ Oscillations at PeV Energies," *Astropart. Phys.* **3**, 267 (1995). `hep-ph/9405296`.

[163] H. Athar, C. S. Kim, and J. Lee, "Intrinsic and Oscillated Astrophysical Neutrino Flavor Ratios Revisited," *Mod. Phys. Lett. A* **21**, 1049 (2006). `hep-ph/0505017`.

[164] T. Kashti and E. Waxman, "Astrophysical Neutrinos: Flavor Ratios Depend on Energy," *Phys. Rev. Lett.* **95**, 181101 (2005). `astro-ph/0507599`.

[165] F. Halzen and D. W. Hooper, "Neutrino Event Rates from Gamma-Ray Bursts," *Astrophys. J.* **527**, L93 (1999). `astro-ph/9908138`.

[166] J. Alvarez-Muñiz, F. Halzen, and D. W. Hooper, "High Energy Neutrinos from Gamma Ray Bursts: Event Rates in Neutrino Telescopes," *Phys. Rev. D* **62**, 093015 (2000). `astro-ph/0006027`.

[167] V. V. Usov, "On the Nature of Nonthermal Radiation from Cosmological Gamma-Ray Bursters," *Mon. Not. R. Astron. Soc.* **267**, 1035 (1994). `astro-ph/9312024`.

[168] C. Thompson, "A Model of Gamma-Ray Bursts," *Mon. Not. R. Astron. Soc.* **270**, 480 (1994).

[169] M. Lyutikov and R. Blandford, "Gamma Ray Bursts as Electromagnetic Outflows," ArXiv e-print, 2003. `astro-ph/0312347`.

[170] P. Mészáros and M. J. Rees, "Multi-GEV Neutrinos from Internal Dissipation in Gamma-Ray Burst Fireballs," *Astrophys. J.* **541**, L5 (2000). `astro-ph/0007102`.

[171] S. Razzaque, P. Mészáros, and E. Waxman, "Neutrino Tomography of Gamma Ray Bursts and Massive Stellar Collapses," *Phys. Rev. D* **68**, 083001 (2003). `astro-ph/0303505`.

[172] P. Mészáros and E. Waxman, "TeV Neutrinos from Successful and Choked Gamma-Ray Bursts," *Phys. Rev. Lett.* **87**, 171102 (2001). `astro-ph/0103275`.

[173] J. N. Bahcall and P. Mészáros, "5–10 GeV Neutrinos from Gamma-Ray Burst Fireballs," *Phys. Rev. Lett.* **85**, 1362 (2000). `hep-ph/0004019`.

[174] M. Vietri, "Ultrahigh Energy Neutrinos from Gamma Ray Bursts," *Phys. Rev. Lett.* **80**, 3690 (1998). `astro-ph/9802241`.

[175] E. Waxman and J. N. Bahcall, "Neutrino Afterglow from Gamma-Ray Bursts: $\sim 10^{18}$ eV," *Astrophys. J.* **541**, 707 (2000). `hep-ph/9909286`.

[176] K. Murase, "High Energy Neutrino Early Afterglows from Gamma-Ray Bursts Revisited," *Phys. Rev. D* **76**, 123001 (2007). `arXiv:0707.1140`.

[177] K. Murase and S. Nagataki, "High Energy Neutrino Flashes from Far-Ultraviolet and X-Ray Flares in Gamma-Ray Bursts," *Phys. Rev. Lett.* **97**, 051101 (2006). `astro-ph/0604437`.

[178] K. Murase, "Prompt High-Energy Neutrinos from Gamma-Ray Bursts in Photospheric and Synchrotron Self-Compton Scenarios," *Phys. Rev. D* **78**, 101302 (2008). `arXiv:0807.0919`.

[179] X.-Y. Wang and Z.-G. Dai, "Prompt TeV Neutrinos from the Dissipative Photospheres of Gamma-Ray Bursts," *Astrophys. J.* **691**, L67 (2009). `arXiv:0807.0290`.

[180] S. Razzaque, P. Mészáros, and E. Waxman, "High Energy Neutrinos from Gamma-Ray Bursts with Precursor Supernovae," *Phys. Rev. Lett.* **90**, 241103 (2003). `astro-ph/0212536`.

[181] C. D. Dermer and A. Atoyan, "High-Energy Neutrinos from Gamma Ray Bursts," *Phys. Rev. Lett.* **91**, 071102 (2003). `astro-ph/0301030`.

[182] S. Razzaque, P. Mészáros, and E. Waxman, "TeV Neutrinos from Core Collapse Supernovae and Hypernovae," *Phys. Rev. Lett.* **93**, 181101 (2004). `astro-ph/0407064`.

[183] S. Razzaque, P. Mészáros, and E. Waxman, "Neutrino Signatures of the Supernova: Gamma Ray Burst Relationship," *Phys. Rev. D* **69**, 023001 (2004). `astro-ph/0308239`.

[184] NASA, "GCN: The Gamma-Ray Bursts Coordinates Network," Website. `http://gcn.gsfc.nasa.gov/`.

[185] N. Gehrels *et al.*, "The *Swift* Gamma-Ray Burst Mission," *Astrophys. J.* **611**, 1005 (2004).

[186] S. D. Barthelmy *et al.*, "The Burst Alert Telescope (BAT) on the *Swift* Midex Mission," *Space Sci. Rev.* **120**, 143 (2005). `astro-ph/0507410`.

[187] D. N. Burrows *et al.*, "The *Swift* X-Ray Telescope," *Space Sci. Rev.* **120**, 165 (2005). `astro-ph/0508071`.

[188] P. W. A. Roming *et al.*, "The *Swift* Ultra-Violet/Optical Telescope," *Space Sci. Rev.* **120**, 95 (2005). `astro-ph/0507413`.

[189] W. B. Atwood *et al.* (*Fermi* LAT Collaboration), "The Large Area Telescope on the *Fermi Gamma-Ray Space Telescope* Mission," *Astrophys. J.* **697**, 1071 (2009). `arXiv:0902.1089`.

[190] C. Meegan *et al.*, "The *Fermi* Gamma-ray Burst Monitor," *Astrophys. J.* **702**, 791 (2009). `arXiv:0908.0450`.

[191] C. Winkler *et al.*, "The INTEGRAL Mission," *Astron. Astrophys.* **411**, L1 (2003).

[192] S. Mereghetti *et al.*, "The INTEGRAL Burst Alert System," *Astron. Astrophys.* **411**, L291 (2003). `astro-ph/0308173`.

[193] A. von Kienlin *et al.*, "INTEGRAL Spectrometer SPI's GRB Detection Capabilities: GRBs Detected Inside SPI's FoV and with the Anticoincidence System ACS," *Astron. Astrophys.* **411**, L299 (2003). `astro-ph/0308346`.

[194] M. Feroci *et al.*, “SuperAGILE: The Hard X-Ray Imager for the AGILE Space Mission,” *Nucl. Instrum. Meth. A* **581**, 728 (2007). `arXiv:0708.0123`.

[195] R. L. Aptekar *et al.*, “Konus-W Gamma-Ray Burst Experiment for the GGS Wind Spacecraft,” *Space Sci. Rev.* **71**, 265 (1995).

[196] T. Takahashi *et al.*, “Hard X-Ray Detector (HXD) on Board Suzaku,” *Publ. Astron. Soc. Japan* **59**, 35 (2007). `astro-ph/0611232`.

[197] K. Yamaoka *et al.*, “Design and In-Orbit Performance of the Suzaku Wide-Band All-Sky Monitor,” *Publ. Astron. Soc. Japan* **61**, 35 (2009).

[198] K. Hurley *et al.*, “The Third Interplanetary Network,” in *Deciphering the Ancient Universe with Gamma-Ray Bursts*, edited by N. Kawai and S. Nagataki, *AIP Conf. Proc.* **1279**, 330 (2010).

[199] T. K. Gaisser, F. Halzen, and T. Stanev, “Particle Astrophysics With High Energy Neutrinos,” *Phys. Rep.* **258**, 173 (1995). `hep-ph/9410384`.

[200] J. G. Learned and K. Mannheim, “High-Energy Neutrino Astrophysics,” *Annu. Rev. Nucl. Part. Sci.* **50**, 679 (2000).

[201] P. Lipari and T. Stanev, “Propagation of Multi-TeV Muons,” *Phys. Rev. D* **44**, 3543 (1991).

[202] J. Ahrens *et al.* (IceCube Collaboration), “Sensitivity of the IceCube Detector to Astrophysical Sources of High Energy Muon Neutrinos,” *Astropart. Phys.* **20**, 507 (2004). `astro-ph/0305196`.

[203] F. Halzen and S. R. Klein, “IceCube: An Instrument For Neutrino Astronomy,” *Rev. Sci. Instrum.* **81**, 081101 (2010). `arXiv:1007.1247`.

[204] M. Ackermann *et al.* (IceCube Collaboration), “Optical Properties of Deep Glacial Ice at the South Pole,” *J. Geophys. Res.* **111**, D13203 (2006).

[205] R. Abbasi *et al.* (IceCube Collaboration), “The Design and Performance of IceCube DeepCore,” *Astropart. Phys.* **35**, 615 (2012). `arXiv:1109.6096`.

[206] E. Andrés *et al.* (AMANDA Collaboration), “The AMANDA Neutrino Telescope: Principle of Operation and First Results,” *Astropart. Phys.* **13**, 1 (2000). `astro-ph/9906203`.

[207] E. Andrés *et al.*, “Observation of High-Energy Neutrinos Using Čerenkov Detectors Embedded Deep in Antarctic ice,” *Nature* **410**, 441 (2001).

[208] R. Abbasi *et al.*, “Measurement of the Atmospheric Neutrino Energy Spectrum from 100 GeV to 400 TeV with IceCube,” *Phys. Rev. D* **83**, 012001 (2011). `arXiv:1010.3980`.

[209] K. Woschnagg, "Geometry Figures," IceCube Internal Wiki. `http://wiki.icecube.wisc.edu/index.php/Geometry_figures`.

[210] R. Abbasi *et al.* (IceCube Collaboration), "Calibration and Characterization of the IceCube Photomultiplier Tube," *Nucl. Instrum. Meth. A* **618**, 139 (2010). `arXiv:1002.2442`.

[211] A. Achterberg *et al.* (IceCube Collaboration), "First Year Performance of the IceCube Neutrino Telescope," *Astropart. Phys.* **26**, 155 (2006). `astro-ph/0604450`.

[212] R. Abbasi *et al.* (IceCube Collaboration), "The IceCube Data Acquisition System: Signal Capture, Digitization, and Timestamping," *Nucl. Instrum. Meth. A* **601**, 294 (2009). `arXiv:0810.4930`.

[213] D. Heck *et al.*, "CORSIKA: A Monte Carlo Code to Simulate Extensive Air Showers," Tech. Rep. FZKA 6019, Forschungszentrum Karlsruhe, Germany, 1998, p. 90.

[214] J. R. Hörandel, "On the Knee in the Energy Spectrum of Cosmic Rays," *Astropart. Phys.* **19**, 193 (2003). `astro-ph/0210453`.

[215] S. V. Ter-Antonyan and L. S. Haroyan, "About EAS Size Spectra and Primary Energy Spectra in the Knee Region," ArXiv e-print, 2000. `hep-ex/0003006`.

[216] A. Gazizov and M. Kowalski, "ANIS: High Energy Neutrino Generator for Neutrino Telescopes," *Comput. Phys. Commun.* **172**, 203 (2005). `astro-ph/0406439`.

[217] H. L. Lai *et al.*, "Global QCD Analysis of Parton Structure of the Nucleon: CTEQ5 Parton Distributions," *Eur. Phys. J. C* **12**, 375 (2000). `hep-ph/9903282`.

[218] R. Gandhi *et al.*, "Ultrahigh-Energy Neutrino Interactions," *Astropart. Phys.* **5**, 81 (1996). `hep-ph/9512364`.

[219] R. Gandhi *et al.*, "Neutrino Interactions at Ultrahigh Energies," *Phys. Rev. D* **58**, 093009 (1998). `hep-ph/9807264`.

[220] A. M. Dziewonski and D. L. Anderson, "Preliminary Reference Earth Model," *Phys. Earth Planet. Inter.* **25**, 297 (1981).

[221] M. Honda *et al.*, "Calculation of Atmospheric Neutrino Flux Using the Interaction Model Calibrated with Atmospheric Muon Data," *Phys. Rev. D* **75**, 043006 (2007). `astro-ph/0611418`.

[222] G. Fiorentini, V. A. Naumov, and F. L. Villante, "Atmospheric Neutrino Flux Supported by Recent Muon Experiments," *Phys. Lett. B* **510**, 173 (2001). `hep-ph/0103322`.

[223] T. K. Gaisser, *Cosmic Rays and Particle Physics*, Cambridge University Press, 1990, p. 88.

[224] P. Lipari, "Lepton Spectra in the Earth's Atmosphere," *Astropart. Phys.* **1**, 195 (1993).

[225] D. Chirkin and W. Rhode, "Propagating Leptons through Matter with Muon Monte Carlo (MMC)," ArXiv e-print, 2004. `hep-ph/0407075`.

[226] P. A. Čerenkov, "Visible Radiation Produced by Electrons Moving in a Medium with Velocities Exceeding that of Light," *Phys. Rev.* **52**, 378 (1937).

[227] J. D. Jackson, *Classical Electrodynamics*, 3rd ed., Wiley, New York, 1999, pp. 637–640.

[228] J. Lundberg *et al.*, "Light Tracking Through Ice and Water: Scattering and Absorption in Heterogeneous Media with PHOTONICS," *Nucl. Instrum. Meth. A* **581**, 619 (2007). `astro-ph/0702108`.

[229] T. Hakamata *et al.*, eds., *Photomultiplier Tubes: Basics and Applications*, 3rd ed., Hamamatsu Photonics K.K., Shizuoka, Japan, 2006.

[230] C. Roucelle, "Documentation for the DOMcalibrator Module," IceCube Internal Report. `icecube/200709001`.

[231] D. Chirkin, "Feature Extraction of IceCube Waveforms," IceCube Internal Report. Docushare Document-48044.

[232] G. D'Agostini, "A Multidimensional Unfolding Method Based on Bayes' Theorem," *Nucl. Instrum. Meth. A* **362**, 487 (1995).

[233] F. James and M. Roos, "MINUIT: A System for Function Minimization and Analysis of the Parameter Errors and Correlations," *Comput. Phys. Commun.* **10**, 343 (1975).

[234] D. Pandel, "Bestimmung von Wasser- und Detektorparametern und Rekonstruktion von Myonen bis 100 TeV mit dem Baikal-Neutrinoteleskop NT-72," diploma thesis, Humboldt-Universität zu Berlin, 1996.

[235] J. Ahrens *et al.* (AMANDA Collaboration), "Muon Track Reconstruction and Data Selection Techniques in AMANDA," *Nucl. Instrum. Meth. A* **524**, 169 (2004). `astro-ph/0407044`.

[236] N. L. Johnson, S. Kotz, and N. Balakrishnan, *Continuous Univariate Distributions*, vol. 1, 2nd ed., Wiley, New York, 1994, ch. 17.

[237] G. Japaridze and M. Ribordy, "Realistic Arrival Time Distribution from an Isotropic Light Source," ArXiv e-print, 2005. `astro-ph/0506136`.

[238] N. van Eijndhoven, O. Fadiran, and G. Japaridze, "Implementation of a Gauss Convoluted Pandel PDF for Track Reconstruction in Neutrino Telescopes," *Astropart. Phys.* **28**, 456 (2007). `arXiv:0704.1706`.

[239] T. Neunhöffer, "Estimating the Angular Resolution of Tracks in Neutrino Telescopes Based on a Likelihood Analysis," *Astropart. Phys.* **25**, 220 (2006). `astro-ph/0403367`.

[240] J. Dumm and M. Baker, "IC-40 PS Cut Variables," IceCube Internal Wiki. `http://wiki.icecube.wisc.edu/index.php/IC-40_PS_Cut_Variables`.

[241] S. Grullon *et al.* for the IceCube Collaboration, "Reconstruction of High Energy Muon Events in IceCube Using Waveforms," in *Proceedings of the 30th International Cosmic Ray Conference*, edited by R. Caballero *et al.*, Universidad Nacional Autónoma de México, Mexico City, 2008, vol. 5 (HE part 2), contribution 1107, pp. 1475–1460.

[242] D. Boersma, S. Grullon, and G. Hill, "Photonics-Based Log-Likelihood Reconstruction in IceCube," IceCube Internal Report. `icecube/200807001`.

[243] J. Neyman, "Outline of a Theory of Statistical Estimation Based on the Classical Theory of Probability," *Phil. Trans. R. Soc. A* **236**, 333 (1937).

[244] A. Stuart, J. K. Ord, and A. Steven, *Classical Inference and the Linear Model*, vol. 2B of *Kendall's Advanced Theory of Statistics*, 6th ed., Arnold, London, 1994, ch. 19.

[245] K. Nakamura *et al.* (Particle Data Group), "Review of Particle Physics," *J. Phys. G* **37**, 075021 (2010).

[246] S. McBreen and E. Bissaldi, "GRB 081110: *Fermi* GBM Detection," *GCN Circ.* 8519 (2008).

[247] S. Tilav *et al.* for the IceCube Collaboration, "Atmospheric Variations as Observed by IceCube," in *Proceedings of the 31st International Cosmic Ray Conference*, Łódź, Poland, July 2009, contribution 1398. `arXiv:1001.0776`.

[248] P. Desiati *et al.* for the IceCube Collaboration, "Seasonal Variations of High Energy Cosmic Ray Muons Observed by the IceCube Observatory as a Probe of Kaon/Pion Ratio," in *Proceedings of the 32st International Cosmic Ray Conference*, Beijing, 2011, contribution 0662. `arXiv:1111.2735`.

[249] P. H. Barrett *et al.*, "Interpretation of Cosmic-Ray Measurements Far Underground," *Rev. Mod. Phys.* **24**, 133 (1952).

[250] GRB light curves cand be obtaind from the following locations:
Swift: `http://gcn.gsfc.nasa.gov/swift_gnd_ana.html`
Konus-Wind: `http://gcn.gsfc.nasa.gov/konus_grbs.html`

Suzaku HDX-WAM: `http://www.astro.isas.jaxa.jp/suzaku/HXD-WAM/WAM-GRB/grb/untrig/grb_table.html`
SuperAGILE: `http://agile.rm.iasf.cnr.it/gnc/gcn.html`
INTEGRAL IBAS:
`http://ibas.iasf-milano.inaf.it/IBAS_Results.html`
INTEGRAL SPI-ACS:
`http://www.isdc.unige.ch/integral/ibas/cgi-bin/ibas_acs_web.cgi`.

[251] The location of and distance from Earth cand be obtained from `http://cdaweb.gsfc.nasa.gov/sp_phys/` for Konus-Wind and `http://www.isdc.unige.ch/integral/ibas/cgi-bin/ibas_acs_web.cgi` for INTEGRAL.

[252] NASA, "FERMIGBRST - *Fermi* GBM Burst Catalog," Website. `http://heasarc.gsfc.nasa.gov/W3Browse/fermi/fermigbrst.html`.

[253] S. T. Holland, E. Fenimore, and K. L. Page, "Swift Observation of GRB 080515," *GCN Rep.* 141.1 (2008).

[254] H. Ziaeepour *et al.*, "Swift Observation of GRB 080426," *GCN Rep.* 130.1 (2008).

[255] C. B. Markwardt *et al.*, "GRB 081228, Swift-BAT Refined Analysis," *GCN Circ.* 8749 (2008).

[256] J. Mao *et al.*, "Swift Observation of GRB 080503," *GCN Rep.* 138.1 (2008).

[257] G. Stratta *et al.*, "Swift Observation of GRB 081024," *GCN Rep.* 174.1 (2008).

[258] S. Golenetskii *et al.*, "IPN Triangulation of Short Hard GRB 081209," *GCN Circ.* 8646 (2008).

[259] S. Golenetskii *et al.*, "GRB 081211B–Possibly a Short Burst with Extended Emission," *GCN Circ.* 8676 (2008).

[260] S. Golenetskii *et al.*, "IPN Localization of Short Hard GRB 081216," *GCN Circ.* 8677 (2008).

[261] S. Golenetskii *et al.*, "IPN Localization of Short Bright GRB 090227B," *GCN Circ.* 8925 (2009).

[262] T. N. Ukwatta *et al.*, "GRB 090426: Swift/BAT Spectral Lag Results," *GCN Circ.* 9272 (2009).

[263] R. D. Preece *et al.*, "The BATSE Gamma-Ray Burst Spectral Catalog. I. High Time Resolution Spectroscopy of Bright Bursts Using High Energy Resolution Data," *Astrophys. J. Suppl. Ser.* **126**, 19 (2000). `astro-ph/9908119`.

[264] J. K. Becker, "Neutrinos on the Rocks: On the Phenomenology of Potential Astrophysical Neutrino Sources," PhD thesis, Technische Universität Dortmund, Germany, 2007.

[265] I. Taboada and M. V. D'Agostino, "Correlating Prompt GRB Photons with Neutrinos," ArXiv e-print, 2007. `arXiv:0711.2277`.

[266] J. P. U. Fynbo *et al.*, "Low-resolution Spectroscopy of Gamma-ray Burst Optical Afterglows: Biases in the *Swift* Sample and Characterization of the Absorbers," *Astrophys. J. Suppl. Ser.* **185**, 526 (2009). `arXiv:0907.3449`.

[267] D. W. Hogg, "Distance Measures in Cosmology," ArXiv e-print, 1999. `astro-ph/9905116`.

[268] P. J. E. Peebles, *Principles of Physical Cosmology*, Princeton University Press, 1993, pp. 99–103.

[269] E. Komatsu *et al.*, "Seven-year *Wilkinson Microwave Anisotropy Probe* (WMAP) Observations: Cosmological Interpretation," *Astrophys. J. Suppl. Ser.* **192**, 18 (2011). `arXiv:1001.4538`.

[270] D. Guetta, M. Spada, and E. Waxman, "Efficiency and Spectrum of Internal Gamma-Ray Burst Shocks," *Astrophys. J.* **557**, 399 (2001). `astro-ph/0011170`.

[271] J. K. Becker *et al.*, "Coincident GRB Neutrino Flux Predictions: Implications For Experimental UHE Neutrino Physics," *Astropart. Phys.* **25**, 118 (2006). `astro-ph/0511785`.

[272] J. K. Becker, "High-Energy Neutrinos in the Context of Multimessenger Astrophysics," *Phys. Rep.* **458**, 173 (2008). `arXiv:0710.1557`.

[273] M. Ahlers, M. C. Gonzalez-Garcia, and F. Halzen, "GRBs on Probation: Testing the UHE CR Paradigm with IceCube," *Astropart. Phys.* **35**, 87 (2011). `arXiv:1103.3421`.

[274] E. Waxman, "Astrophysical Sources of High Energy Neutrinos," in *Proceedings of the XX^{th} International Conference on Neutrino Physics and Astrophysics*, edited by F. von Feilitzsch and N. Schmitz, *Nucl. Phys. B, Proc. Suppl.* **118**, 353 (2003). `astro-ph/0211358`.

[275] G. Punzi, "Sensitivity of Searches for New Signals and Its Optimization," in *Proceedings of the Conference on Statistical Problems in Particle Physics, Astrophysics, and Cosmology: PHYSTAT2003*, edited by L. Lyons, R. Mount, and R. Reitmeyer, Stanford Linear Accelerator Center, Stanford, CA, Sept. 2003, eConf C030908, MODT002, pp. 79–83. `physics/0308063`.

[276] G. C. Hill *et al.*, "Examining the Balance Between Optimising an Analysis for Best Limit Setting and Best Discovery Potential," in *Statistical Problems in Particle Physics, Astrophysics and Cosmology: Proceedings of PHYSTAT05*, edited by L. Lyons and M. Karagöz Ünel, Imperial College Press, London, 2005, pp. 108–111.

[277] G. C. Hill and K. Rawlins, "Unbiased Cut Selection for Optimal Upper Limits in Neutrino Detectors: The Model Rejection Potential Technique," *Astropart. Phys.* **19**, 393 (2003). `astro-ph/0209350`.

[278] J. Braun *et al.*, "Methods for Point Source Analysis in High Energy Neutrino Telescopes," *Astropart. Phys.* **29**, 299 (2008). `arXiv:0801.1604`.

[279] S. S. Wilks, "The Large-Sample Distribution of the Likelihood Ratio for Testing Composite Hypotheses," *Ann. Math. Statist.* **9**, 60 (1938).

[280] G. J. Feldman and R. D. Cousins, "Unified Approach to the Classical Statistical Analysis of Small Signals," *Phys. Rev. D* **57**, 3873 (1998). `physics/9711021`.

[281] J. R. Klein and A. Roodman, "Blind Analysis in Nuclear and Particle Physics," *Annu. Rev. Nucl. Part. Sci.* **55**, 141 (2005).

[282] R. D. Cousins and V. L. Highland, "Incorporating Systematic Uncertainties into an Upper Limit," *Nucl. Instrum. Meth. A* **320**, 331 (1992).

[283] J. Conrad *et al.*, "Including Systematic Uncertainties in Confidence Interval Construction for Poisson Statistics," *Phys. Rev. D* **67**, 012002 (2003). `hep-ex/0202013`.

[284] F. Tegenfeldt and J. Conrad, "On Bayesian Treatment of Systematic Uncertainties in Confidence Interval Calculation," *Nucl. Instrum. Meth. A* **539**, 407 (2005). `physics/0408039`.

[285] A. Schukraft, "PeakIce," IceCube Internal Wiki. `http://wiki.icecube.wisc.edu/index.php/PeakIce`.

[286] D. Chirkin, "Study of Ice Transparency with IceCube Flashers," IceCube Internal Report. `icecube/200911002`.

[287] D. Chirkin for the IceCube Collaboration, "Study of South Pole ice transparency with IceCube flashers," in *Proceedings of the 32^{st} International Cosmic Ray Conference*, Beijing, 2011, contribution 0333. `arXiv:1111.2731`.

[288] J. Pumplin *et al.*, "New Generation of Parton Distributions with Uncertainties from Global QCD Analysis," *J. High Energy Phys.* **7**, 12 (2002). `hep-ph/0201195`.

[289] E. V. Bugaev, I. A. Sokalski, and S. I. Klimushin, “Simulation Accuracy of Long Range Muon Propagation in Medium: Analysis of Error Sources,” ArXiv e-print, 2000. `hep-ph/0010323`.

[290] M. F. Morales, D. A. Williams, and T. De Young, “An Advanced Analysis Technique for Transient Searches in Wide-Field Gamma-Ray Observatories,” *Astropart. Phys.* **20**, 485 (2004). `astro-ph/0303178`.

[291] R. Abbasi *et al.* (IceCube Collaboration), “Limits on Neutrino Emission from Gamma-Ray Bursts with the 40 String IceCube Detector,” *Phys. Rev. Lett.* **106**, 141101 (2011). `arXiv:1101.1448`.

[292] R. Abbasi *et al.* (IceCube Collaboration), “An Absence of Neutrinos Associated with Cosmic-Ray Acceleration in γ-Ray Bursts,” *Nature* **484**, 351 (2012).

[293] P. Baerwald, S. Hümmer, and W. Winter, “Systematics in the Interpretation of Aggregated Neutrino Flux Limits and Flavor Ratios from Gamma-ray Bursts,” *Astropart. Phys.* **35**, 508 (2012). `arXiv:1107.5583`.

[294] D. Guetta, M. Spada, and E. Waxman, “On the Neutrino Flux from Gamma-Ray Bursts,” *Astrophys. J.* **559**, 101 (2001). `astro-ph/0102487`.

[295] G. Ghirlanda *et al.*, “Gamma-ray Bursts in the Comoving Frame,” *Mon. Not. R. Astron. Soc.* **420**, 483 (2012). `arXiv:1107.4096`.

[296] P. Baerwald, S. Hümmer, and W. Winter, “Magnetic Field and Flavor Effects on the Gamma-Ray Burst Neutrino Flux,” *Phys. Rev. D* **83**, 067303 (2011). `arXiv:1009.4010`.

[297] Z. Li, “Note on the Normalization of Predicted Gamma-ray Burst Neutrino Flux,” *Phys. Rev. D* **85**, 027301 (2012). `arXiv:1112.2240`.

[298] G. A. MacLachlan *et al.*, “Minimum Variability Time Scales of Long and Short GRBs,” ArXiv e-print , 2012. `arXiv:1201.4431`.

[299] R. J. Barlow, *Statistics*, Wiley, New York, 1989, ch. 5.